Compact and Efficient Millimetre-Wave Circuits for Wideband Applications

Ohlsson, Lars

2015

[Link to publication](#)

Citation for published version (APA):
Ohlsson, L. (2015). *Compact and Efficient Millimetre-Wave Circuits for Wideband Applications*. [Doctoral Thesis (compilation), Department of Electrical and Information Technology].

Total number of authors:
1

Compact and Efficient Millimetre-Wave Circuits for Wideband Applications

Lars Ohlsson

LUND UNIVERSITY

Doctoral Thesis
Electrical Engineering
Lund, April 2015

Organization: LUND UNIVERSITY Department of Electrical and Information Technology Ole Römers väg 3 223 63 Lund Sweden	*Document name:* DOCTORAL THESIS
	Date of issue: April 2015
Author: Lars Ohlsson	*Sponsoring organization(s):* Swedish Foundation for Strategic Research (SSF) Swedish Research Council (VR) Knut and Alice Wallenberg Foundation

Title and subtitle:
Compact and Efficient Millimetre-Wave Circuits for Wideband Applications

Abstract:
Radio systems, along with the ever increasing processing power provided by computer technology, have altered many aspects of our society over the last century. Various gadgets and integrated electronics are found everywhere nowadays; many of these were science-fiction only a few decades ago. Most apparent is perhaps your "smart phone", possibly kept within arm's reach wherever you go, that provides various services, news updates, and social networking via wireless communications systems. The frameworks of the fifth generation wireless system is currently being developed worldwide. Inclusion of millimetre-wave technology promise high-speed piconets, wireless back-haul on pencil-beam links, and further functionality such as high-resolution radar imaging.

This thesis addresses the challenge to provide signals at carrier frequencies in the millimetre-wave spectrum, and compact integrated transmitter front-ends of sub-wavelength dimensions. A radio frequency pulse generator, i.e. a "wavelet generator", circuit is implemented using diodes and transistors in III–V compound semiconductor technology. This simple but energy-efficient front-end circuit can be controlled on the time-scale of picoseconds. Transmission of wireless data is thereby achieved at high symbol-rates and low power consumption per bit. A compact antenna is integrated with the transmitter circuit, without any intermediate transmission line. The result is a physically small, single-chip, transmitter front-end that can output high equivalent isotropically radiated power. This element radiation characteristic is wide-beam and suitable for array implementations.

Keywords:
Compact circuit, dielectric resonator antenna, energy-efficiency, integrated transmitter, millimetre-wave spectrum, resonant-tunnelling diode, transistor, wavelet generator, wideband.

Classification system and/or index terms (if any):	*Language:* English
Supplementary bibliographical information (if any):	*ISBN (digital):* 978-91-7623-290-3
Key title and ISSN: Series of licentiate and doctoral theses, 1654-790X; No. 71	*ISBN (printed):* 978-91-7623-289-7
Recipient's notes:	*Number of pages:* 186	*Price:* Cost price
	Security classification: Unclassified	

Compact and Efficient Millimetre-Wave Circuits for Wideband Applications

Lars Ohlsson

LUND UNIVERSITY

Doctoral Thesis
Electrical Engineering
Lund, April 2015

Abstract

ʀᴀᴅɪᴏ systems, along with the ever increasing processing power provided by computer technology, have altered many aspects of our society over the last century. Various gadgets and integrated electronics are found everywhere nowadays; many of these were science-fiction only a few decades ago. Most apparent is perhaps your "smart phone", possibly kept within arm's reach wherever you go, that provides various services, news updates, and social networking via wireless communications systems. The frameworks of the fifth generation wireless system is currently being developed worldwide. Inclusion of millimetre-wave technology promise high-speed piconets, wireless back-haul on pencil-beam links, and further functionality such as high-resolution radar imaging.

This thesis addresses the challenge to provide signals at carrier frequencies in the millimetre-wave spectrum, and compact integrated transmitter front-ends of sub-wavelength dimensions. A radio frequency pulse generator, i.e. a "wavelet genarator", circuit is implemented using diodes and transistors in III–V compound semiconductor technology. This simple but energy-efficient front-end circuit can be controlled on the time-scale of picoseconds. Transmission of wireless data is thereby achieved at high symbol-rates and low power consumption per bit. A compact antenna is integrated with the transmitter circuit, without any intermediate transmission line. The result is a physically small, single-chip, transmitter front-end that can output high equivalent isotropically radiated power. This element radiation characteristic is wide-beam and suitable for array implementations.

Populärvetenskaplig Sammanfattning

*T*RÅDLÖS kommunikation via radiosystem har närapå blivit en rättighet i dagens samhälle. Vi förväntar oss att internet inte ska vara mer fjärran än där vi senast lade vår "smarta mobiltelefon"; antagligen inom armlängds avstånd. Strömmning av data ökar ständigt då vi nuförtiden själva vill bestämma när och var vi ska avnjuta, till exempel senaste säsongen i favoritserien. Visserligen kommer vi bara kunna se ett avsnitt eller två innan laddaren måste kopplas in, men det beror ju på att batteriet har för liten kapacitet. Eller, beror det på att elektroniken drar för mycket ström?

Traditionell kisel-baserad kretsteknologi med komplementära transistorer är utmäkt när det gäller hantering av digital data, men är inte det enda alternativet för trådlös elektronikkonstruktion. Antenner står för kopplingen mellan elektroniken och den elektromagnetiska radiokanalen, men behöver ett visst utrymme för att fungera optimalt. Kretsar och antenner ska sedan klämmas in på så liten yta som möjligt, vilket medför diverse designutmaningar och risk för ineffektivitet.

I forskningen som beskrivs i den här avhandlingen används komponenter i III–V-material för att utforska vad som kan åstadkommas utanför kisel-baserad kretsteknologi. Det är materialsystem där elektronernas grundläggande egenskaper kan påverkas på nanometernivå i så kallade heterostrukturer. Därmed kan en enkel men energieffektiv signalgenerator förverkligas, vilken tillåter konvertering av digital data till radiosymboler vid extrema hastigheter. Vidare demonstreras en liten men effektiv antenn i en alternativ implementering av en sändarkrets; den principiella frågan är ifall antennen och signalgeneratorn verkligen behöver vara två skilda enheter?

Acknowledgments

*N*ot a single word in this thesis would have been written without the mix of support and distractions that was provided by colleagues, family, and friends. To avoid any misconception that I can provide a comprehensive list and numeration of your contributions, I will keep this short.

Lars-Erik guided me among compound semiconductor devices and reviewers. *Daniel* helped me with electromagnetic concepts. *Mikael* taught me monolithic device design and fabrication. *Mats* shared know-how on millimetre-wave measurements and systems. *Erik* always had a mind for transistor physics. *Tomas* and *Patrick* hosted and propelled me. *Iman* provided antennas and algorithms. *Sebastian* brought new perspectives. *Mattias*, *Johannes*, and *Cezar* grew my crystals. *Carl* gave me the channel view. *Alexander* patched me through. *Nanoelectronics Group* were larger than their devices. *Electrical and Information Technology* were an interesting array of companions. *Lund Nano Lab* provided tools and solutions. *Anritsu* delivered test equipment. *Floorball team* worked me out.

Hilda is my love and co-explorer. *Mom*, *Dad*, *Sofi*, *Olof*, and *Adam* are the roots that support me. *Family* and *friends* are dear to me.

Thank you!

Lars Ohlsson
Lund, April 2015

Contents

PAPERS

Preface

*T*HIS doctoral thesis concludes work that I have performed over the recent half-decade and in collaboration with various colleagues. To aid any navigation, a summary of the structure is provided below. This is followed by an enumeration where I aim to clarify my personal contributions to the papers that are included in the thesis. Additional works that I have contributed to are listed thereafter, and the funding organisations are finally acknowledged.

STRUCTURE OF THE THESIS

This doctoral thesis is divided into three parts and their respective contents are organised as follows.

- **INTRODUCTION**
  The research field is reviewed and summarised, with emphasis on the papers that are included in the thesis.

  1: Background and Motivation
  Basic theory is utilised to motivate the research on high-frequency wavelet generators and the implementation of a monolithically-integrated wavelet transmitter.

  2: Millimetre-Wave Applications
  Non-dispersive antenna measurements are demonstrated in Paper I, and a quantitative characterisation method is described in Paper II. Energy-efficient multi-Gb/s wireless communication is shown in Paper III, while improved performance and a comparative study is presented in Paper IV.

3: Efficient Wavelet Generator

Techniques for signal generation in the millimetre-wave spectrum are discussed. A high-frequency transistor is realised in Paper V, and is utilised in the efficient wavelet generator presented in Paper VI. This quenchable oscillator is shown to allow generation of ultra-short wavelets in Paper VII. Analytic modelling and time-domain simulations are also shown possible, alleviating circuit design and verification.

4: Compact Wavelet Transmitter

A compact antenna technology is investigated in Paper VIII, and further development for monolithic integration is presented in Paper IX. A simple modelling approach is shown useful for describing its design and radiation mechanics. By combining the wavelet generator and antenna an integrated transmitter is realised in Paper X.

5: Outlook

Additions required for a complete time-domain system are discussed, and interesting developments and implementations utilising the investigated circuits are suggested.

- **APPENDICES**

  Further details on various aspects of the work can be found in the appendices.

  A: Device Fabrication

  A brief overview of the fabrication techniques is given, the fabrication scheme is summarised, and a representative batch processing recipe is disclosed.

  B: Electrical Models

  Additional information on the device modelling is provided.

  C: Numerical Methods

  The main numerical simulation methods are clarified.

- **PAPERS**

  The included papers are reproduced in the last part of the thesis. They cover fabrication of devices and circuits, as well as their implementation in various measurements. Observe that the copyrights of the papers are owned by the respective publishers.

INCLUDED PAPERS

The following papers are included in this thesis and the respective published or draft versions are appended at the back of this thesis.

Paper I: I. VAKILI, <u>L. OHLSSON</u>, M. GUSTAFSSON, AND L.-E. WERNERSSON, "Wideband and Non-Dispersive Wavelet Transmission Using Leaky Lens Antenna," *IET Electron. Lett.*, vol. 49, no. 5, pp. 321–322, Feb. 2013.

► *I designed and fabricated the generator circuits; performed the wavelet measurements; helped writing the paper.*

Paper II: <u>L. OHLSSON</u>, I. VAKILI, D. SJÖBERG, AND L.-E. WERNERSSON, "Time-Domain Wavelet Characterisation With Gating Techniques Applied to Millimetre-Wave Antennas," *IEEE Trans. Antennas Propag.*, Mar. 2015, submitted.

► *I designed and partially fabricated the generator circuits; planned and performed the measurements, as well as the data analysis; wrote the paper.*

Paper III: M. ÄRLELID, M. EGARD, <u>L. OHLSSON</u>, E. LIND, AND L.-E. WERNERSSON, "Impulse-Based 4 Gbit/s Radio Link at 60 GHz," *IET Electron. Lett.*, vol. 47, no. 7, pp. 467–468, Mar. 2011.

► *I partially designed the generator circuits; assisted during the measurements; helped writing the paper.*

Paper IV: <u>L. OHLSSON</u>, AND L.-E. WERNERSSON, "A 15-Gb/s Wireless ON-OFF Keying Link," *IEEE Access*, vol. 2, pp. 1307–1313, Oct. 2014.

► *I designed and fabricated the generator circuits; planned and performed the measurements, as well as the data analysis; wrote the paper.*

Paper V: M. EGARD, <u>L. OHLSSON</u>, M. ÄRLELID, K.-M. PERSSON, B. M. BORG, F. LENRICK, R. WALLENBERG, E. LIND, AND L.-E. WERNERSSON, "High-Frequency Performance of Self-Aligned Gate-Last Surface Channel $In_{0.53}Ga_{0.47}As$ MOSFET," *IEEE Electron Device Lett.*, vol. 33, no. 3, pp. 369–371, Mar. 2012.

► *I designed and partially fabricated the transistors; assisted during measurements; helped writing the paper.*

Paper VI: M. EGARD, M. ÄRLELID, <u>L. OHLSSON</u>, B. M. BORG, E. LIND, AND L.-E. WERNERSSON, "$In_{0.53}Ga_{0.47}As$ RTD-MOSFET Millimeter-Wave Wavelet Generator," *IEEE Electron Device Lett.*, vol. 33, no. 7, pp. 970–972, Jul. 2012.

► *I designed and partially fabricated the generator circuits; assisted during measurements; helped writing the paper.*

Paper VII: L. Ohlsson, P. Fay, and L.-E. Wernersson, "Picosecond Dynamics in a Millimetre-Wave RTD-MOSFET Wavelet Generator," *IET Electron. Lett.*, Apr. 2015, submitted.

► *I designed and fabricated the generator circuits; planned and performed the measurements, as well as the data analysis and simulations; wrote the paper.*

Paper VIII: L. Ohlsson, D. Sjöberg, M. Ärlelid, M. Egard, E. Lind, and L.-E. Wernersson, "Admittance Matching of 60 GHz Rectangular Dielectric Resonator Antennas for Integrated Impulse Radio," in *2010 Conf. Loughborough Antennas and Propagation (LAPC)*, Nov. 8-9, 2010, pp. 253–256.

► *I designed, fabricated, and assembled the antennas; planned and performed the measurements; wrote the paper and presented a poster at the conference.*

Paper IX: L. Ohlsson, T. Bryllert, C. Gustafson, D. Sjöberg, M. Egard, M. Ärlelid, and L.-E. Wernersson, "Slot-Coupled Millimeter-Wave Dielectric Resonator Antenna for High-Efficiency Monolithic Integration," *IEEE Trans. Antennas Propag.*, vol. 61, no. 4, pp. 1599–1607, Apr. 2013.

► *I designed, fabricated, and assembled the antennas and carrier substrates; planned and performed the reflection measurements, as well as the data analysis; wrote the paper.*

Paper X: L. Ohlsson, T. Bryllert, D. Sjöberg, and L.-E. Wernersson, "Monolithically-Integrated Millimetre-Wave Wavelet Transmitter With On-Chip Antenna," *IEEE Microw. Wireless Compon. Lett.*, vol. 24, no. 9, pp. 625–627, Sep. 2014.

► *I designed, fabricated, and assembled the transmitter circuits; designed the carrier circuit-boards; planned and performed the measurements, as well as the data analysis; wrote the paper.*

EXTRANEOUS PAPERS

The following papers are not included in the thesis, but summarise related work which I have contributed to.

Paper xi: M. Egard, L. Ohlsson, B. M. Borg, L.-E. Wernersson, and E. Lind, "Self-Aligned Gate-Last Surface Channel $In_{0.53}Ga_{0.47}As$ MOSFET With Selectively Regrown Source and Drain Contact Layers," in *69th Annu. Conf. Device Research (DRC 2011)*, Jun. 20-22, 2011, pp. 1–2.

Paper xii: M. Ärlelid, L. Ohlsson, M. Egard, E. Lind, and L.-E. Wernersson, "60 GHz Impulse Radio Measurements," in *2011 IEEE Int. Conf. Ultra-Wideband (ICUWB)*, Sep. 14-16, 2011, pp. 536–540.

Paper xiii: M. EGARD, <u>L. OHLSSON</u>, B. M. BORG, F. LENRICK, R. WALLENBERG, L.-E. WERNERSSON, AND E. LIND, "High Transconductance Self-Aligned Gate-Last Surface Channel In$_{0.53}$Ga$_{0.47}$As MOSFET," in *2011 IEEE Int. Electron Devices Meeting (IEDM)*, Dec. 5-7, 2011, pp. 13.2.1–13.2.4.

Paper xiv: I. VAKILI, <u>L. OHLSSON</u>, M. GUSTAFSSON, AND L.-E. WERNERSSON, "Pulse Transmission Using Leaky Lens Antenna and RTD-MOSFET Wavelet Generator," in *7th European Conf. Antennas and Propagation (EuCAP 2013)*, Apr. 8-12, 2013, pp. 324–325.

Paper xv: M. EGARD, M. ÄRLELID, <u>L. OHLSSON</u>, B. M. BORG, E. LIND, AND L.-E. WERNERSSON, "Frequency Modulation in Mm-Wave InGaAs MOSFET/RTD Wavelet Generators," in *25th IEEE Int. Conf. Indium Phosphide and Related Materials (IPRM 2013)*, May 19-23, 2013, pp. 1–2.

Paper xvi: G. ROLL, M. EGARD, S. JOHANNSON, <u>L. OHLSSON</u>, L.-E. WERNERSSON, AND E. LIND, "RF Reliability of Gate Last InGaAs nMOSFETs with High-k Dielectric," in *2013 IEEE Int. Integrated Reliability Workshop (IRW) Final Report*, Oct. 13-17, 2013, pp. 38–41.

Paper xvii: G. ROLL, E. LIND, M. EGARD, S. JOHANSSON, <u>L. OHLSSON</u>, AND L.-E. WERNERSSON, "RF and DC Analysis of Stressed InGaAs MOSFETs," *IEEE Electron Device Lett.*, vol. 35, no. 2, pp. 181–183, Feb. 2014.

Paper xviii: I. VAKILI, <u>L. OHLSSON</u>, M. GUSTAFSSON, AND L.-E. WERNERSSON, "Time Domain Material Characterizations Using Leaky Lens Antennas," in *31st URSI Symp. General Assembly and Scientific (URSI GASS 2014)*, Aug. 16-23, 2014, pp. 1–2.

Paper xix: I. VAKILI, <u>L. OHLSSON</u>, L.-E. WERNERSSON, AND M. GUSTAFSSON, "Complex Permittivity Extraction Using a Leaky-Lens Antenna System," in *2014 Symp. Progress In Electromagnetics Research (PIERS)*, Aug. 25-28, 2014, pp. 1271.

Paper xx: I. VAKILI, <u>L. OHLSSON</u>, L.-E. WERNERSSON, AND M. GUSTAFSSON, "Time-Domain System for Millimeter-Wave Material Characterization," *IEEE Trans. Microw. Theory Techn.*, Mar. 2015, submitted revision.

Paper xxi: D. SJÖBERG, <u>L. OHLSSON</u>, I. VAKILI, M. GUSTAFSSON, AND L.-E. WERNERSSON, "Impulse Based Radio Technology for Mm-Waves," in *9th European Conf. Antennas and Propagation (EuCAP 2015)*, Apr. 12-17, 2015, presented.

FUNDING ORGANISATIONS

Abbreviations and Symbols

ABBREVIATIONS

5G fifth generation wireless system

Al aluminium
AlAs aluminium arsenide
ALD atomic layer deposition
As arsenic
ASIC application-specific integrated circuit
ASK amplitude-shift keying
Au gold
AWGN additive white Gaussian noise

Be beryllium
BER bit-error rate
BOE buffered oxide etch

Cl chlorine
CMOS complementary metal-oxide-semiconductor
CPW coplanar waveguide
Cu copper
CW continuous-wave

DC direct-current
DIW de-ionised water
DR dielectric resonator
DRA dielectric resonator antenna
DUT device under test

EBL electron beam lithography
EE energy-efficiency
ENIG electroless nickel immersion gold

F fluor
FD frequency-domain
Fe iron

Ga gallium
GaAs gallium arsenide

H hydrogen
H_2O water
H_2O_2 hydrogen peroxide
H_3PO_4 phosphoric acid
HBT heterojunction bipolar transistor
HCl hydrochloric acid
HEMT high electron-mobility transistor
Hf hafnium
HSQ hydrogen silsesquioxane

III–V compound semiconductor
In indium
In–Al–As indium–aluminium–arsenide
    $In_{0.52}Al_{0.48}As$ an In–Al–As composition that is lattice-matched to InP
InAs indium arsenide
In–Ga–As indium–gallium–arsenide
    $In_{0.53}Ga_{0.47}As$ an In–Ga–As composition that is lattice-matched to InP
    $In_{0.70}Ga_{0.30}As$ an In–Ga–As composition
InP indium phosphide
IPA iso-propyl alcohol

LOS line-of-sight
LTI linear, time-invariant

MBE molecular beam epitaxy
MCM multi-chip module
MIBK methyl iso-butyl ketone
MIMO multiple-input multiple-output
mmW millimetre-wave
MOSFET metal-oxide-semiconductor field-effect transistor
MOVPE metal-organic vapour-phase epitaxy

N nitrogen

NDC negative differential conductance
(NH$_4$)$_2$S ammonium sulphide
NH$_4$OH ammonium hydroxide
NID not intentionally doped

O oxygen
OOK on-off keying

P phosphorus
PCB printed circuit board
Pd palladium
PMMA poly methyl-methacrylate
PRBS pseudo-random binary sequence
PSD power spectral density

QAM quadrature amplitude modulation
QPSK quadrature phase-shift keying

RF radio frequency
RMS root-mean-square
RTD resonant-tunnelling diode

S sulphur
Sb antimony
SF$_6$ sulphur hexafluoride
SI semi-insulating
Si silicon
SNR signal-to-noise ratio

TD time-domain
TE transverse electric
TEM transverse electromagnetic
Ti titanium
TMAH tetra-methyl ammonium hydroxide

UV ultra-violet

VNA vector network analyser

WLAN wireless local area network
WPAN wireless personal area network
WRx wavelet receiver
WTx wavelet transmitter

GREEK SYMBOLS

α (Np/m) attenuation constant of transmission line

β (rad/m) phase constant of transmission line

γ (1/m) propagation constant of transmission line
   γ_c coupling-slot propagation constant
   γ_k propagation constant of line interfacing port k
$\Gamma_{\textbf{eff}}$ (V) effective resonance voltage-width
Γ_f voltage reflection coefficient

$\delta_{\textbf{s}}$ (m) skin depth
Δ (m) imaging radar resolution
   $\Delta_{\textbf{x}}$ cross-range resolution
   $\Delta_{\textbf{y}}$ down-range resolution

$\varepsilon_{\textbf{0}}$ ($8.854,187,82\ldots\cdot10^{-12}$ F/m) vacuum permittivity
$\varepsilon_{\textbf{r}}$ relative electric permittivity
   $\varepsilon_{\textbf{r,eff}}$ effective relative permittivity
   $\varepsilon_{\textbf{r,InP}}$ relative permittivity of InP, approximately 12.6
   $\varepsilon_{\textbf{r,s}}$ slot line relative permittivity

η ideality factor
   $\eta_{\textbf{lkg}}$ leakage ideality
   $\eta_{\textbf{res}}$ resonant-tunnelling ideality

Θ (rad) spectral phase
   $\Theta_{\textbf{min}}$ minimum-phase

$\kappa_{\textbf{dep}}$ (C/($\sqrt{V}$–m^2)) depletion constant

λ (m) wavelength
   $\lambda_{\textbf{0}}$ free-space wavelength
   λ_g guided wavelength

$\mu_{\textbf{0}}$ ($4\pi\cdot10^{-7}$ H/m) vacuum permeability
$\mu_{\textbf{r}}$ relative magnetic permeability, typically 1
   $\mu_{\textbf{r,eff}}$ effective relative magnetic permeability

π ($3.141,592,65\ldots$) circular constant

ρ (Ω–m) electrical resistivity
   $\rho_{\textbf{d}}$ resistivity of dielectric
   $\rho_{\textbf{m}}$ resistivity of metal

ρ_c (Ω–m^2) specific contact resistivity

    $\rho_{c,c}$ collector specific resistivity

    $\rho_{c,e}$ emitter specific resistivity

σ (m^2) radar cross-section

τ_g (s) group-delay

τ_{trc} (s) transit-charge delay

Φ (rad) perceived angular width of linear synthetic aperture

ω (rad/s) angular frequency

    ω_r resonator resonance angular frequency

LATIN SYMBOLS

a_x (m) width of a rectangular dielectric waveguide

A (m^2) area

    A_{eff} active area

A_0 ($1.201, 732, 01 \ldots \cdot 10^6$ A/(m–K)^2) Richardson's constant

b_y (m) height of rectangular dielectric waveguide

B (Hz) bandwidth

    B_N noise bandwidth

    B_S signal bandwidth

c_0 (299,792,458 m/s) speed of light

C (F) capacitance

    C_{ce} external collector-emitter parallel capacitance

    C_{dep} depletion capacitance

    C_{ds} external drain-source parallel capacitance

    C_{eff} effective capacitance

    C_{tc} terminating coupling-slot capacitance

    C_{tk} terminating CPW stub capacitance

    C_{trc} transit-charge capacitance

C' (F/m) capacitance per unit length of a transmission line

    C'_r resonator capacitance per unit length

    C'_s slot capacitance per unit length

C_0 (F/m^2) intrinsic heterostructure capacitance per unit area

$C_{Shannon}$ (b/s) Shannon's channel capacity

d_c (m) channel-distance

    $d_{c,i}$ equivalent isotropic channel-distance

$d_{c,Rx}$ radar receiver channel-distance

$d_{c,Tx}$ radar transmitter channel-distance

d_z (m) length of a rectangular dielectric waveguide

D (W/Hz) power spectral density

D_N noise spectral density

$D_{N,0}$ ambient noise spectral density

t_m (m) ground-plane metallisation thickness

t_{rtd} (m) heterostructure thickness

e (2.718, 281, 82...) Euler's number

$\vec{E}$ (V/m) electric vector field

f (Hz) frequency

f_c carrier frequency

f_i intrinsic fundamental resonance frequency of dielectric body

f_{max} maximum oscillation frequency

f_p offset frequency of periodic nulls, inverse of pulse-length

f_r resonator resonance frequency

f_t current gain cut-off, or transition, frequency

F_N (dB) noise figure, or additional noise gain

$F_{N,Rx}$ receiver noise figure

g (S/m^2) differential conductace per unit area

g_{min} minimum differential conductance

G (S) conductance

$G_{L,max}$ maximum load conductance

$G_{L,opt}$ optimum load conductance

G_S source conductance

G' (S/m) conductance per unit length of transmission line

G'_r resonator conductance per unit length

G'_s slot conductance per unit length

G_A (dBi) realised antenna gain

$G_{A,Rx}$ receive antenna gain

$G_{A,Tx}$ transmit antenna gain

G_P (dB) power gain

$G_{P,Rx}$ receiver gain

h_P (6.626, 069, 57... $\cdot$ 10^{-34} J–s) Planck's constant

h_t (1/s) impulse-response of a device under test

h_y (m) height of a rectangular dielectric resonator antenna on a ground-plane

$\vec{H}$ (A/m) magnetic vector field

H_f transfer-function of a device under test

I (A/Hz) current phasor, or phasor spectral density, in frequency-domain
   I^- departing current
   I^+ impinging current
$I_\mathbf{D}$ (A/m) normalised drain current

$\mathbf{j}$ imaginary unit, defined by $\mathrm{j}^2 = -1$
J (A/m^2) current density
   $J_\mathbf{0}$ mean peak and valley current
   $J_\mathbf{C}$ collector current
   $J_\mathbf{C,approx}$ collector current approximation
   $J_\mathbf{lkg}$ thermionic-emission leakage current
   $J_\mathbf{V}$ leakage current at threshold
   $J_\mathbf{P}$ approximate peak current
   $J_\mathbf{pv}$ peak-to-valley difference current
   $J_\mathbf{res}$ resonant-tunnelling current

k port indices of a multi-port device under test
$k_\mathbf{0}$ (1/m) free-space wavenumber
$k_\mathbf{B}$ ($1.380,648,81\ldots \cdot 10^{-23}$ J/K) Boltzmann's constant
$k_\mathbf{i}$ (1/m) wavenumber in dielectric waveguide
   $k_\mathbf{x}$ transverse wavenumber in x-direction
   $k_\mathbf{y}$ transverse wavenumber in y-direction
   $k_\mathbf{z}$ longitudinal wavenumber in z-direction

l (m) length of transmission line
   $l_\mathbf{s}$ length of coupling-slot
L (H) inductance
   $L_\mathbf{tk}$ inductance of oscillator tank shunted by port
   $L_\mathbf{tn}$ inductance of oscillator tank not shunted by port
   $L_\mathbf{tnk}$ inductance of oscillator tank
L' (H/m) inductance per unit length of a transmission line
   $L'_\mathbf{r}$ resonator inductance per unit length
   $L'_\mathbf{s}$ slot inductance per unit length
$L_\mathbf{c}$ (dB!!) radio channel loss
   $L_\mathbf{Friis}$ free-pace pathloss from Friis' transmission equation
$L_\mathbf{P}$ (dB) relative power loss
   $L_\mathbf{P,Rx}$ receiver insertion loss
   $L_\mathbf{P,Tx}$ transmitter insertion loss

$m_\mathbf{e}^*$ relative effective electron mass
$m_\mathbf{0}$ ($9.109,382,15\ldots \cdot 10^{-31}$ kg) free electron mass

$\hat{\mathbf{n}}$ (m) unit normal direction vector

$N_{\mathbf{dep}}$ (1/m^3) depleted spacer layer doping density

P (W) power
  $P_{\mathbf{AvS}}$ available source power
  $P_{\mathbf{L}}$ load power
  $P_{\mathbf{N}}$ noise power
  $P_{\mathbf{Rx}}$ received power
  $P_{\mathbf{S}}$ source power
  $P_{\mathbf{Tx}}$ transmitted power

q (C/m^2) charge per unit area
  $q_{\mathbf{CE}}$ collector-emitter charge
  $q_{\mathbf{dep}}$ depletion charge
  $q_{\mathbf{trc}}$ transit-charge
$q_{\mathbf{e}}$ ($1.602, 176, 57 \ldots \cdot 10^{-19}$ C) elementary charge
Q quality factor
  $Q_{\mathbf{r}}$ resonator quality factor
  $Q_{\mathbf{tnk}}$ tank inductor quality factor

R (Ω) resistance
  $R_{\mathbf{ce}}$ external collector-emitter series resistance
  $R_{\mathbf{ds}}$ external drain-source series resistance
  $R_{\mathbf{off}}$ off-resistance, cut-off region
  $R_{\mathbf{on}}$ on-resistance, linear region
R' (Ω/m) resistance per unit length of a transmission line
  $R'_{\mathbf{s}}$ slot resistance per unit length

$s_{\mathbf{s}}$ (m) un-tapered length of coupling-slot
$\vec{S}$ (W/m^2) Poynting vector
S_f scattering matrix
$S_{\mathbf{L}}$ (W) receiver sensitivity

t (s) time
  $t_{\mathbf{p}}$ wavelet duration, or pulse-length
T (s) time period, or interval
  $T_{\mathbf{c}}$ carrier oscillation period
  $T_{\mathbf{s}}$ signal transient period
$T_{\mathbf{amb}}$ (K) ambient temperature

u (V) voltage signal in time-domain
  u^- departing voltage
  u^+ impinging voltage
  $u_{\mathbf{Ctrl}}$ wavelet generator control voltage

U (V/Hz) voltage phasor, or phasor spectral density, in frequency-domain

  U_2^+ impinging voltage, towards port 2
  U_2^- departing voltage, from port 2
  U_1^- departing voltage, from port 1
  U_1^+ impinging voltage, towards port 1
  U^- departing voltage
  U^+ impinging voltage
  U_S source voltage
  $U_{S,k}$ source voltage interfacing port k

v (m/s) velocity

  v_{lin} linear acceleration velocity
  v_{th} thermal velocity

v_s (m) width of coupling-slot

V (V) voltage

  V_0 mean value of valley- and peak- voltage, modelled
  V_{Bias} bias voltage
  V_{CE} collector-emitter voltage
  V_{CE}' external collector-emitter voltage
  V_{DS} drain-source voltage
  V_{GS} gate-source voltage
  V_N negative-conductance voltage
  V_p pulse, or wavelet, amplitude
  V_T tunnelling threshold voltage
  V_{th} thermal voltage
  V_V leakage threshold voltage
  V_{vp} valley-to-peak voltage difference

w_s (m) width that coupling-slot is tapered to

x (m) spatial dimension

y (m) spatial dimension

Y (S) admittance

  Y_A antenna admittance

Y' (S/m) transmission line admittance per unit length

  Y_c' coupling-slot admittance

z (m) spatial dimension

Z (Ω) impedance

  Z_L load impedance
  Z_S source impedance
  $Z_{S,k}$ source impedance interfacing port k

Z_T transformed load impedance

Z_{tc} terminating impedance

Z' (Ω/m) transmission line impedance per unit length

Z'_c coupling-slot impedance

Z_0 (Ω) characteristic impedance of transmission line

$Z_{0,c}$ characteristic impedance coupling-slot

$Z_{0,k}$ characteristic impedance of transmission line interfacing port k

$Z_{0,s}$ characteristic impedance of un-loaded and lossless coupling-slot

FUNCTIONS AND OPERATORS

arctan($\cdot$) inverse tangent

exp($\cdot$) exponential with basis e, natural exponential

FA$\{\cdot\}$ Fourier analysis, transforming from temporal to spectral domain

FS$\{\cdot\}$ Fourier synthesis, transforming from spectral temporal domain

Im$\{\cdot\}$ imaginary part, returns the imaginary part of a complex variable

ln($\cdot$) natural logarithm, basis e

log$_2$($\cdot$) logarithm, basis 2

Re$\{\cdot\}$ real part, returns the real part of a complex variable

sin($\cdot$) sine

sinh($\cdot$) hyperbolic sine

tan($\cdot$) tangent

tanh($\cdot$) hyperbolic tangent

INTRODUCTION

"The mountains are calling and I must go."

—John Muir

1
Background and Motivation

$\mathcal{A}$BOUT one-and-a-half centuries ago, Maxwell formulated the equations that describe the interaction of materials and electromagnetic waves. Since then, radio electronics have evolved from the early spark gap experiments to radars and digital communications. This evolution was propelled by continuous progress in signal generation and detection by current switching, electromagnetic cavities, and solid-state devices. At the end of the 19th century, wireless telegraph transmissions revolutionised communications. Over the first half of the 20th century, radar technology forever changed the methods of navigation and surveillance. In the second half of the century, the discrete components of old were substituted by devices fabricated in integrated technologies; this allowed for a controlled climb of the radio frequency (RF) spectrum, 3 kHz–300 GHz.

Meanwhile, circuit implementations of Turing's "universal machine" provided a means to automatise arithmetic tasks, and perform them at incomprehensible speed. These computers have revolutionised our everyday life, and allow virtually unlimited storage and exchange of information. In the beginning of the 21st century, processing power of portable and hand-held devices increased rapidly. High performance digital radios, striving to close the gap to wired technologies, can now be found in consumer electronics. Wireless streaming of data is an ever increasing demand which pushes the industry towards the fifth generation wireless system (5G) implementations [1, 2]. This new generation of wireless communication is envisioned to be diverse and utilise various bands in the microwave spectrum, 300 MHz–300 GHz, each task implemented in the spectral region where the most performance can be achieved.

The millimetre-wave (mmW) spectrum, 30–300 GHz, is the last decade of
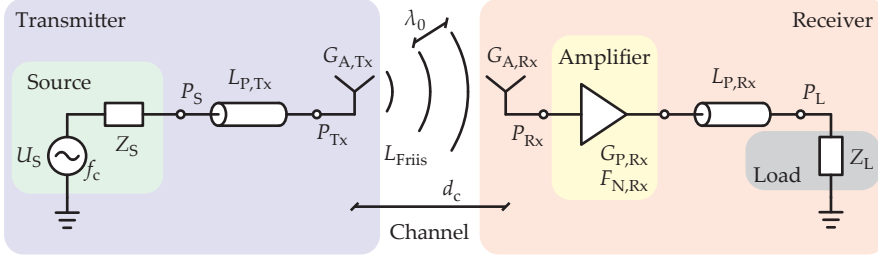
Figure 1.1: A schematic illustration of a generic wireless system, i.e. transmitter, channel, and receiver, for the illustration of a link power budget.

frequencies in the microwave spectrum; etymologically from the handful of millimetres which are the corresponding free-space wavelengths. Wireless systems are approaching this frequency range on the quest for more bandwidth, potentially increasing system performance. The challenge mainly lies in limited device stability, reproducibility, and available output power, as the frequencies are relatively high. This also inflicts stringent demands on the antenna fabrication and assembly accuracy, as the wavelengths are short. Further, mechanical milling being too coarse and thin-film processing susceptible to areal variations, the processing technological no-mans-land between micrometres and millimetres must be bridged.

1.1 LINK BUDGET

Designing any wireless system, a link power budget can be helpful. For this purpose, a simple wireless system is shown in Figure 1.1, and the corresponding power budget is to be determined. More precisely, the signal power into the load, P_L, in the receiver must be deduced by relating it, i.e. via the link, to the power delivered from the source, P_S, in the transmitter. It must further be compared to that of the noise, P_N, and the input-referred sensitivity limit of the receiver, S_L. For clarity, each connection in the schematic represents a two-terminal pair, i.e. a Wheeler RF signal port, while bias inputs and ground terminals are neglected.

On the transmitter side, a wireless system has a signal source with an output power, P_S, operating in a bandwidth, B_S, centred about a carrier frequency, f_c. This signal is typically fed to a transmission line with an insertion loss, $L_{P,Tx}$. Keeping it simple, i.e. ignoring reflections, the signal then propagates to, and is accepted by, the transmitter antenna with realised gain, $G_{A,Tx}$, in the direction towards the receiver antenna. Its realised gain, $G_{A,Rx}$, is obviously evaluated in the opposite direction.

The transmitted power, P_{Tx}, will propagate in a radio channel and parts of it will eventually be received, P_{Rx}. Knowledge of the power delay profile of the channel is required to determine the effective loss between the antennas. Its quantification in a generalised environment is a science of its own, especially at mmW frequencies [3], but to cover a few of the possible factors, any multipath propagation as well as antenna user interference will affect the channel loss. Under line-of-sight (LOS) free-space propagation conditions, however, Friis' transmission equation can be utilised to identify the pathloss [4], as

$$L_{\text{Friis}} = \left(\frac{4\pi d_{\text{c}}}{\lambda_0} \right)^2,$$ (1.1)

where d_{c} denotes the channel distance, $\lambda_0 = c_0/f_{\text{c}}$ the free-space wavelength, $c_0 = 1/\sqrt{\varepsilon_0 \mu_0}$ is the speed of light, and ε_0 and μ_0 is the vacuum permittivity and permeability, respectively. This simply makes the practical, but impossible, assumption that the signal spreads isotropically and radially from one point source, and is collected at another. Departures from this assumption are mitigated into the antenna gain.

In the receiver, the signal is again typically fed through a transmission line with some insertion loss, $L_{\text{P,Rx}}$. A low-noise amplifier with power gain, $G_{\text{P,Rx}}$, and noise figure, $F_{\text{N,Rx}}$, then amplifies the signal to reach above the sensitivity of the receiver. The signal power in the load of the receiver is in its ideal form thereby found as,

$$P_{\text{L}} = \frac{G_{\text{P,Rx}} G_{\text{A,Rx}} G_{\text{A,Tx}}}{L_{\text{P,Rx}} L_{\text{Friis}} L_{\text{P,Tx}}} P_{\text{S}}.$$ (1.2)

The corresponding noise power delivered to the receiver load is often dominated by the ambient noise at the receive antenna port and can thereby be found as,

$$P_{\text{N}} = \frac{G_{\text{P,Rx}} F_{\text{N,Rx}}}{L_{\text{P,Rx}}} B_{\text{N}} D_{\text{N,0}},$$ (1.3)

where $D_{\text{N,0}}$ is the ambient additive white Gaussian noise (AWGN) power spectral density, and B_{N} denotes the equivalent noise bandwidth of the receiving circuit.

The radio link can provide functionality if the received power is greater than the input referred sensitivity, $P_{\text{L}} > S_{\text{L}}$, and if the signal-to-noise ratio (SNR) is high enough, $P_{\text{L}}/P_{\text{N}} \gg 1$. If any of the signal parameters in the above link budget are significantly non-constant over its bandwidth, B, the power variables must be substituted with the corresponding power spectral densities (PSDs), e.g. $P \to D = P/B$ in an even-distributed case. Also, the centre frequency in (1.1) should be substituted by the frequency, $f_{\text{c}} \to f$.

1.2 WIRELESS SYSTEM PERFORMANCE

Having evaluated that power can be transmitted over a wireless link, the performance or capacity of such a link is of interest. This is a challenging question as the answer will depend greatly on the purpose of the link. However, there are a two fundamental properties that are important for the performance of most systems; the bandwidth, B_S, and the SNR which is the quotient of received signal power over the noise power in the reciever, P_L/P_N. This is thereby, via the link budget in (1.2), related to the generated signal power, P_S.

In a communications system, Shannon's channel capacity, $C_{Shannon}$, can be determined by the Shannon-Hartley theorem under AWGN [5], as

$$C_{Shannon} = B_S \log_2(1 + \frac{P_L}{P_N}).$$ (1.4)

This channel capacity is a theoretical upper bound for information transfer rate and (1.4) thereby provides basic insight into how to increase the performance of a communications link. Analysing (1.4), two regions of operation are typically identified with regard to the SNR. The first is the case of low received SNR, not allowing the second term of the sum in the logarithm to dominate. This is the bandwidth limited region, where an approximately linear dependence on the bandwidth can be observed; capacity can primarily be increased by increasing the symbol-rate. By contrast, if the second term in the logarithm dominates, i.e. $P_L \gg P_N = B_N D_N$, the bandwidth dependence approximately cancels. The capacity becomes power limited and the signal amplitude or phase can primarily be utilised to define additional symbol diversity to encode more data per symbol. A system operating at the upper end of its range or at a very high symbol-rate, both cases assuring a low SNR, must according to (1.4) be bandwidth limited.

Detection and ranging is another application for wireless RF signals, generally known as radar. This is based on the concept of transmitting an electromagnetic pulse and analysing the reflected response, providing information of the surrounding environment, i.e. the "radar range". Navigation, naval or airborne but also recently established in the automotive industry, is a traditional radar application. Further well-known examples can be found in geophysical or astronomical mapping, and surveillance for military or security purposes. Depending on the geometrical configuration and movement of the radar transceiver, together with the available knowledge of the radar range, most tasks involving detection of material interfaces, e.g. air/ metal, can be attempted.

A synthetic aperture radar operates by measuring the response of a range from various positions, e.g. even-spaced along a line, as illustrated in
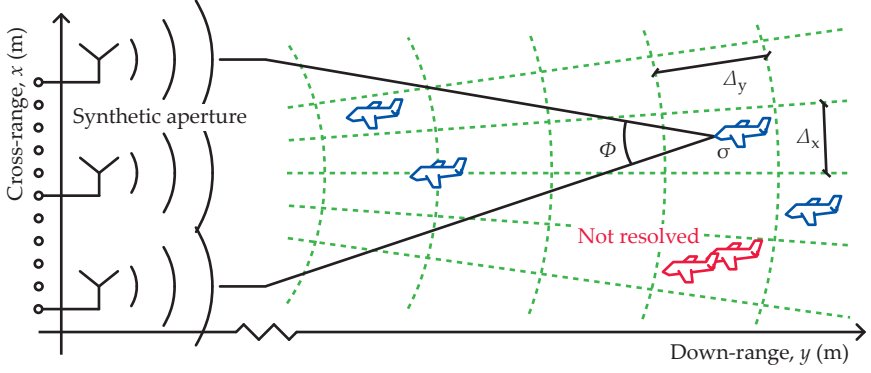
Figure 1.2: A schematic radar range, illustrating a linear synthetic aperture and its down- and cross-range resolution. The model aircraft illustrate generic targets on the radar range.

Figure 1.2. The data from all positions is then migrated into an image that visualises the reflected responses from any targets. For an imaging radar, there are at least two dimensions which require resolution, defined as the minimum separation between two objects which reproduces them as two separate responses. Down-range resolution, Δ_y, i.e. in the signal propagation direction, and cross-range resolution, Δ_x, i.e. in the perpendicular direction, as depicted by the grid in Figure 1.2. For an ideal linear synthetic aperture radar, down-range resolution is provided by the bandwidth,

$$\Delta_y = \frac{c_0}{2B_S},\tag{1.5}$$

and the cross-range resolution improves with the carrier frequency,

$$\Delta_x = \frac{c_0}{2f_c \sin(\Phi)},\tag{1.6}$$

where Φ denotes the angular width of the linear synthetic aperture [6]. To allow target illumination over a large angular width, high output power and a relatively wide-beam antenna is required. Once again, as for the communications link, the system performance is found to be proportional to the signal bandwidth. By contrast, increased carrier frequency also provides resolution enhancements in an aperture radar system. For clarity, the expressions in (1.5) and (1.6) state the respective ideal resolutions for a linear synthetic aperture radar. Any imaging algorithm may increase the minimum distances that can be resolved.

From the viewpoint of a radar system, the received power in the link budget has to be modified. The "radar equation" can be used to predict the received
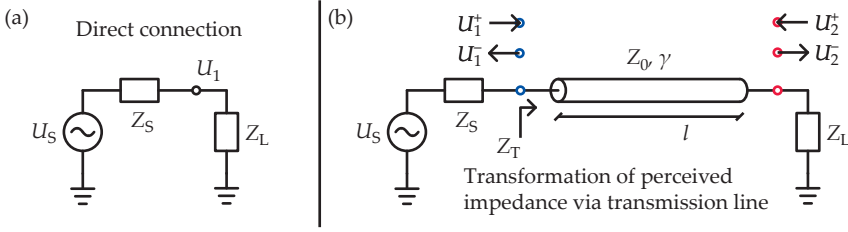
Figure 1.3: (a) A discrete load connected to a signal source, and (b) an illustration of a transmission line interfacing the source and load.

power level, assuming matched devices, as

$$P_{\text{Rx}} = \frac{G_{\text{A,Rx}} \sigma \lambda_0{}^2 G_{\text{A,Tx}}}{d_{\text{c,Rx}}{}^2 (4\pi)^3 d_{\text{c,Tx}}{}^2} P_{\text{Tx}}, \tag{1.7}$$

where σ denotes the radar cross-section of a target, $d_{\text{c,Tx}}$ is the channel-distance between the radar transmitter and the target, and $d_{\text{c,Rx}}$ the corresponding radar receiver channel-distance [6]. Once again, the signal must be strong enough to be detected at all and the received SNR will determine the accuracy of the detected targets.

1.3 MATCHING AND TRAVELLING WAVES

To make a link budget or performance prediction, as discussed above, knowledge of the device characteristics is required. First of all, an RF device must be able to accept power in order to transfer it. For this purpose, the input of the device under test (DUT) will load the output of a signal source, as illustrated in Figure 1.3(a). Given a continuous-wave (CW) generator with a source impedance, Z_{S}, and an electromotive force, U_{S}, the target is typically to select the load impedance, Z_{L}, so that it can accept all the available power, P_{AvS}, from the source. By node-voltage/branch-current analysis, the maximum transferred power is achieved when the load impedance is the complex conjugate of the source impedance, $Z_{\text{L}} = Z_{\text{S}}{}^*$. If the impedances are real-valued, i.e. $\text{Im}\{Z_{\text{L}}\} = \text{Im}\{Z_{\text{S}}\} = 0$ where $\text{Im}\{\cdot\}$ is the imaginary part operator, the matching simply corresponds to equating the real parts, i.e. $\text{Re}\{Z_{\text{L}}\} = \text{Re}\{Z_{\text{S}}\}$ where $\text{Re}\{\cdot\}$ is the real part operator. Conjugate matching ensures that the power delivered to the load, P_{L}, is all that which is available from the source, $P_{\text{L}} = P_{\text{AvS}} = |U_{\text{S}}|^2/(8\,\text{Re}\{Z_{\text{S}}\})$.

In the RF spectrum, however, signals are typically routed using transmission lines, as shown in Figure 1.3(b), and propagate as waves. This transmission line has a characteristic impedance, Z_0, a propagation constant,

γ, and a length, l. Further, the propagation constant, $\gamma = \alpha + \mathrm{j}\beta$, consists of an attenuation, α, and a phase constant, β; j denotes the imaginary unit. Provided that the equivalent series impedance per unit length, Z', and the corresponding shunt admittance, Y', is known, the characteristic impedance and propagation constant of a line can be calculated, as

$$Z_0 = \sqrt{\frac{Z'}{Y'}}, \tag{1.8}$$

and

$$\gamma = \sqrt{Z'Y'}, \tag{1.9}$$

respectively.

At an arbitrary position on the line, the voltage phasor, U, is accompanied by a current phasor, I. If there are signals travelling in both directions on the transmission line, the voltage can be modelled as an effective forward phasor, U^+, together with one travelling in the backward direction, U^-, where $U = U^+ + U^-$. Propagation of the phasors over a distance, l, are proportional to advancing and retreating complex exponentials, $\exp(\mp\gamma l)$, respectively; the time convention $\exp(\mathrm{j}\omega t)$ is used, where $\omega = 2\pi f$ is the angular frequency, and t denotes time. By contrast to the voltage phasors, the corresponding currents, $I^+ = U^+/Z_0$ and $I^- = U^-/Z_0$, interfere destructively, $I = I^+ - I^-$.

As a consequence from wave propagation on transmission lines, an RF signal on the port of a DUT can typically not simply be set. Instead, the signal has to be transmitted towards the port via a transmission line which inflicts loss and phase-delay, as $U^+(l) = U^+(0)\exp(-\gamma l)$. At the interface to the load, only part of the signal power will typically be accepted as a combination of forward and backward signal will be needed to obey all impedances at this point. The voltage reflection coefficient, Γ_f, describes the complex ratio of the impinging, U^+, and reflected voltage phasors, U^-, at an interface from a transmission line and into a load impedance, Z_L, and is calculated as

$$\Gamma_f = \frac{U^-}{U^+} = \frac{Z_L - Z_0}{Z_L + Z_0}. \tag{1.10}$$

In effect, from the reflection and propagation characteristics [7], the perceived impedance through the transmission line, Z_T, is typically not identical to that which loads the other end, Z_L, as

$$Z_T = Z_0 \frac{Z_L + Z_0 \tanh(\gamma l)}{Z_0 + Z_L \tanh(\gamma l)}. \tag{1.11}$$

Returning to the matching problem in Figure 1.3(b), it is the perceived impedance which must be conjugate matched to that of the source. It is

important to understand that, even under conjugate matching, direct reflection analysis using (1.10) between the source and load impedances does not generally show zero reflection, but this is not required in the discrete representation. Nonetheless, if desired, such a zero-reflection is found for power waves [8–11]. To avoid the transcendental behaviour of (1.11), the load can be matched to the line, $Z_L = Z_0 \Rightarrow Z_T = Z_L$. Some of the available power will, however, generally be lost since this will require the source to operate into that same impedance. The alternative is to co-design the source, transmission line, and load to provide the best possible implementation. Since a transmission line always will have some loss, the optimum co-design in terms of efficiency will be to remove it, $l = 0 \Rightarrow Z_T = Z_L$. This has the challenging implication that the source output must be fabricated directly connected to the load, as was indicated in Figure 1.3(a). Another, more traditional, co-design alternative is to design the length and impedance of the transmission line to transform the perceived load into the complex conjugate of the source impedance, $Z_T = Z_S{}^*$.

Any of the above solutions are suitable for CW operation. If steady-state CW analysis is not applicable, however, the reflection and transmission characteristics of a device is not always easily understood from a frequency-domain (FD) perspective. This will be discussed further in Chapter 2.

1.4 ULTRA-SHORT WAVELETS

Up to this point, e.g. as suggested by (1.4), it has been established that any performance in a wireless system partially must stem from the SNR and bandwidth of the utilised RF signal. Traditional systems utilise a CW steady-state signal with controlled amplitude or phase variation about a carrier frequency to define radio symbols. Such FD systems typically depend on homo- or heterodyne methods for frequency and phase detection, requiring relatively long symbols and complex circuits for signal synthesis and detection. By contrast to FD systems, a time-domain (TD) system is generally one which utilises short-enough symbols to render conventional phase and frequency detection problematic. Benefits of pulse-based TD implementations is high performance and simple signal processing, as compared to FD counterparts. Specifically, TD systems utilising short RF pulses can provide more direct system implementations. For example, a traditional FD radar typically performs consecutive CW measurements, synthesises a virtual pulse from the whole data set, and finally analyses the respective time required for it to travel to the target and back. The corresponding TD method is simply to transmit an ultra-short RF pulse and measure the delay until it returns.

A short RF pulse with a significant relative bandwidth is a TD signal and
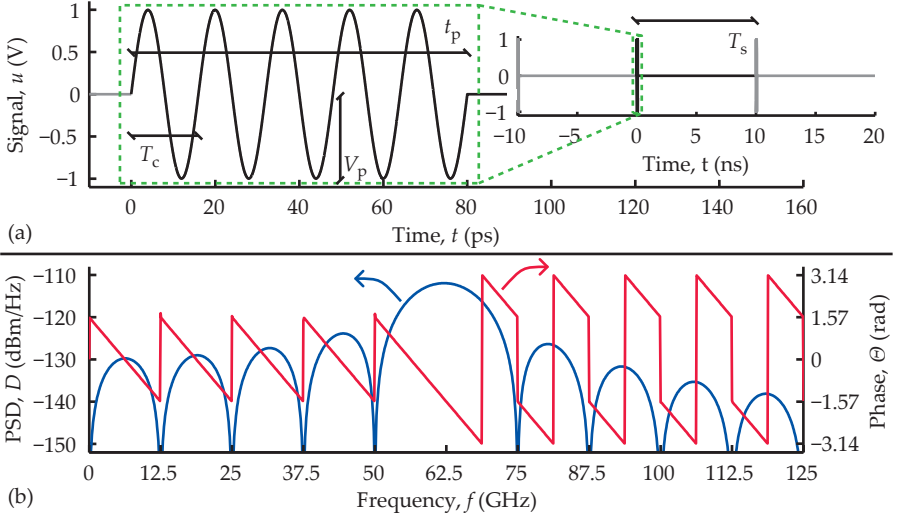
Figure 1.4: (a) A $t_p = 80$-ps length $f_c = 1/T_c = 62.5$-GHz carrier wavelet and an inset which illustrates the full $T_s = 10$-ns signal period. (b) Analysed PSD and phase response for one signal period of this wavelet signal.

can be referred to as a "wavelet"; a sampling oscilloscope can be utilised to capture it. An example wavelet is illustrated in Figure 1.4(a), with a $f_c = 62.5$-GHz carrier frequency, $t_p = 80$-ps pulse-length, and $V_p = 1$-V pulse amplitude. The envelope of the wavelet is rectangular, fitting five $T_c = 1/f_c = 16$ ps harmonic carrier oscillation periods, and the full signal period is $T_s = 10$ ns; the significant characteristics are the short pulse-length, $t_p < 10T_c$, and low duty-cycle, $t_p/T_s < 1\%$. This TD transient signal, u, has an equivalent FD spectral phasor representation U, as shown in Figure 1.4(b), which can be found through Fourier analysis, $U = \text{FA}\{u\}$. The phasor can be factorised into a magnitude, $|U|$, and a phase, Θ, and is in this notation $U = |U| \exp(j\Theta)$. Its PSD, D, is spread over a wide bandwidth, where the offset frequency, $f_p = 1/t_p$, defines the periodicity of magnitude nulls around the carrier; the maximum $U = -112$-dBm/Hz level occurs about the carrier frequency. The phase response of the wavelet is also shown in Figure 1.4(b) and the linear slope is $\partial\Theta/\partial f = -\pi/f_p$. As a non-phased spectral phasor is centred about zero delay, this phase-gradient can be found from the minimum group-delay, $\tau_g = -\partial\Theta/\partial\omega$, required to offset the signal to have causal time-domain support. Given the spectral phasor, Fourier synthesis can be utilised to reconstruct the actual transient waveform, $u = \text{FS}\{U\}$. For discrete signals sampled over a finite period, the Fourier transform operations imply TD periodicity [12].

One interesting aspect of any FD spectral magnitude, signal or transfer-function, is that it has a corresponding minimum-phase, $\Theta_{\min}$. This defines the most TD compact causal signal or impulse-response that is possible given the spectral magnitude [13]. Impulses and rectangular wavelets are minimum-phase and any phase distortion will thereby smear them temporally, voiding some of their potential TD benefits.

2

Millimetre-Wave Applications

$\mathcal{N}$o device or circuit will benefit the general society unless it is implemented to create or improve a useful application. In electrical engineering, this typically starts at fundamental device research and develops into application-specific circuit design in large-scale parallel fabrication processes. To bridge these two stages, it can be interesting to evaluate the circuit performance in simplistic experiments with off-the-shelf components.

Devices and circuits that can be used to generate and transmit wideband millimetre-wave (mmW) wavelet signals are studied in this thesis. To demonstrate their potential, applications which can be facilitated by use of a burst of radio frequency (RF) power instead of continuous-wave (CW) signals must be explored. Fortunately, as found in Chapter 1, the achievable performance in most applications is proportional to the utilised signal bandwidth. To access large bandwidths in practice, implementations operating at unlicensed bands in the mmW spectrum, 30–300 GHz, can be considered [14,15]. In the studies described below, to allow freedom in exploration, spectrum regulations and full system implementations are generally neglected.

2.1 TIME-DOMAIN CHARACTERISATION

One application which can be alleviated by use of time-domain (TD) wavelet signals is device characterisation. When characterising RF circuits or devices, they are typically described as multi-port networks [7]. For a complete description, the port reflection coefficients, Γ_f, must thereby be accompanied with transfer-functions, H_f, between the different ports. It is important not to confuse this RF transfer-function with the low-frequency transfer-function
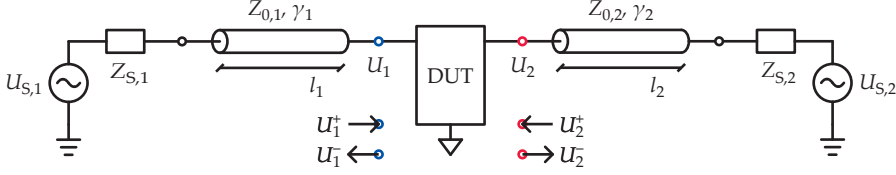
Figure 2.1: Schematic illustration of a two-port DUT that is connected to sources via interfacing transmission lines. The port signals are indicated, and decomposed into impinging and departing phasors.

which relates the total port signals. The frequency-domain (FD) scattering matrix, S_f, is an equivalent, compact, and standard description of the linear, time-invariant (LTI) reflection and transfer characteristics; the diagonal terms are reflection coefficients while the non-diagonal matrix entries are the transfer-functions between the respective ports.

A two-port device under test (DUT) is shown in Figure 2.1, via transmission lines connecting two power sources, with impedances, $Z_{S,k}$, as well as electromotive force phasor densities, $U_{S,k}$. The characteristic impedances and propagation constants of the interfacing lines are $Z_{0,k}$ and γ_k, respectively. Let the source interfacing port $k = 1$ generate a finite signal and that at port $k = 2$ be passive, i.e. acting as a load. In such a setup, the active source is launching a forward signal that appears as an impinging voltage phasor at port 1, U_1^+, with an implicit current related via the characteristic impedance. By effect from the impinging signal on port 1, there will also be a reflected departing phasor, $U_1^- = \Gamma_f U_1^+$, and a transferred departing phasor on port 2, $U_2^- = H_f U_1^+$. This departing signal will propagate along the transmission line and ideally be absorbed by the load. If there is imperfect matching between the load and output transmission line impedances, there will also be a non-zero impinging signal returning to the output, U_2^+. Further, if the DUT is not symmetric and reciprocal the reflection and transfer characteristics, respectively, will also depend on the direction of the excitation.

Two antennas facing each other over a free-space channel represent a simple, passive, LTI two-port DUT. If the antennas are identical and face each other in inverted polarisation, the same but arbitrary angles of departure and arrival can be probed. By sending an impinging wavelet signal, u^+, to the input port of this DUT, characterisation in the TD can be attempted [16]. This will produce a predictable departing output signal, u^-, through a linear transformation via the transfer-function in the FD. In the TD, the impulse-response, h_t, determines the relation between the impinging input and the departing output in a convolution, $u^- = h_t * u^+$. As for signals, Fourier

analysis and synthesis, $H_f = \mathrm{FA}\{h_t\}$ and $h_t = \mathrm{FS}\{H_f\}$, respectively, can be used to go between the FD and TD representations. It is important to keep in mind that discretisation in one domain will fold the other periodically, or vice versa [12].

A qualitative comparison of the signal distortion in mmW leaky-lens antennas, as compared to inherently dispersive pyramidal horns, was studied in Paper I. This extremely wideband antenna was found to closely reproduce $t_\mathrm{p} = 100$-ps pulse-length rectangular wavelets with carrier frequencies from $f_\mathrm{c} = 45$ to 75 GHz, as intended [17]. Similar measurements can be performed to identify the frequency dependent delay of a two-port [18].

The characteristics of a stable LTI system always have a unique inverse and can thereby be found by comparison of the input and output signal under an arbitrary, but known, input [12]. To characterise the transfer-function using narrowband signals over a range of frequencies, consecutive CW analyses may be utilised. Traditionally, a vector network analyser (VNA) is utilised to characterise devices and circuits in the FD. An amplitude and phase reference is needed to deduce the inherent reflection and transmission properties of the DUT alone. This is provided by a calibration procedure, which typically moves the measurement reference planes to appear at the ends of cables, for the case in Figure 2.1, or a similar probed interface. Calibration by at least three terminations per port, including inter-port connections, must be utilised for this purpose, identifying any parasitic network which can be de-embedded from the DUT characteristics [7]. Band-limited impulse-response studies can thereby be realised by transforming the transfer-function from a VNA measurement [19].

It can be attractive to utilise wavelet signals to perform direct TD network analysis [16]. However, noise captured in an actual measurement will add uncertainty to the estimation of the DUT characteristics [20]. Such influence can be reduced by, e.g. parametric or iterative filters [21, 22]. Simulations is the easy solution for passive devices such as simple antennas, eliminating any complication of limited signal-to-noise ratio (SNR) in a measurement scenario [23]. In some situations, having acquired the impulse-response, gating by means of a window function in the TD can be used as a complement to the calibration [24]. This works by the duality principle that a calibrated excitation in the FD is mathematically equivalent to the corresponding band-limited impulse excitation in the TD.

The most easily applicable implementation of gating is that where discrete impulse-response features are located at delays well separated from the targeted ones [25]. For example, multi-path propagation in a radio channel will add impulse-response features at large delay, as compared to the line-of-sight transfer characteristics. These multi-path components can be removed if the free-space characteristics are of interest. However, it is important to

extend the gate to include all the reactive responses from the targeted direct path. As an example, consider the distortion effects on the rectangular wavelet in Figure 1.4 when passed through a first-order numerical filter, as shown in Figure 2.2. When inserted directly between a matched source and load, achieving a $Q = 5$ quality factor, the filter disperses the signal due to its limited bandwidth. Cascade connection of a matched transmission line, approximately a $l = 20$-mm long teflon-based coaxial cable, adds delay and minor attenuation to the response. However, if the characteristic impedance of the transmission line is mismatched to the source and load, illustrated here for a $\Gamma_f = -10$ dB reflection coefficient, there will be a more severe distortion to the response. First, a signal directly driven by the source will pass through the filter and propagate to the load interface. Only part of that signal is accepted in the load due to the non-zero reflection coefficient and the remainder will go back to the filter, where another reflection will occur. A round-trip reflection response will thereby return to the load, and the cycle will repeat itself infinitely. The result at the load is a train of signal responses of diminishing amplitude and separated by twice the direct delay of the transmission line. A similar reactive mechanism will occur for any arbitrary DUT of finite size and non-perfect matching. Note that the standard $\Gamma_f = -10$-dB-level for matching produces quite significant round-trip responses unless the transmission line attenuates them. If a device with an impulse-response that consists of several discrete features is excited by a wavelet, the effect will be an output that consists of as many signal components of various shapes and delays. Mismatch in the setup about the DUT will produce additional round-trip propagation responses trailing each signal component, as illustrated for one wavelet in Figure 2.2.

An attempt to combine wavelet excitations and a well-defined gating environment for device characterisation is described in Paper II. Symmetric antenna links were used as DUTs and provided illustrative examples of the need for noise awareness in de-convolution problems. In combination with setup scattering, this required gating techniques in both TD and FD. Special care in the choice of filter and gate functions should be taken [26], as the properties in the TD are reciprocal to those in the FD. It was found that the proposed wavelet-based TD characterisation method, with just one thru reference, can be used to find approximate DUT parameters. The described method requires inclusion of additional reference measurements to be applicable on arbitrary DUTs, e.g. a multi-line calibration [27]. However, the utilised controlled gating by itself provides an additional analysis layer for any wideband FD VNA measurement.

Other applications for TD measurements and signal processing include free-space material characterisation and radar imaging. The former requires knowledge of the geometry to find the electromagnetic properties, e.g. relative
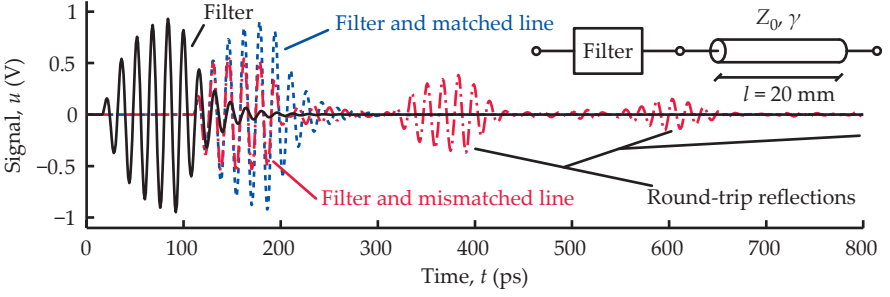
Figure 2.2: Calculated distortion of a rectangular wavelet passed through a first-order series bandpass filter. Also shown are cases where the filter is cascaded by a matched or mismatched ($\Gamma_f = -10$ dB) transmission line. A matched line only delays and attenuates the response, while a mismatched line also produces a train of round-trip propagation responses.

permittivity, ε_r, of the sample [28, 29]. Assumptions of the environment are required in the latter to identify probable positions of any targets. Both can be useful for non-destructive testing purposes.

2.2 HIGH-SPEED WIRELESS COMMUNICATIONS

Wireless communications is another application area that can benefit from the use of TD signals. Vast network infrastructures have been developed for wireless digital communications, and continue to evolve to support more users and higher data-rates. For local synchronisation of data and streaming of high-definition video, wireless links with capacities of several Gb/s per user in wireless local area network (WLAN), wireless personal area network (WPAN), or piconet applications are attractive [14, 30]. Internal chip-to-chip communications between modules on a motherboard or board-to-board communications in servers also demand Gb/s per chip or board, respectively. Already, regulations for Gb/s data-rates are developed [31], but as demands on wireless service increase, an approach towards Tb/s data-rates will be required in future short-range links [2]. To meet this demand, the upcoming fifth generation wireless system (5G) framework is expected to be diverse, spreading functionality over different bands [1]; this is one step towards an eventual mitigation of wireless capacity into the terahertz spectrum [32]. Also, new wireless system principles such as massive multiple-input multiple-output (MIMO) provide opportunities in spatial multiplexing via array technologies [33].

Returning from the visions and investigating realised systems, long-haul

fibre networks have capacities in the Tb/s range [34], connecting servers world-wide. In the cellular networks, mmW wireless back-haul can constitute last-mile wireless pencil-beam links for the distribution of network access to rural base-stations and local access-points in urban areas [15,35]. However, a base-station is broadcasting on various channels and codes to deliver network access to a number of portable devices in its cell. This results in a data-rate per user which in many cases is limited to a few Mb/s in current implementations. Improving on this, recent regulations for short-range wireless communications in the 60 GHz band, i.e. IEEE 802.11a and 802.15.3c, have motivated implementations which can achieve a handful of Gb/s [36–39].

Attempting to satisfy the projected demands [2], energy-efficient transceivers with increased capacity must be developed. Consider the transmitter and receiver front-ends illustrated in Figure 2.3(a); digital data is provided by an external circuit and the wireless system must deliver it to the recipient with a minimum amount of errors. The data is carried in radio symbols over the channel and there are in principle two options to provide a high data-rate. The one is high-order modulation in a power limited scenario, and the other is a rapid transmission of binary symbols in a bandwidth limited case, as was discussed in relation to (1.4). The first requires a high-order modulation technique such as quadrature amplitude modulation (QAM) to carry many bits in each symbol. A common option is 16-QAM, illustrated in Figure 2.3(b), where four bits are programmed into the phase and amplitude of each symbol. The second option is to use a high symbol-rate and send a serial data-stream containing one bit per symbol, i.e. a binary modulation. A simplistic alternative is to use on-off keying (OOK), i.e. the full-level binary amplitude-shift keying (ASK) extreme where the signal simply is turned on and off, and the demodulation procedure is thereby only energy detection and threshold comparison, as illustrated in Figure 2.3(c). To achieve the same data-rate, a system using binary OOK modulation must operate at a higher symbol-rate than the high-order 16-QAM simile. The trade-off is that more control of the transmitted signal and more intricate receiving schemes are required for the high-order modulation, which typically increases the total direct-current (DC) dissipation. This thereby degrades the energy-efficiency (EE) of the system, which is the quotient of the average dissipation over the bit-rate, requiring more energy per transmitted amount of data.

Wireless communication at multi-Gb/s data-rate was demonstrated in Paper III, utilising an efficient mmW wavelet generator and a simple detector. The utilised modulation is OOK, but also including an impulse-radio scheme. The presence or absence of a short wavelet in the symbol interval sets the value of the corresponding bit; a 7.5-pJ/b transmitter EE was achieved at 4-Gb/s data-rate as the front-end is dormant during parts of the radio symbols. In effect, impulse-radio schemes conserve the DC dissipation and also lowers
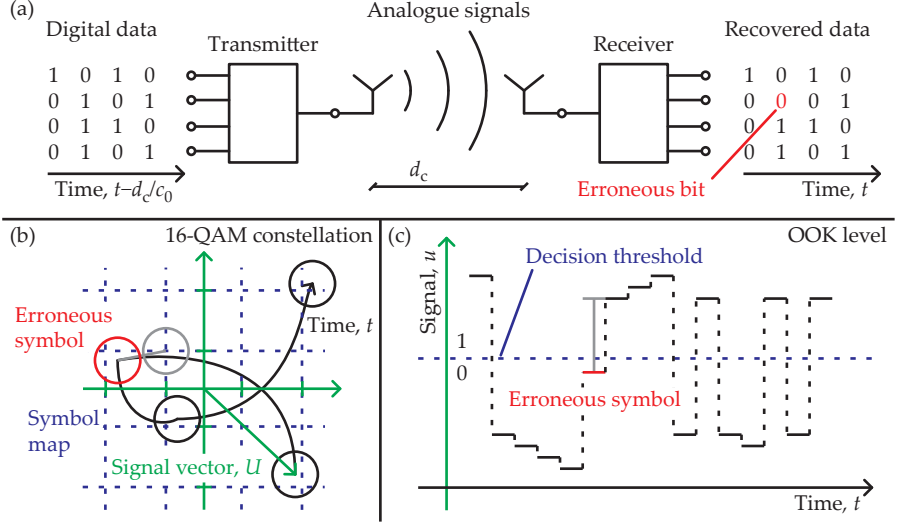
Figure 2.3: (a) A schematic wireless communications setup, showing the transmission of digital data via analogue signals over the radio channel. The data can be transferred using (b) a high-order modulation such as 16-QAM, or (c) a binary modulation such as OOK.

the root-mean-square (RMS) radiated power to better comply with spectrum regulations. The transmitter front-end circuit in Paper III is simplistic, it operates by switching an oscillator on and off, directly converting input baseband pulses to short RF wavelets. A similar but improved generator circuit, as well as a more wideband and sensitive receiver, was used for OOK communication in Paper IV. Replacing the impulse-radio scheme with a higher symbol rate, this allowed for 15-Gb/s data-rates over an up to $d_c = 1.5$-m wireless link with an acceptable bit-error rate (BER). In combination with a state-of-the-art transmitter EE of 1.55 pJ/b, the results promise high-speed energy-efficient wavelet communications. The utilised receivers are based on gallium arsenide (GaAs) Schottky diode detectors, operated at zero-bias. Diodes in antimony (Sb) technology may provide further sensitivity and efficiency [40]. Combining a diode detector with an amplifier, communication over longer distances can be facilitated at the cost of DC dissipation, and integrated implementations already exist in the terahertz spectrum [41].

The state-of-the-art in front-end circuits for short-range mmW wireless multi-Gb/s communications was reviewed in Paper IV. Benchmarking of various wireless circuit technologies for objective comparison requires suitable and meaningful figures-of-merit. Transmission tests typically utilise some best-effort line-of-sight antenna link, or even wired path, that sets the realised

link distances. Often, the actual antenna link in an implementation will have little in common with this test setup. To eliminate this complication, calculation of the intrinsic system omni-distance, $d_{c,i}$, can be useful. This scales the achieved link distance via (1.1) to the corresponding result utilising lossless omni-directional antennas, as

$$d_{c,i} = \frac{d_c}{\sqrt{G_{A,Rx} G_{A,Tx}}}, \tag{2.1}$$

which can be used to better compare front-end systems. Since the possible link distance increase with the output power and sensitivity of the front-ends used, so does the maximum omni-distance. Further, the DC power dissipation of the transmitter and receiver front-ends are interesting, but not as much as the energy per bit as described by the EE. Normalising EE over the omni-distance provides a final figure-of-merit that investigates the simultaneous capability to achieve performance in range, data-rate, and DC dissipation. In communications, it is further important to utilise a pseudo-random binary sequence (PRBS) of sufficient length to simulate data, otherwise the result will not reflect the real performance of a transceiver.

In general, implementations utilising OOK and high symbol-rates provide the best EEs [42–46], as low as 6.3 pJ/b at a total DC dissipation of 68 mW. At low symbol-rate, by contrast, the over-long binary symbols just consume more energy to over-determine each bit. Similar results and arguments are related to 2-ASK system implementations [47–50]. The best omni-distance found for the systems using low-order modulations is 54 mm, while the best EE normalised by the omni-distance is 0.29 pJ/bit/mm. Systems that utilise high-order modulations require front-ends that achieve phase synthesis and detection. The corresponding added circuit complexity will require more power to operate, for example as demonstrated in quadrature phase-shift keying (QPSK) [35–37, 51]. Addition of multiple amplitude stated allows additional data in each symbol, but also increases the circuit complexity further, which is paid in DC dissipation for high-order QAM transceivers [38, 39, 51, 52]. The best omni-distance achieved in these QAM systems is 126 mm, while the corresponding DC dissipation is 450 mW; EE normalised by the omni-distance is 0.22 pJ/bit/mm. Throughout the literature studied, the mmW output power levels are typically from 0 through 10 dBm. By contrast, the receiver sensitivities for the QAM front-ends can be below -50 dBm, compared to typical values about -30 dBm for those operating in high-rate binary modulations. If range is crucial, a QAM system is preferable due to the better receiver sensitivity possible for long symbols. A binary TD communications system can instead offer an improved static dissipation, suitable for battery powered devices.

3

Efficient Wavelet Generators

$\mathscr{H}$IGH-POWER energy-efficient signal synthesis, is required to achieve range and portability in wireless systems. Performance, however, can also be provided by the signal bandwidth, e.g. pulsing the source to produce wavelets. A wavelet generator can consist of an oscillator core and a means to rapidly switch it on and off. However, signal generation with a carrier frequency, f_c, in the millimetre-wave (mmW) spectrum is challenging as modern transistor technologies typically have cut-off, f_t, and maximum oscillation frequencies, f_{max}, of a few hundred gigahertz. By adding compound semiconductor (III–V) devices to the silicon (Si) circuits in the radio frequency (RF) front-end, alternative performance trade-offs can be made available. This is especially beneficial for systems targeting efficient signal generation at carrier frequencies scaled towards terahertz.

3.1 DIODE OSCILLATORS

A feedback loop that promotes self-oscillations at a certain carrier frequency can be implemented in any transistor technology. Such a circuit can in its simplest form be described as an electrical negative differential conductance (NDC) element, which generates power, in combination with a resonance circuit that sets the frequency. Digital methods for monitoring and tuning of the generated frequency, phase, and amplitude have been researched and implemented for integrated mmW radios [53]. Devices in Si based complementary metal-oxide-semiconductor (CMOS) technologies are excellent for such arithmetic implementations, and can support oscillator performance up to reasonably high frequencies.

An oscillator core primarily demands a sufficiently high maximum oscillation frequency, $f_{max} > f_c$, to provide feedback amplification. In a standard $Z_0 = 50$-Ω environment, however, the cut-off frequency must also be high, $f_t > f_c$, to provide current gain in the interface to the transmitter antenna. A buffer or power amplifier may be desirable to isolate the output or boost the output power, but additional circuits also translate into an increased direct-current (DC) power dissipation. This is problematic for battery powered units where as much of the available energy as possible must be used in computations or to transmit information via wireless signals, instead of dissipating into heat.

Instead of NDC from electrical feedback, there are several physical sources of NDC in the form of semiconductor diodes. In the late 1950's, the Esaki diode was discovered to provide NDC characteristics from quantum mechanical inter-band electron tunnelling [54]. Similar NDC behaviour was soon discovered in the Gunn diode [55], stemming from the transferred electron effect. Through implementation of the intra-band resonant-tunnelling diode (RTD) [56], a device structure that present NDC and can provide both high carrier frequency and conversion efficiency was realised.

An RTD consists of a quantum well defined between two narrow potential barriers in the conduction or valence band of a semiconductor heterostructure. In the well, as illustrated in Figure 3.1(a), discrete sub-bands with bound states are formed due to quantum confinement. Thinner or lower barriers increase the probability of tunnelling transport through the double-barrier structure. Resonant-tunnelling requires that there is an empty state on one side of the RTD that matches a bound state in the well and the state of an electron on the other side. Under such conditions, the electron can tunnel directly via the bound state to the other side of the heterostructure, and add to the collector current density, J_C. This resonant-tunnelling conduction mechanism is more effective than indirect processes that require additional scattering. Although the diode can be symmetric, a specific emitter is typically designed to provide a high density of electrons, as compared to the collector. A collector-emitter voltage, V_{CE}, must be applied to bias the structure and eventually level the ground-state with the emitter reservoir, but this energy level can be also be offset by inclusion of a notch in the well.

Band diagram illustrations under various bias conditions are sketched in Figure 3.1(a-c) to conceptually explain the schematic non-linear RTD current-voltage characteristic in Figure 3.1(d). At zero-bias, the ground-state typically resides above the emitter and collector terminal potentials, as illustrated in Figure 3.1(a), and no net current flows. Application of a bias voltage lowers the potential of the collector and generates a band bending where the bound states approach the available carriers in the emitter. Thereby, cf. Figure 3.1(b), the first resonant-tunnelling current peak is achieved when the ground-state
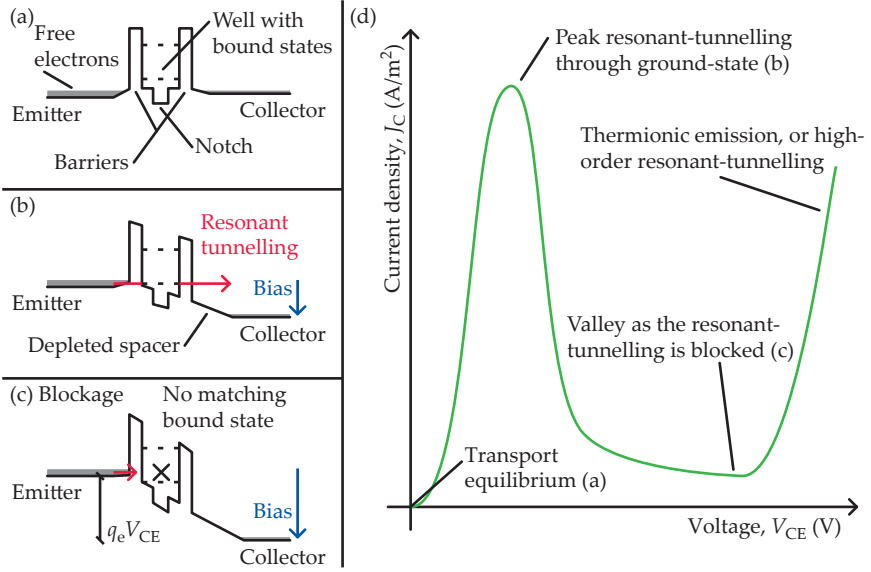
Figure 3.1: Band diagram illustrations of an RTD at (a) zero, (b) peak, and (c) valley bias. (d) Schematic current-voltage characteristics.

in the well is biased close to the conduction band edge on the emitter side of the diode. The bias scale is primarily determined by the level of the bound state, but skewed or scaled by any series resistance or distributed band-bending. Above the peak, cf. Figure 3.1(c), the current decreases as the matching bound states are shifted away from the available carriers. At substantially increased bias, higher sub-bands or thermionic emission over the barriers may contribute to additional resonances or barrier diode behaviour, respectively.

The options to design the energy level and coupling of the bound states in III–V materials makes this device attractive for mmW signal generation [57]. The high-mobility characteristics in the indium–gallium–arsenide (In–Ga–As) and indium–aluminium–arsenide (In–Al–As) material systems are of special interest. Using aluminium arsenide (AlAs) barriers and an indium arsenide (InAs) notch in the quantum well, such RTD oscillator implementations are promising in terms of output power and efficiency [58]. Also, this comes in combination with scalability throughout the mmW spectrum and into the terahertz region [59].

An In–Ga–As/ AlAs/ InAs RTD is utilised in the oscillator core that is implemented in the circuits presented in this thesis; the heterostructure specification and fabrication scheme is elaborated in Appendix A. Measured
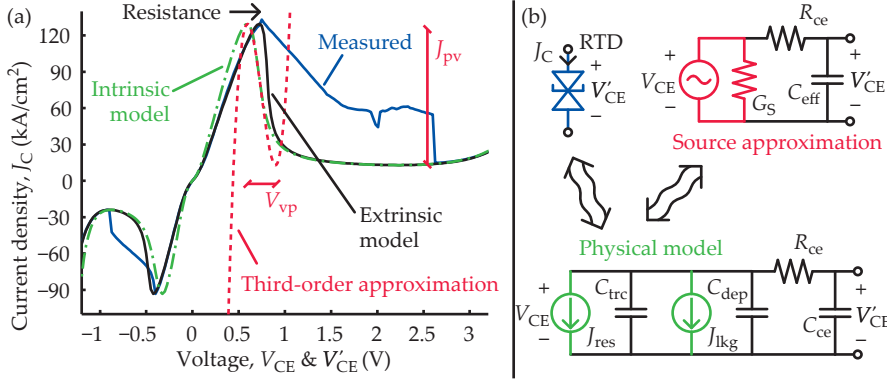
Figure 3.2: (a) Measured and modelled, with and without series resistance, current-voltage characteristics of an RTD; also shown is a third-order approximation of the NDC region. (b) Schematic of a physical model and the small-signal source approximation.

DC current-voltage characteristics of a fabricated RTD with $A_{\text{eff}} = 21.5\text{-}\mu\text{m}^2$ active area is shown in Figure 3.2(a). An asymmetry can be observed due to differences in the collector and emitter layers. This RTD has a 129-kA/cm^2 peak current density in the forward direction; the peak to valley current ratio is 10.0 and it presents NDC over a bias range of almost 2 V. Note that the measured current in the NDC regions is not the true DC current but the root-mean-square (RMS) value of a continuous-wave (CW) oscillation with the measurement setup. Direct measurement of the RTD characteristics in the NDC region can be attempted by stabilising the device with series resistance or parallel conductance. Unfortunately, this is very challenging for devices with both high current density and high negative conductance; any such stabilisation attempt will risk to bury the targeted characteristics in the fabrication and measurement uncertainties.

Modelling is another approach that instead will rely on the validity of the models used. As illustrated in Figure 3.2(b), the RTD heterostructure can be described as a resonant-tunnelling current source, J_{res}, in parallel to a transit-charge capacitance, C_{trc}, both with non-linear dependence on the applied voltage [60]. A bias-dependent small-signal inductance is sometimes also introduced as part of the heterostructure model [61]. This inductance arises from charging dynamics in the heterostructure; this is disregarded here, i.e. electrostatic steady-state is assumed to occur with negligible delay in the RTD heterostructure. Such an approximation can be justified when the carrier frequency is relatively low compared to the self resonance of the RTD. Building on the model, leakage due to thermionic emission over the barriers

can be taken into account by an additional current source, J_{lkg}, and a depletion capacitance, C_{dep}, models the reactive influence of the bias-induced collector space-charge region. Finally, series resistance in the interfacing semiconductor mesa and in the semiconductor/ metal contacts, R_{ce}, as well as external capacitance between the collector and emitter contacts, C_{ce}, must be added. The fitted modelling result is shown in Figure 3.2(a), with and without series resistance that effectively skews the external voltage scale, V'_{CE}, in relation to the intrinsic, V_{CE}. Analytic modelling thereby allows an estimate of the intrinsic resonant-tunnelling current peak and its NDC region. Further details on the analytic RTD model are provided in Appendix B.

By fitting a third-order current-voltage characteristic to that of the intrinsic NDC current, a few interesting but approximative results can be found [62]. The optimum load conductance, $G_{L,opt} = -A_{eff}g_{min}/2$, which maximises the output power, can be found from the minimum differential conductance, g_{min}. Consequently, the maximum available power, $P_{AvS} = 3A_{eff}J_{pv}V_{vp}/16$, is determined by the peak-to-valley difference current density, J_{pv}, and the corresponding intrinsic valley-to-peak voltage, V_{vp}. Pursuing this modelling approach, the RTD current density can be approximated as

$$J_{C,approx} = J_0 - \frac{3J_{pv}}{2V_{vp}}\left(V_{CE} - V_0\right) + \frac{2J_{pv}}{V_{vp}^3}\left(V_{CE} - V_0\right)^3, \qquad (3.1)$$

where J_0 denotes a cosmetic shift to the mean of the measured peak- and valley- currents, and V_0 denotes another to overlap the modelled characteristics with the measured. As can be seen in Figure 3.2(a), the current densities and minimum conductance have been preserved by using an effective NDC voltage region $V_{vp} = -3J_{pv}/(2g_{min})$ instead of the actual range. The resulting under-estimation of the voltage range is more acceptable than an error in the differential conductance. This is because the latter dictates the maximum possible load that leaves any NDC available for power generation, $G_{L,max} = -A_{eff}g_{min}$.

The RTD used has a modelled $g_{min} = -4.88$-mS/μm^2 minimum differential conductance in the NDC and a measured $J_{pv} = 116$-kA/cm^2 difference-current density between the peak and valley. For the $A_{eff} = 21.5$-μm^2 device measured, this corresponds to a $G_{L,opt} = 62.1$-mS optimum load and an approximate available output power of $P_{AvS} = 1.52$ dBm. Further, n $R_{ce} = 4.7$-Ω series resistance was estimated from the modelling. Taking the third-order model one step further, the RTD can be approximated as a power source, as illustrated in Figure 3.2(b). The source conductance must, according to standard matching theory, be $G_S = G_{L,opt}$ since it maximises the generated power. There is, however, a degradation of this intrinsic third-order source approximation due to the external series resistance of the RTD. It further has

an effective capacitance, C_{eff}, that shunts the collector-emitter port and must be conjugate matched to set the carrier frequency, $f_c = 1/(2\pi\sqrt{C_{eff}L_{tnk}})$ of the generated oscillation, where L_{tnk} denotes the inductance presented in the tank circuit formed. This RTD oscillator can be used as the signal source in a mmW wavelet generator.

3.2 WAVELET GENERATOR CORE

One simple implementation for wavelet generation in the mmW spectrum is to bandpass filter short baseband pulses about the desired carrier frequency, e.g. as has been demonstrated in high electron-mobility transistor (HEMT) technology [63]. However, this is inefficient as much of the power is discarded. Implementations in various Si based transistor technologies are also possible. One example is injection-locked oscillators that can generate coherent signals by switching on and off in synchronisation with a reference clock [64, 65]. Pulse shaping from a CW oscillator, utilising any amplitude control circuit, is another option feasible in the mmW spectrum. One such method that limits the power dissipation by integrating an oscillator in combination with a dynamically biased buffer amplifier has been demonstrated [66].

Wavelet generator core circuits based on mmW RTD oscillators can be devised by introducing a means to rapidly regulate the effective NDC presented. This has been realised by integrating an In–Ga–As/ In–Al–As heterojunction bipolar transistor (HBT) switch in series with an RTD [67,68], providing a dynamic series resistance. Such an implementation avoids any significant energy dissipation when the diode is disconnected by the HBT, and any oscillation is quenched. However, the series configuration of the resonance and bias circuit utilised is not optimal for rapid wavelet start-up and quench. It provides a significant time-constant associated with on and off transitions, not readily allowing a rapid start-up and quench to generate ultra-short and coherent wavelet signals. Another solution is an epitaxially overgrown Schottky gate in the vicinity of an RTD in a gallium arsenide (GaAs) based technology [69–71]. Coherent wavelet generation, with start-up and quench in the time scale of the carrier oscillation period, is possible through utilisation of a parallel bias and resonance circuit. A more efficient core circuit implementation can be realised by integrating a metal-oxide-semiconductor field-effect transistor (MOSFET) switch in series with the RTD, providing a means to rapidly change the voltage division between the devices and thereby their common bias current. This allows the RTD to be disconnected when the MOSFET is operated in cut-off, due to a low control voltage, u_{Ctrl}, on the gate, achieving an off-state and minimal DC dissipation. To realise an on-state, the RTD can be switched in by application of a high control signal on the MOSFET gate. During wavelet
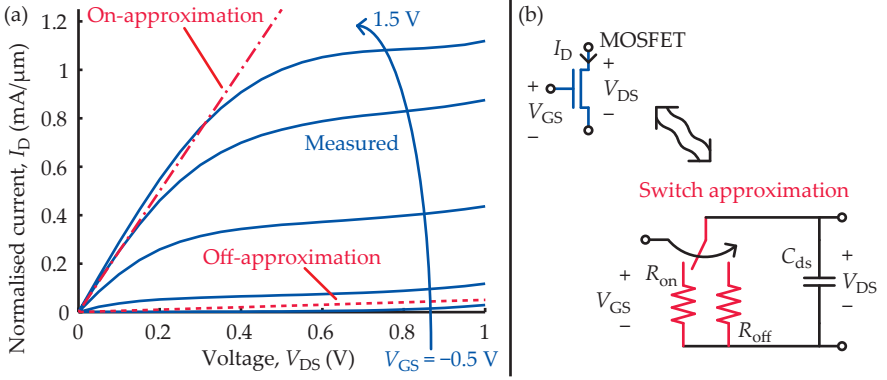
Figure 3.3: (a) Measured current-voltage characteristics of a 130-nm-gate-length MOSFET, with on- and off-approximations that represent switch operation. (b) Circuit schematic of switch approximation.

generation in the on-state, the current is limited by the RTD and the MOSFET thereby operates in the linear region.

To allow efficient and ultra-short wavelet generation in the mmW spectrum, a series configured RTD-MOSFET core circuit was pursued. An $In_{0.53}Ga_{0.47}As$ surface-channel MOSFET, on an $In_{0.52}Al_{0.48}As$ back barrier and indium phosphide (InP) substrate, was developed for this purpose in Paper V. One of the main processing steps in the MOSFET fabrication is utilisation of a dummy-gate on the channel layer. Epitaxial regrowth of access and support layers, subsequent low-resistance T-gate formation isolated from the channel by a thin dielectric, and contact deposition masked by the gate allows for formation of self-aligned contacts. The fabrication scheme is described more thoroughly in Appendix A. The result is 199-Ω–μm-low normalised on-resistance, 1.9-mS/μm-high extrinsic transconductance, and limit frequencies in excess of 240 GHz at 55-nm gate-length. Interestingly, for both digital and analogue applications in general, modern III–V surface-channel MOSFETs outperform HEMTs with regard to on-resistance and transconductance [72].

In the circuit implementations described in this thesis, the MOSFET is operated as a switch. The most important performance is thereby to modulate the drain-source resistance, R_{ds}, between suitable values when the control signal, u_{Ctrl}, that is fed to the gate is regulated. A 130-nm-gate-length device was chosen for this purpose, its current-voltage characteristics are shown in Figure 3.3(a). This MOSFET presents an approximate $I_D \approx$ 1-mA/μm normalised drain current saturation for V_{GS} = 1.5-V gate-source voltage. It is seen to have a normalised on-resistance better than 400 Ω–μm, while cut-off operation at approximately V_{DS} = 1-V drain-source voltage achieves
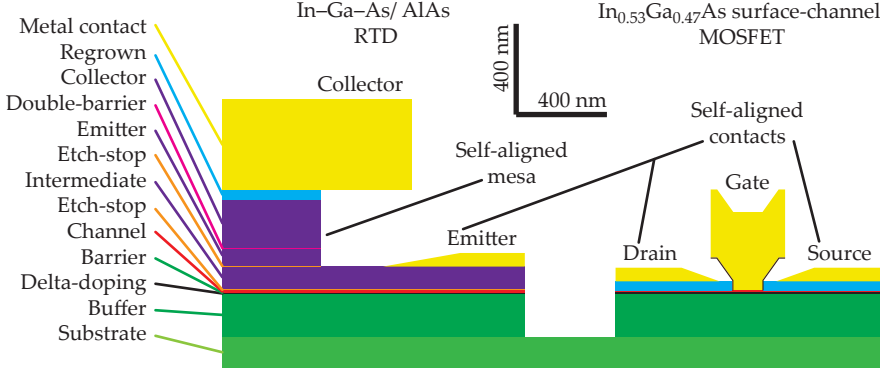
Figure 3.4: Schematic cross-section view of the RTD and MOSFET on InP sample surface. The devices are fabricated in parallel and additional layers remain to connect them as well as forming any circuit.

a normalised off-resistance of 20 kΩ–μm. In the implemented circuits, a 100-μm-wide MOSFET was used, it can thereby be approximated as an $R_{on} = 4$-Ω on-resistance or an $R_{off} = 200$-Ω off-resistance, depending on the control voltage as illustrated in Figure 3.3(b). To provide a somewhat realistic switching behaviour, a $C_{ds} = 82$-fF capacitance was implemented in parallel to this variable resistor, scaled from the model in Paper V. Physical transistor modelling is required for most other circuit implementations, but the above approximation is sufficient to capture the principal behaviour of the device when used in an RTD-MOSFET wavelet generator core.

3.3 WAVELET GENERATOR CIRCUIT

A monolithic process was developed to allow for the In–Ga–As/ AlAs/ InAs RTD and In$_{0.53}$Ga$_{0.47}$As surface-channel MOSFET to be fabricated in parallel. As illustrated on the mostly to-scale cross-section sketch in Figure 3.4, the heterostructure used features MOSFET layers at the bottom with those for the RTD on top. Observe that the final interconnections are not shown. The methods used to achieve these self-aligned devices are described in Appendix A. This process is a streamlined version of that used in Paper VI, where an efficient series-integrated RTD-MOSFET generator circuit was demonstrated.

To achieve a mmW generator circuit that can output ultra-short wavelets, the series-integrated RTD-MOSFET core must be shunted by a resonance and bias circuit. Starting from the core components in Figure 3.4, an interlayer spacer and two $t_m = 0.5$-μm-thick gold (Au) layers with a thin dielectric sandwiched in-between was utilised for this purpose, as illustrated in an
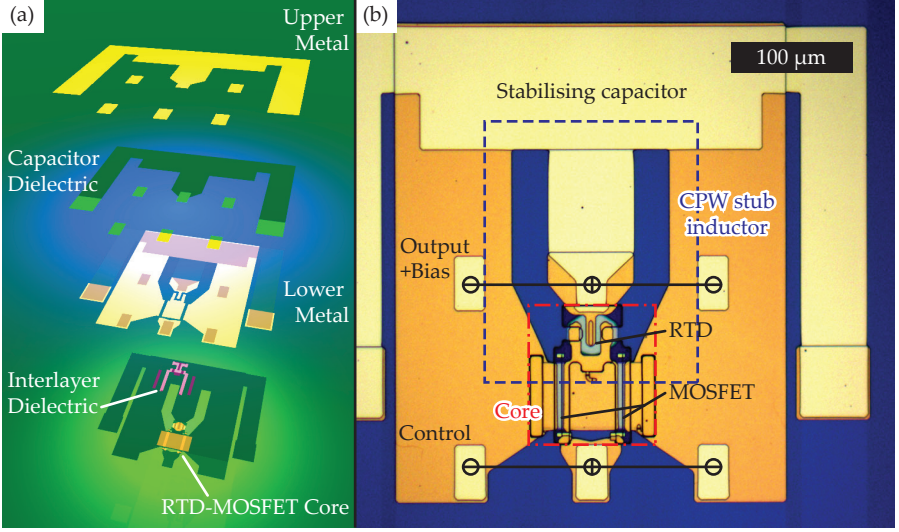
Figure 3.5: (a) Illustration of the RTD-MOSFET core on the sample surface with an expanded structure of the final circuit layers. (b) Chip micrograph of a fabricated wavelet generator circuit.

expanded projection in Figure 3.5(a). This achieves the assembly of a coplanar waveguide (CPW) stub inductor and a stabilising capacitor, as well as 100-μm-pitch ground-signal-ground point-contact probe pads, also shown on the chip micrograph of a fabricated circuit in Figure 3.5(b). Here, the lower pad is used for control signal, u_{Ctrl}, input to the MOSFET gate, while the upper is a combined RF output and circuit bias voltage, V_{Bias}, input. In effect from application of an approximately 1.2-V peak-to-peak baseband pulse to the control input, under $V_{\text{Bias}} = 1$–2-V-bias, the output signal, u, will typically oscillate while the input pulse exceeds the threshold of the MOSFET; wavelets are generated.

A circuit schematic that can be used to clarify the circuit design and operation is provided in Figure 3.6(a), representing probed operation of the on-chip mmW wavelet generator. The series-integrated RTD-MOSFET is shunted by a CPW inductor that utilises an RF short-circuit provided by the $C_{\text{tk}} = 710$-pF stabilising capacitance, which also is useful in pulsed operation [73]. The probe would ideally shunt the whole of the inductance, but only achieves to connect L_{tk} within the port due to its finite pitch. This leaves a small inductance, L_{tn}, that is not shunted by the load; the majority resides in the ground-track of the CPW interface connecting the core. The inductance, L_{tnk}, presented in the tank circuit formed together with the effective capacitance, C_{eff}, of the RTD is thereby that of an inductive tap to the probe interface. In

29
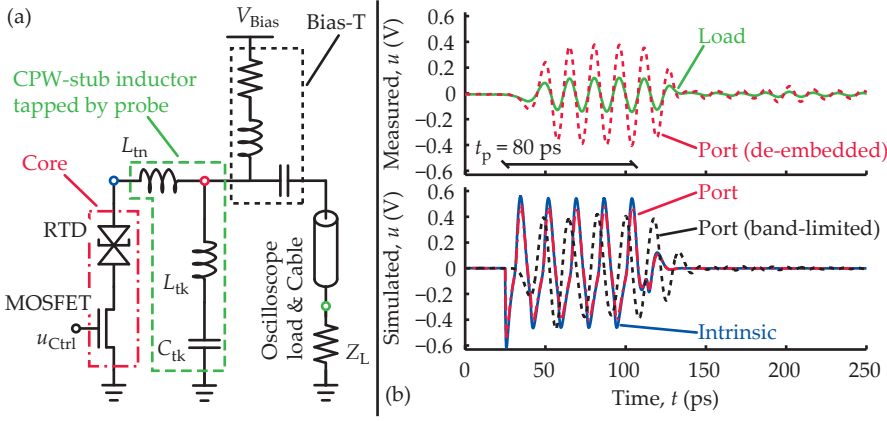
Figure 3.6: (a) An idealised schematic of the wavelet generator circuit loaded via a probe and a bias-T. (b) Measured and simulated $f_c \approx 64$-GHz wavelet generator output signals for $t_p = 80$-ps control signal pulse-length.

a probed implementation scaled towards terahertz, this tapping effect may limit the available output power. The probe further provides connection to a bias-T and, typically via a 30-in teflon-based coaxial cable, the 100-GHz $Z_L \approx 50$-Ω sampling-head of an oscilloscope. The total insertion loss from chip to oscilloscope is approximately 8 dB about $f = 60$ GHz.

The principal operation of the wavelet generator circuit can be described as follows. In the off-state, the cut-off MOSFET disconnects the RTD and the stabilising capacitor can be charged, its internal voltage approaching the external bias voltage, V_{Bias}. An impinging baseband pulse on the gate will switch the MOSFET to a highly conducting state, eventually entering the linear region as the core becomes current-limited by the RTD. This is the wavelet generator on-state; an oscillation will develop if the internal bias is sufficient to enter the NDC region and if the total conductance in the circuit can be negative. Further, while the RTD becomes switched in, the current demanded by the core will typically increase at a rate that cannot be allowed via the DC path of the bias-T. The approximately stepped increase in current is instead provided in part by the coupling capacitor in the bias-T, but primarily by the on-chip stabilising capacitor. This charge reservoir it is large enough to provide an approximately constant bias voltage throughout short-length pulses. The corresponding stepped increase in current through the CPW inductor results in a "kick-start" pulse over the output; a sharp onset of a coherent wavelet is thereby possible. These circuit dynamics were explored in measurements for $t_p = 25$-ps-short pulse-lengths in Paper VII. As the circuit presented lacks a constant DC-path to ground, the actual internal

bias provided from the stabilising capacitor will depend on the pulse pattern fed to the baseband input.

In this mmW wavelet generator circuit, the CPW stub inductor in part determines the carrier frequency, $f_c = 1/(2\pi\sqrt{C_{eff}L_{tnk}})$, of the wavelet generated and can be modelled using a quasi-transverse electromagnetic (TEM) approach [74]. This model predicts a non-shunted $L_{tn} = 8.3$-pH series inductance and a parallel $L_{tk} = 58$-pH inductance of the tap, cf. Figure 3.6(a). It further suggests a $Q_{tnk} \approx 50$ un-loaded quality-factor of the tank inductor, corresponding to series losses associated with the inductances. To find the effective capacitance of the RTD, the analytic modelling approach, suggested earlier and described in Appendix B, can provide an approximate answer. It is, however, greatly bias dependent and the effective value will depend on the time evolution of the wavelet generated, which in turn depends on the load used.

A measured wavelet generated for an $t_p = 80$-ps-short control pulse-length is shown in Figure 3.6(b), where the RTD used had a $A_{eff} = 21.5$-μm^2 active area and the circuit consumed 2 mA at $V_{Bias} = 1.2$ V. This wavelet has a $f_c = 64$-GHz carrier frequency and the de-embedded source power is $P_S = 2$ dBm. It is important to take the wideband power spectral density (PSD) into account when de-embedding such a signal, as discrete points in the transfer characteristics can be misleading. The modelled inductance and measured frequency determines a $C_{eff} = 110$-fF effective capacitance provided by the RTD in the tank, or 5.1-fF/μm^2 when normalised by the active area. Observe that although the load is not optimum the de-embedded measured power level is similar to, even exceeds, that predicted at optimum by the third-order source approximation.

In the limit case of slow wavelet envelope variations, the start-up and quench dynamics of the equivalent NDC oscillator can be studied analytically based on a van der Pol oscillator [75, 76]. This is, however, not the desired output. To investigate the potential of the wavelet generator core, the physical RTD model, specified in Appendix B, and the MOSFET switch approximation were implemented in a circuit simulator, as described in Appendix C. A simulated wavelet is presented in Figure 3.6(b), using a $V_{Bias} = 1.0$-V bias voltage that approximately represents the realised intrinsic bias of the measured circuit. The frequency and amplitude is similar to that of the measured wavelet, but the spectral content available from the simulation is more rich as the filtering effect of the 100-GHz sampling-head is missing. Numerical filtering of the simulated transients can be used to estimate the influence, as shown in Figure 3.6(b); a minimum-phase 120-GHz low-pass filter with 20-GHz cosine-tapering at the upper limit was used [13, 26]. This simulated and band-limited wavelet transient should better resemble that possible to capture in the sampling-oscilloscope. The similarity to the de-

embedded measured wavelet is striking; this suggests that the model used for the MOSFET is sufficient to capture the principal behaviour of the mmW wavelet generator. Simulations, using physical device models, promise a powerful tool in the design and optimisation of future RTD-based circuit implementations.

4

Compact Wavelet Transmitters

$\mathcal{E}$FFICIENT high-power signal generation is not enough to form a high performance wireless system, the remaining devices may degrade the link budget. The antenna is the next essential device in the signal path of the transmitter. Both the antenna itself and its interface to the generator should be optimised. If the antenna element is electrically small and efficient, both stand alone integration with small footprint and array implementations for beam forming and steering are attractive.

Through co-design of a compact antenna and the generator core technology described in the previous chapter, a versatile millimetre-wave (mmW) wavelet transmitter (WTx) module can be realised. One interesting concept is direct monolithic integration of the two devices, eliminating feed losses but also demanding a well defined inductive characteristic at the antenna port. To clarify, such an implementation avoids radio frequency (RF) signal routing on lossy transmission lines, but instead implies placement of the wavelet generator core at the antenna port, requiring fabrication accuracy. One solution, which is the one pursued, is to fabricate a monolithically-integrated antenna feed in the wavelet generator process technology.

4.1 ON-CHIP ANTENNAS

The size of an efficient antenna element aperture is typically comparable to half the free-space wavelength, $\lambda_0 = c_0/f_c$. At low frequencies, this would mean a very large aperture and one either has to settle with an inefficient or gargantuan implementation, or possibly both. However, an increase in carrier frequency results in a reduction of the free-space wavelength. As an example, the free-space wavelength at 60 GHz is only 5 mm, while 333 and 167 mm

are the corresponding values in the cellular 900 and 1800 MHz bands, respectively. This promises efficient antenna implementations for mmW systems on compact and portable devices such as cell phones, but may be compromised by increased material losses, user interaction, or shadowing effects [77]. The complementary view is that the directivity of an antenna aperture of fixed size increases with frequency, given an in-phase field distribution, and rather long-range links are thereby feasible even in the mmW spectrum.

Packaging of antenna will influence its design options and radiation characteristics. Electromagnetic waves interacting with matter shrink in accordance to the effective relative electric permittivity, $\varepsilon_{r,eff}$, and magnetic permeability, $\mu_{r,eff}$. The guided wavelength, λ_g, of a plane wave in matter is $\lambda_g = \lambda_0 / \sqrt{\varepsilon_{r,eff}\mu_{r,eff}}$. The exact effective values depend on the overlap of the wave fields and material regions of different characteristics. If an electromagnetic wave transits completely into a non-magnetic, $\mu_r = 1$, homogeneous material the effective parameters will simply become those of the material, i.e. $\mu_{r,eff} \to \mu_r = 1$ and $\varepsilon_{r,eff} \to \varepsilon_r$. Any material about an antenna will thereby reduce the effective signal wavelength, in effect increasing the electrical size of the antenna aperture. Various microstrip antenna types have been researched based on this principle, with the target of providing as compact an implementation as possible [78].

Scaling into the mmW spectrum provides further possibilities on system miniaturisation through packaging of RF front-end circuits and antennas in multi-chip modules (MCMs) on printed circuit boards (PCBs) and ceramics. To maintain a high efficiency, it is important to minimise the insertion loss between RF front-ends and antennas. Traditionally, wire-bonding can be utilised to transfer the signal to an antenna carrier substrate, where a short transmission line provides the interface to the antenna [78–80]. Flip-chip assembly, i.e. tightly connecting the front-end output to the transmission line on the carrier, is a more ideal solution as it avoids the substantial inductive parasitics of thin wires [53,81].

To illustrate the influence of the antenna and feed transmission line on the shape of wavelets transmitted over a wireless link, a few examples are illustrated in Figure 4.1. These signals were transmitted over a $d_c = 0.3$ m wireless link by connecting one antenna to the probed wavelet generator output, via a bias-T, and received by an equivalent antenna connected to a sampling oscilloscope. Interestingly, the horn and leaky-lens antennas show distinctly different results, despite their wideband and approximately constant gain characteristics. The explanation is the phase distortion of the interfacing waveguides used with the $G_A = 20$-dBi Flann 25240 V-band pyramidal horn antennas, resulting in an approximately triangular envelope. By contrast, the in-house fabricated $G_A = 16$-dBi leaky-lens antennas have negligible phase distortion and preserve the signal shape, as shown in Paper I;
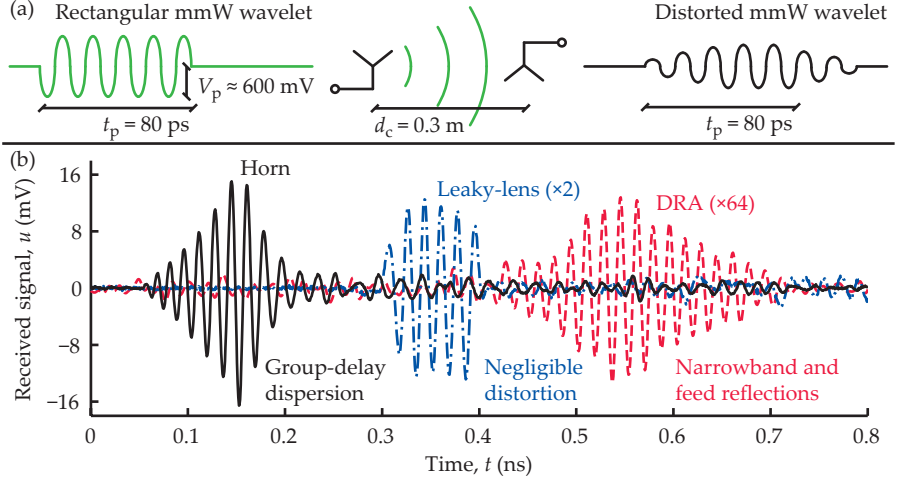
Figure 4.1: (a) Schematic illustration of link for transmission of $t_\mathrm{p} = 80$-ps rectangular-envelope $f_\mathrm{c} = 60$-GHz wavelets. (b) Received signals over a $d_\mathrm{c} = 0.3$-m symmetric link using horn, leaky-lens, or DRAs.

their bandwidth also lack the cut-off found in waveguide-based components. The third signal has been transmitted between narrowband $G_\mathrm{A} = 4$-dBi dielectric resonator antennas (DRAs) and their limited bandwidth smears the wavelet envelope, as compared to the horn and leaky-lens antennas. Taking a closer look on the DRA signal envelope, there is also a finer structure to be discerned. This stems from imperfect matching in the transition from the utilised connector and the feed transmission line on the carrier substrate used; significant round-trip propagation responses interact with the antenna port. For the purpose of signal fidelity, such reflections should be avoided.

Direct integration of the wavelet generator core and the antenna, i.e. fabricating an on-chip antenna, has the potential to eliminate many of the above imperfections. Consider the conceptual circuit schematics in Figure 4.2, showing the evolution from a more standard transmitter front-end to a monolithically-integrated WTx implementation. To deliver all generated power from the wavelet generator core to the antenna, the interfacing transmission line should be removed. This illustrates the most compact integration possible of a transmitter circuit, directly feeding the antenna port with a monolithic front-end. It further eliminates any transformation of the antenna admittance and thereby allows direct co-design to match the wavelet generator core. The bias stabilisation and inductive resonance circuit can thereby be mitigated into the antenna feed.

Circuit fabrication in compound semiconductor (III–V) technology often
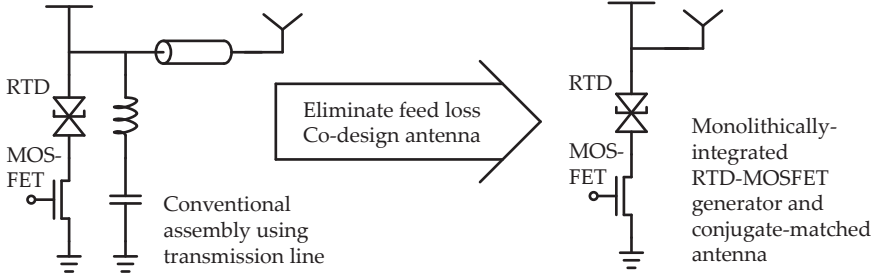
Figure 4.2: A monolithically-integrated WTx module allows for the insertion loss between generator and antenna to be eliminated, in effect providing a means for direct connection of a conjugate matched antenna load.

utilise a semi-insulating (SI) substrate with low loss. The 0.65-mm-thick indium phosphide (InP) wafer that carries the device heterostructures for the resonant-tunnelling diode (RTD) and metal-oxide-semiconductor field-effect transistor (MOSFET) presented in Chapter 3 provides a dielectric material of excellent quality. In the mmW spectrum, the relative permittivity is approximately $\varepsilon_{r,InP} = 12.6$, as the loss tangent is nominally $\mathrm{Im}\{\varepsilon_{r,InP}\} / \mathrm{Re}\{\varepsilon_{r,InP}\} = 3 \cdot 10^{-4}$, evaluated at 11 GHz [82]. Since the InP substrate used also has a specified resistivity of $\rho_d = 3 \cdot 10^5$ Ω–m, any substrate loss must be dominated by lattice dipole relaxation. In total, however, this means that the substrate loss will be negligible in an on-chip antenna implementation. By contrast, the radiation efficiency of the antenna will be limited by the resistivity of the feed metallisation. Skin-depth confinement of the radiating current magnifies any loss; the 0.5-μm-thick gold (Au) metallisation with $\rho_m = 24.4$-nΩ–m resistivity provides an approximate $\delta_s \approx 0.3$-μm skin-depth at $f = 60$ GHz.

If the monolithically-integrated concept is pursued, realisation of a mmW antenna with a single well-defined conjugate match to the RTD at the desired carrier frequency is a challenge. This stems from the fact that a chip large enough to carry an antenna typically is electrically large and can support various guided modes, in effect behaving like a high-order dielectric resonator (DR) [83]. Such high-order modes are challenging to predict in a packaged implementation and they typically interfere with the intended antenna input characteristics with a coupling strength which is proportional to the thickness of the substrate [84]. One attractive solution is to take advantage of such physics and allow for the fundamental mode in the chip to boost the antenna performance, i.e. designing a DRA. Interestingly, this option is typically neglected in review studies on options for integrated mmW antennas [85]; one explanation may be the inherently lossy silicon (Si) substrates traditionally

used. In effect, the work in this thesis is the first on monolithic integration of mmW wavelet generators with DRAs.

4.2 DIELECTRIC RESONATOR ANTENNAS

The support of standing wave resonances within the confinement of an open dielectric body was reported already in the late 1930's [83]. The idea of using such resonant modes for improving the radiative properties of small antennas was suggested three decades later [86]. Likely due to the otherwise unwieldy dimensions of low-frequency resonators, bodies with high relative electric permittivity, $\varepsilon_r \gg 10$, were initially of interest [87]. Radiative losses from the DR arise from non-perfect confinement of the mode fields, i.e. electric, $\vec{E}$, and magnetic, $\vec{H}$, leaking power into travelling waves. This implies that the Poynting vector, $\vec{S} = \vec{E} \times \vec{H}$, has a net non-zero component in the normal direction, $\hat{n}$, through the boundary of the dielectric body, $\oiint \hat{n} \cdot \vec{S} \, \partial A > 0$, where ∂A is an infinitesimal area on the boundary. Most modes in DRs of arbitrary shapes are typically of this non-confined type. Bodies with rotational symmetry can also support confined modes where both the normal electric field

$$\hat{n} \cdot \vec{E} = 0 \tag{4.1}$$

and the parallel magnetic field

$$\hat{n} \times \vec{H} = 0 \tag{4.2}$$

vanish on the faces of the DR; magnetic boundary conditions apply is such a case. Non-confined modes typically only obey (4.1) and can thereby radiate [88].

The fundamental mode of a simple dielectric body geometry typically provides a smooth, dipole-like radiation pattern. Operation at the fundamental resonance also provides the most compact antenna element, as compared to high-order modes. To predict the intrinsic resonance frequency, f_i, of a rectangular DR, such as that shown in Figure 4.3(a), the dielectric body can be modelled as an open-ended waveguide of length, d_z, in the z-direction [88–90]. This targets a transverse electric (TE) mode resonance about the z-axis. The fundamental transverse wavenumbers are thereby set by the width, a_x, and height, b_y, respectively, as

$$k_x = \frac{\pi}{a_x}, \tag{4.3}$$

and

$$k_y = \frac{\pi}{b_y}, \tag{4.4}$$

in the x- and y-directions. The longitudinal wavenumber in the z-direction, k_z, is given by a transcendental equation,

$$k_z \tan\left(k_z \frac{d_z}{2}\right) = \sqrt{(\varepsilon_r - 1)\, k_0{}^2 - k_z{}^2},$$ (4.5)

and is dependent on the free-space wavenumber, $k_0 = 2\pi f_i / c_0$, at the resonance frequency [89]. Provided a specified transverse size and dielectric material, i.e. electrical cross-section, the relation between the resonance frequency and longitudinal length can be solved by applying the separation equation

$$k_i{}^2 = \varepsilon_r k_0{}^2 = k_x{}^2 + k_y{}^2 + k_z{}^2,$$ (4.6)

where $k_i = 2\pi f_i \sqrt{\varepsilon_r} / c_0$ is the wavenumber in the material at the resonance frequency. The design conditions are slightly altered if the dielectric resonator is placed on a ground-plane, as illustrated in Figure 4.3(b). The actual dielectric body height in the y-dimension, h_y, is mirrored to an effective DR height, $b_y = 2h_y$, in such a configuration. Fixating a $d_z = 1$-mm length, the DR resonance frequency is plotted for various aspect ratios in height and width in Figure 4.3(c), assuming that an InP substrate such as that in the wavelet generator fabrication is used. A $a_x = d_z = 1$-mm quadratic-footprint is used here as it is predicted to have a $f_i = 60.4$-GHz intrinsic resonance if the $h_y = 0.65$-mm original thickness of the substrate is preserved. Full-wave calculations approximately reproduce this result, as noted in Appendix C.

In designing a DRA, a means to transfer energy into the dielectric body must be implemented, which can be facilitated by a coupling-structure. Rectangular DRAs have been shown possible to excite by means of, e.g. slot apertures [91] or coaxial, microstrip, and coplanar waveguide (CPW) transmission lines and stubs [92–94]. For implementation in a coplanar circuit technology, the CPW fed slot-coupled DRA is of special interest [95]. The coupling-slot is placed in a ground-plane in the x-z-plane, onto which the rectangular dielectric body is positioned, as illustrated in Figure 4.4(a). In this mirrored arrangement, the slot is effectively located in the centre of the dielectric body of the DRA. From this position, the electric field on the slot transmission line is closely overlapping that of the DR mode. This is the mechanism by which the coupling-slot can inject or drain energy to and from the radiating mode in the dielectric body.

In the geometries of the dielectric body and coupling-slot of the slot-coupled rectangular DRA, as well as their relative alignment, several trade-offs must be managed. The shape of the resonator can be used to modify the resonance, or even introduce more than one mode to widen the bandwidth [96, 97]. Further, the size of the slot determines the amount of perturbation which it performs on the intrinsic mode, or modes, of the
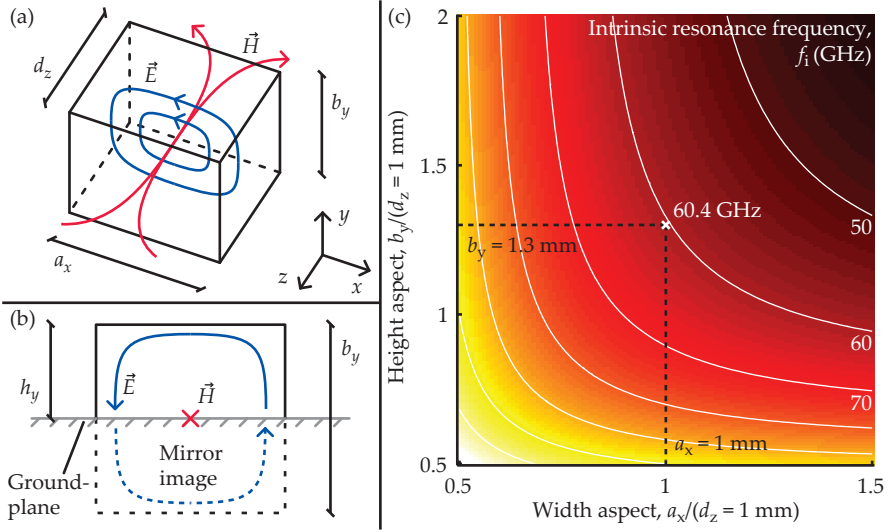
Figure 4.3: (a) Body of a rectangular DR with geometric definitions and a schematic drawing of the fundamental mode. (b) Mirrored body of a rectangular DR on a ground-plane. (c) Resonance frequency of an InP DR as a function of the width and height aspect in relation to the length according to the dielectric waveguide model.

dielectric body. If the coupling-slot occupies a significant area, the mode can extend slightly through the slot, thereby lowering the resonance frequency from that of the intrinsic mirrored DR. There must, however, exist a minimum resonance frequency because the case of a slot much larger than the dielectric body would not mirror the mode, producing a DR of half the size and an increased resonance frequency. Intuitively, starting from an infinitesimally small coupling-slot, coupling to the dielectric body of the DRA must be proportional to its length and width. There is also a design trade-off between any direct radiation, the coupling strength, and the resonance quality factor of the dielectric body of the DRA. More frankly, this can be expressed as a trade-off between the extremes of a non-radiating DR and an ordinary antenna.

Two similar but fundamentally different antenna concepts are considered for wavelet generator integration in this thesis. As outlined in the study summarised in Paper VIII, the first option is to design a conjugate-matched antenna that presents an input with both an inductive component, to resonate the RTD capacitance, as well as a radiation conductance. An electrically-short slot is inductive and is thereby a suitable candidate. This is illustrated Figure 4.4(a), together with the simulated antenna admittances, Y_A, in Figure 4.4(b). These simulated characteristics correspond to a $v_s = 20\text{-}\mu\text{m}$
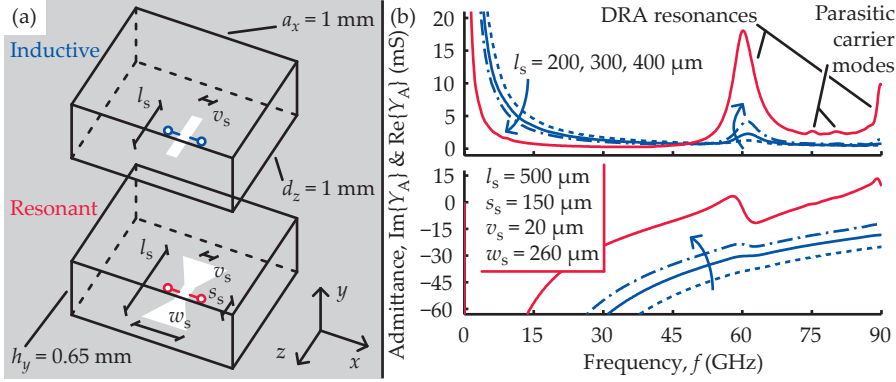
Figure 4.4: (a) Schematic illustrations of inductive and resonant coupling-slot design options for a slot-coupled DRA. (b) Input admittance of simulated designs suitable for $f_c = 60$-GHz carrier operation.

wide, centred and centre-fed, coupling slot that has a two-sided length l_s stepped from 200 through 400 μm. As expected, a generally inductive admittance that scales in inverse proportion to the length of the coupling-slot can be observed. This is overlapped by a resonant feature about the designed frequency, $f_i \approx 60$ GHz, adding a conductance peak and a minor undulation in the susceptance in effect from the radiation mechanism via the dielectric body. The strength of this radiation effect is seen to scale in proportion to the length of the coupling-slot. It is further seen that the resistive losses, most significant in the low-frequency region, are reduced for increased slot length. A more conventional resonant mmW DRA was explored in Paper IX, where an intrinsic smooth magnetic-dipole-like, but mirrored, $G_A = 6$-dBi-maximum-gain and 98%-efficiency radiation characteristic was predicted from simulations. In relation to WTx integration, this second design option is to keep the on-chip inductor separate from the antenna feed. This is more similar to the probed wavelet generator implementation, except that the output probe is replaced by the antenna port. A $w_s = 260$-μm-tapered coupling-slot is utilised for this purpose, also in Figure 4.4(a-b). Except for the modified $l_s = 500$-μm-length, only an $s_s = 150$-μm-short part of the centre-fed coupling slot retains the $v_s = 20$-μm un-tapered width. Studying the simulated characteristics of this resonant DRA, the greatly increased strength achieved in the radiation conductance comes with a substantial undulation in the inductive susceptance. Also visible is the onset of a high-order resonance in the DRA, as well as minor perturbations that correspond to coupling into modes in the carrier substrate. Details of the simulation procedures are discussed in Appendix C.
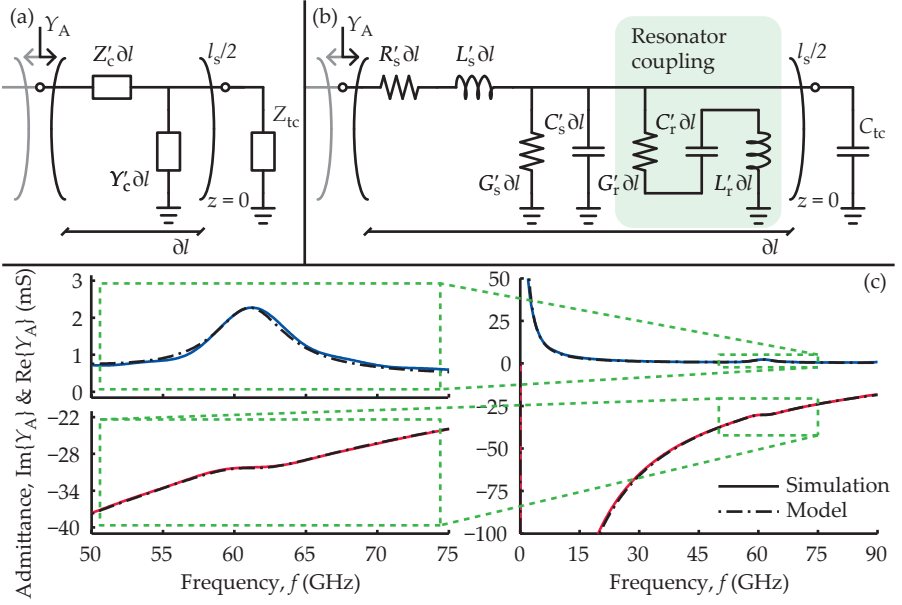
Figure 4.5: (a) Generic infinitesimal unit circuit model of a centre-fed coupling-slot with a terminating impedance, observe that only one side is shown. (b) Coupling to the dielectric body of the DRA can be described as a series resonance, and (c) the model fits simulated input admittance.

By identifying the coupling-slot as two transmission line sections that are connected in parallel and loaded by the DR, an analytic model can be derived. As illustrated in Figure 4.5(a), studying one side of the coupling-structure, the coupling-slot has an impedance and an admittance per unit length, Z'_c and Y'_c, respectively, and is simply a lossy transmission line, where $Z'_c \partial l$ and $Y'_c \partial l$ denote infinitesimal transmission line parameters over the infinitesimal length, ∂l. The terminating impedance at the end of the coupling-slot, Z_{tc}, is in the most simple case a short-circuit. This modelling method has been demonstrated for electrically-short centre-fed printed slot antennas [98], and further extended to correct for high-order resonances and arbitrary feed locations [99]. Instead of a short-circuit termination at the ends of the slot, which would be the case for a standard antenna, a $C_{tc} = 330$-pF capacitor can be implemented, as illustrated in Figure 4.5(b). This allows for a direct-current (DC) bias voltage over the antenna port, e.g. as demonstrated for monolithic slot antennas used in continuous-wave (CW) RTD transmitters [59]. In the un-tapered case this terminating capacitor, as illustrated in Figure 4.5(b), approximately provides an effective short-circuit at the carrier-frequency.

The infinitesimal unit circuit is expanded in Figure 4.5(b), in part containing standard parameters as R'_s, L'_s, G'_s, and C'_s denote the corresponding resistance, inductance, conductance, and capacitance parameters per unit length of the coupling-slot. To describe the coupling to the mode in the dielectric body of the DRA, a shunting series resonance is added. The radiation conductance per unit length, G'_r, arises due to the coupling to the non-confined mode; the corresponding inductance and capacitance, L'_r and C'_r, respectively, are set by the loaded resonance frequency, $f_r \approx f_i$, and the quality factor, Q_r, of the mode in the dielectric body of the DRA. The model provides a compact analytic expression for the antenna input characteristic via (1.11), and allows a good fit to the simulated admittance, Y_A, of the inductive DRA, as shown in Figure 4.5(c). It should be noted that constant parameters are used in the model. This requires the coupling-slot to be uniform and further that any coupling to the dielectric body is independent of the position along the slot line. The latter is approximately true for a short coupling-slot, however, it was not possible to find a perfect simultaneous fit to simulations of antennas with a significant length scaling of the coupling-slot. Although the parameters are constant over the length of the coupling-slot, the RF resistance of the slot metallisation is allowed to scale in inverse proportion to the skin-depth, i.e. $R'_s \propto 1/\delta_s$. Further, if the coupling-slot is a non-uniform transmission line, as for the resonant DRA design, numerical analysis will be required. The terminating impedance, Z_{tc}, can also be somewhat troublesome to identify for a significant width of the coupling-slot end. The DRA modelling is described further in Appendix B.

4.3 MONOLITHICALLY-INTEGRATED TRANSMITTERS

Monolithically-integrated WTxs can be implemented by realising wavelet generators at the ports of the presented DRA designs. The fabrication process is the same as that for the wavelet generator circuits, described briefly in Chapter 3 and further in Appendix A, although the design of the final circuit layers are changed.

In the core circuit for the WTx that has an inductive DRA, an RTD of suitable size to match its effective capacitance, C_{eff}, to the inductance of the coupling-slot must be used. The inductive $l_s = 300$-μm-long and $v_s = 20$-μm-wide coupling-slot design is used for this WTx implementation, reported in Paper X, and the RTD used has a $A_{eff} = 34.7$-μm^2 active area. A conceptual circuit is shown in Figure 4.6(a), and a micrograph of the fabricated chip is provided in Figure 4.6(b). As can be seen, the control signal for the wavelet generator is routed along a CPW in the electric plane of the DRA to minimise perturbation of the mode in the dielectric body below. Bias is fed to the
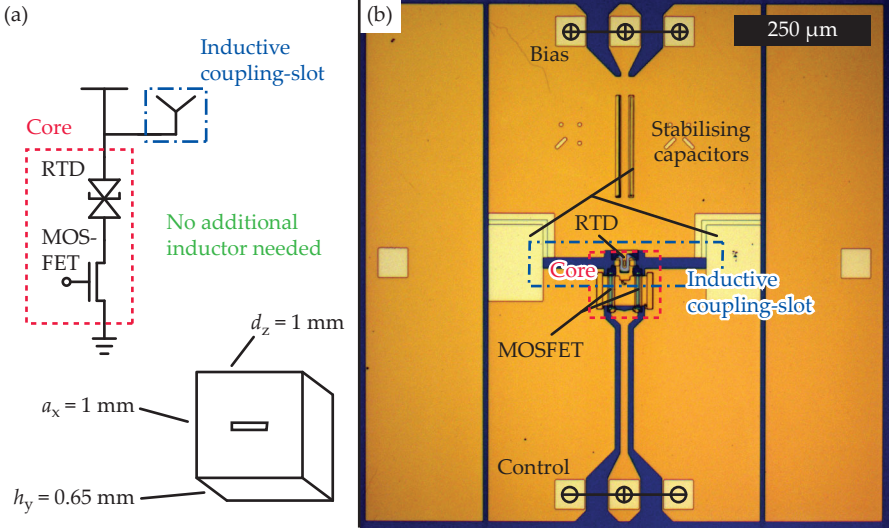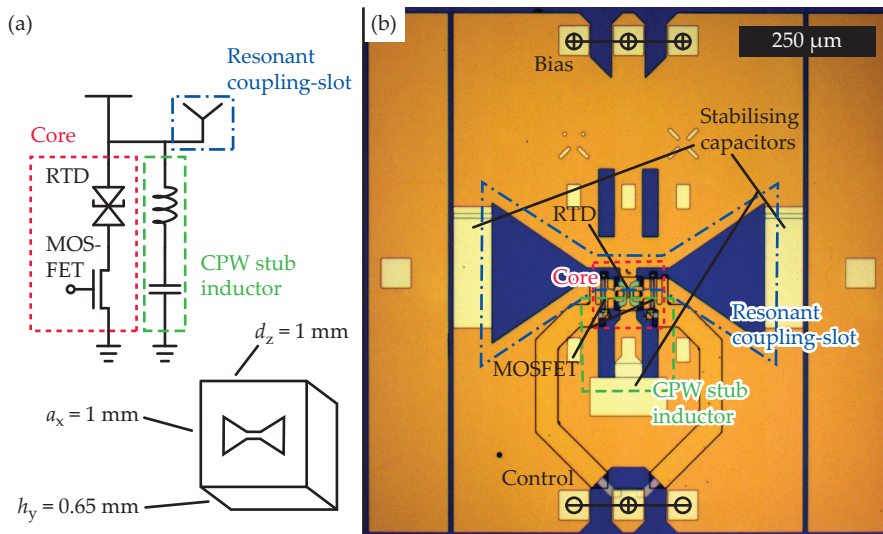
Figure 4.6: (a) Schematic circuit concept of the monolithically-integrated WTx with an inductive DRA, and (b) a chip micrograph of the fabricated circuit.

upper half of the antenna ground-plane. It is thereby provided to the RTD-MOSFET core directly in DC operation, but stored for pulsed RF operation in the stabilising slot-terminating capacitors. The side panels of the ground-plane are disconnected from the coupling-slot to avoid a galvanic short-circuit via the carrier ground-plane.

A more conventional WTx implementation that utilises the resonant DRA design must also feature a separate inductor, as illustrated schematically in Figure 4.7(a). Similar to that of the probed wavelet generator presented in Chapter 3, this 57-pH inductor is implemented as a CPW stub, visible on the chip micrograph in Figure 4.7(b). Compared to the WTx co-designed with a inductive DRA, this allows for a more relaxed design procedure where the input admittance of the resonant DRA and the 41.3-μm^2 active area of the RTD used can be selected independently. In the design shown in Figure 4.7(b), the coupling-slot occupies the region above the RTD, the inductor occupies that below, and the MOSFET gates cut off the remaining sides, the CPW input utilised for the control signal on the inductive DRA design is thereby not possible. Instead, microstrip lines separated from the ground-plane by the utilised interlayer dielectric were used.

After finalising the monolithic fabrication, the sample is diced by sawing to form the designed dielectric bodies of the DRAs. Compact WTx front-ends with monolithically-integrated on-chip antennas are thereby realised

Figure 4.7: (a) Schematic circuit concept of the monolithically-integrated WTx with a resonant DRA and separate CPW inductor, and (b) a chip micrograph of the fabricated circuit.

in a III–V die, as shown for size reference in Figure 4.8(a). Convenient operation of these WTxs require the active die faces shown in Figure 4.6(b) and Figure 4.7(b) to be flip-chip assembled onto carrier substrates that provide the control signal and bias voltage inputs. A 32-mil RO4003 carrier with 30-μm copper (Cu) metallisations capped with electroless nickel immersion gold (ENIG) were designed for this purpose. A schematic cross-section of the intended geometry is illustrated in Figure 4.8(b), also showing openings utilised below the WTx die. The flip-chip assembly is performed by solder-bonding the pads on carrier and die, utilising an indium (In)-based solder compound. Approximately 25-μm diameter solder-spheres were positioned by use of a bond wedge and pre-soldered by heating of the carrier on a hotplate. This realises the scene on the mid-process micrograph shown in Figure 4.8(c), also displaying the carrier feed interfaces and alignment markers used. Flip-chip alignment and subsequent soldering of the WTx die finalises the prototype assembly. Front and back views of the complete WTx prototype is shown in Figure 4.8(d). Here, SMA interfaces are utilised to end-launch the control signal and bias voltage onto the carrier. The contacts are located along the axis of the coupling-slot on the DRA, the respective radiation minima promising minimum interference. The input and bias signals are mainly routed on the back side but transit to the WTx on front by vias.

The radiated output signals from the fabricated and assembled
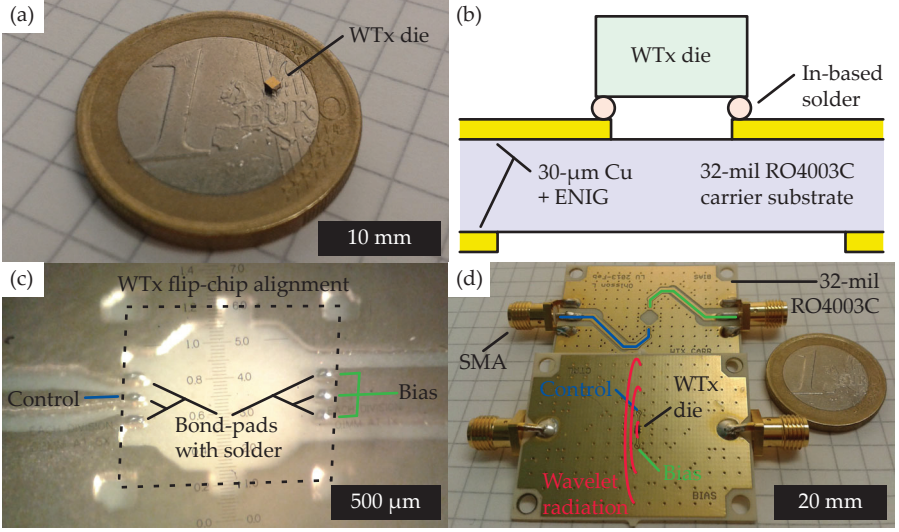
Figure 4.8: (a) A fabricated WTx die on a €1-coin, awaiting assembly on a carrier. (b) Schematic illustration of the solder-bonding assembly technique and (c) a mid-process photograph taken before the flip-chip die alignment and final solder step. (d) A finalised WTx prototype module, illustrating the control and bias inputs and mmW wavelet radiation output.

monolithically-integrated WTxs were evaluated in a transmission setup over a d_c = 0.15-m link, as illustrated schematically in Figure 4.9(a) and on the setup photograph in Figure 4.9(b). A G_A = 16-dBi leaky-wave lens antenna was utilised on the receiving side and connected directly to the 100-GHz sampling-head of an oscilloscope. The minimal distortion induced by this receiving antenna allows for the best possible view of the radiated waveforms from the WTx prototype modules.

Received mmW waveforms captured in the front- and back-side normal directions for an t_p = 80-ps control signal pulse-length are shown in Figure 4.9(c). A $f_c \approx 62.5$ GHz carrier frequency is observed from both WTx prototype designs, matching the V-band centre, and the peak equivalent isotropically radiated power is approximately 11 dBm. Combined with the simulated 6-dBi directivity of the DRA, this corresponds to a radiated power level of P_{Tx} = 5 dBm. The bias voltage was V_{Bias} = 1.45 V for the WTx with an inductive antenna, while V_{Bias} = 1.85 V was used for that with the resonant antenna. This bias difference was required to operate about the resonance of the DRA and maximise output signal, tuned by the bias- and load-dependent effective capacitance of the RTDs used. A numerical 75-GHz bandpass filter has been applied to reject noise and control signal leakage picked up by the
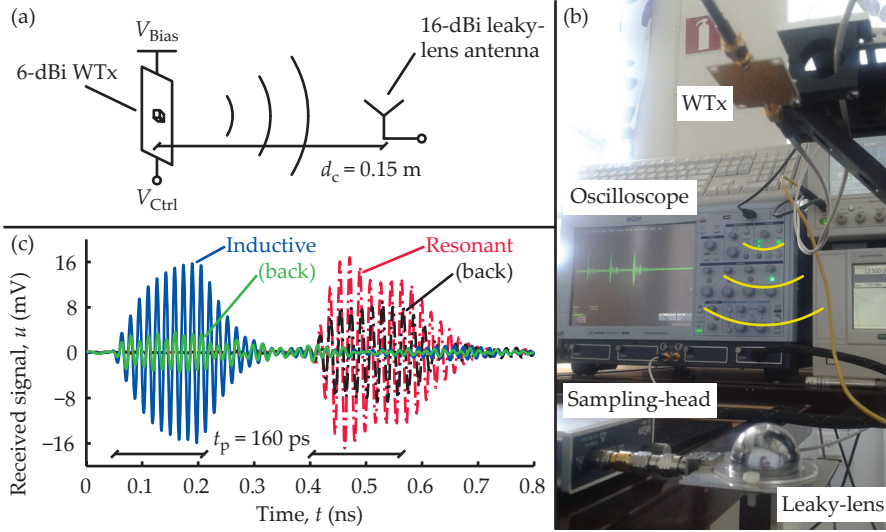
Figure 4.9: (a) Schematic setup for characterisation the monolithically-integrated WTx prototype modules, and (b) a setup photograph taken during measurement. (c) Wavelets received from the front and back broadside directions of the WTxs with inductive and resonant DRAs.

wideband leaky-lens antenna.

The wavelet signal envelope of the WTx with an inductive DRA rises and falls monotonically at the start-up and quench of the signal. By contrast, that of the WTx with a resonant antenna has an overshoot through the first carrier oscillation cycles at start-up. Comparing the back-side radiation to that of the front-side, the inductive design with a small coupling-slot has a significantly lower back-radiation level. Its back-envelope also appears roughly rectangular, but with added responses at some delay that can be explained as multiple reflections in the carrier substrate. The WTx with a resonant coupling-slot has a slightly more rounded back-envelope. This can be interpreted as if the wavelets generated over the coupling-slot ports of the antennas have approximately rectangular envelopes. It further suggests that the direct radiation effects from the coupling-slot, i.e. radiation that do not interact with the mode in the dielectric body, are relatively small for the inductive DRA design, but quite significant for the resonant design.

Focusing on the more ideal WTx with an inductive DRA, the radiated signal envelope resembles that from a first-order bandpass filter. An approximate equivalent $Q \approx 10$ quality factor can be identified, corresponding to a $B_S \approx$ 6-GHz signal bandwidth. These compact and efficient WTx circuits thereby promise performance in short-range and wideband applications.

5

Outlook

A compact and efficient circuit implementation for the generation and transmission of ultra-short millimetre-wave (mmW) wavelets was presented in this thesis. The compound semiconductor (III–V) wavelet generator core and its implementation in various resonance circuits with different loads addresses the challenge to generate and transmit short bursts of power in the mmW spectrum. In this final chapter, I will take the opportunity to suggest interesting projects which one could undertake to further explore the potential of integrated wavelet technology.

5.1 CONTROL AND RECEIVER CIRCUITS

During the work presented in this thesis, control signals and receiver circuits have been generated using general purpose measurement equipments and implemented via off-the-shelf circuits, respectively. To build a complete wireless system from the wavelet generator technology, digital interfaces must be implemented on both the transmitting and receiving sides. Indeed, an efficient receiver must also be realised. For compactness and signal fidelity, a packaged multi-chip module (MCM) should be the target for both transmitter and receiver.

A wavelet receiver can in principle be implemented by energy detection, followed by amplification and analogue-to-digital conversion. For scalability to high-order modulation and terahertz frequencies, continuous-wave (CW) or template mixing in phase-quadrature to an intermediate frequency can be included. Efficient mixers, amplifiers, and converters must be developed for this purpose. For maximum receiver sensitivity, the mixer or detector should be co-designed with the receiving antenna.

Returning to the transmitter, a parallel digital input must be converted to ultra-short control pulses for the wavelet generator input. Such digital arithmetic tasks are likely best handled by an application-specific integrated circuit (ASIC) implemented in complementary metal-oxide-semiconductor (CMOS) technology. This chip with control circuitry could be packaged in close vicinity to the wavelet transmitter (WTx) die, e.g. feeding the generator input through a via from the back of the carrier printed circuit board (PCB) to preserve a clean antenna environment on the front.

5.2 WAVELET TRANSMITTER ARRAY

One intuitive continuation of the monolithically-integrated WTx element is array implementations. Several WTx elements could be solder-bonded to the one side of a carrier PCB, and by adding control circuitry on the other, a WTx array with individual synchronised signal generation is possible. The compactness of the dielectric resonator antenna (DRA) allows for a densely populated array, which provides optimum beam control. This MCM could then be used for spatially multiplexing access points in piconets, or for portable radar systems.

In a similar fashion, a monolithically-integrated wavelet receiver (WRx) array can be constructed.

5.3 LEAKY-WAVELET TRANSCEIVER

If a rectangular-envelope mmW wavelet in a more directive beam is desired, a leaky-wavelet transceiver can be considered. Instead of fabricating a DRA about the wavelet generator core, forming the monolithically-integrated WTx, a leaky-wave lens antenna can be used. The core and an inductor would occupy a III–V die with logic input from a control ASIC. This can be then be flip-chip solder-bonded to a PCB carrier, feeding a leaky-wave coupling structure with the radio frequency (RF) output. In such an implementation, the leaky-lens antenna would act as a wideband radiating load of approximately constant impedance. The high antenna gain provides an improved link budget, as compared to a single DRA element.

As for the DRA implementation, a leaky-wavelet receiver can also be constructed by mounting the corresponding circuits on another leaky-lens antenna. To obtain a steerable beam from this leaky-wavelet transceiver, array feed structures can be considered [100].

Bibliography

[1] F. Boccardi, R. W. Heath, A. Lozano, T. L. Marzetta, and P. Popovski, "Five disruptive technology directions for 5G," *IEEE Commun. Mag.*, vol. 52, no. 2, pp. 74–80, Feb. 2014.

[2] P. Smulders, "The road to 100 Gb/s wireless and beyond: basic issues and key directions," *IEEE Commun. Mag.*, vol. 51, no. 12, pp. 86–91, Dec. 2013.

[3] C. Gustafson, K. Haneda, S. Wyne, and F. Tufvesson, "On mm-wave multipath clustering and channel modeling," *IEEE Trans. Antennas Propag.*, vol. 62, no. 3, pp. 1445–1455, Mar. 2014.

[4] H. T. Friis, "A note on a simple transmission formula," *Proc. IRE*, vol. 34, no. 5, pp. 254–256, May 1946.

[5] C. E. Shannon, "Communication in the presence of noise," *Proc. IRE*, vol. 37, no. 1, pp. 10–21, Jan. 1949.

[6] C. Özdemir, *Inverse Synthetic Aperture Radar Imaging With MATLAB Algorithms*, 1st ed.   Wiley, 2012.

[7] D. M. Pozar, *Microwave Engineering*, 4th ed.   Wiley, 2012.

[8] K. Kurokawa, "Power waves and the scattering matrix," *IEEE Trans. Microw. Theory Techn.*, vol. 13, no. 2, pp. 194–202, Mar. 1965.

[9] D. A. Frickey, "Conversions between S, Z, Y, H, ABCD, and T parameters which are valid for complex source and load impedances," *IEEE Trans. Microw. Theory Techn.*, vol. 42, no. 2, pp. 205–211, Feb. 1994.

[10] R. B. Marks, D. F. Williams, and D. A. Frickey, "Comments on "conversions between S, Z, Y, H, ABCD, and T parameters which are valid for complex source and load impedances" [with reply]," *IEEE Trans. Microw. Theory Techn.*, vol. 43, no. 4, pp. 914–915, Apr. 1995.

[11] D. Williams, "Traveling waves and power waves: Building a solid foundation for microwave circuit theory," *IEEE Microw. Mag.*, vol. 14, no. 7, pp. 38–45, Nov. 2013.

[12] A. V. Oppenheim and R. W. Schafer, *Discrete-Time Signal Processing*, 2nd ed. Prentice Hall, 1998.

[13] S.-C. Pei and H.-S. Lin, "Minimum-phase FIR filter design using real cepstrum," *IEEE Trans. Circuits Syst. II, Exp. Briefs*, vol. 53, no. 10, pp. 1113–1117, Oct. 2006.

[14] R. C. Daniels, J. N. Murdock, T. S. Rappaport, and R. W. Heath, "60 GHz wireless: Up close and personal," *IEEE Microw. Mag.*, vol. 11, no. 7, pp. 44–50, Dec. 2010.

[15] S. Rangan, T. S. Rappaport, and E. Erkip, "Millimeter-wave cellular wireless networks: Potentials and challenges," *Proc. IEEE*, vol. 102, no. 3, pp. 366–385, Mar. 2014.

[16] R. B. Marks, L. A. Hayden, J. A. Jargon, and F. Williams, "Time domain network analysis using the multiline TRL calibration," in *44th ARFTG Conf. Dig.-Fall*, vol. 26, Dec. 1994, pp. 47–55.

[17] A. Neto, "UWB, non dispersive radiation from the planarly fed leaky lens antenna–part 1: Theory and design," *IEEE Trans. Antennas Propag.*, vol. 58, no. 7, pp. 2238–2247, Jul. 2010.

[18] J. D. McKinney, D. Peroulis, and A. M. Weiner, "Time-domain measurement of the frequency-dependent delay of broadband antennas," *IEEE Trans. Antennas Propag.*, vol. 56, no. 1, pp. 39–47, Jan. 2008.

[19] W. Wiesbeck, G. Adamiuk, and C. Sturm, "Basic properties and design principles of UWB antennas," *Proc. IEEE*, vol. 97, no. 2, pp. 372–385, Feb. 2009.

[20] S. M. Riad, "The deconvolution problem: An overview," *Proc. IEEE*, vol. 74, no. 1, pp. 82–85, Jan. 1986.

[21] B. Parruck and S. M. Riad, "An optimization criterion for iterative deconvolution," *IEEE Trans. Instrum. Meas.*, vol. 32, no. 1, pp. 137–140, Mar. 1983.

[22] A. Bennia and S. M. Riad, "An optimization technique for iterative frequency-domain deconvolution," *IEEE Trans. Instrum. Meas.*, vol. 39, no. 2, pp. 358–362, Apr. 1990.

[23] B. Scheers, M. Acheroy, and A. van der Vorst, "Time-domain simulation and characterisation of TEM horns using a normalised impulse response," *IEE Proc. Microw. Antennas Propag.*, vol. 147, no. 6, pp. 463–468, Dec. 2000.

[24] K. Lu and T. J. Brazil, "A systematic error analysis of HP 8510 time-domain gating techniques with experimental verification," in *1993 IEEE MTT-S Int. Symp. Microwave Dig.*, vol. 3, Jun. 14-18, 1993, pp. 1259–1262.

[25] V. Bilik and J. Bezek, "Improved cable correction method in antenna installation measurements," *IET Electron. Lett.*, vol. 34, no. 17, pp. 1627–1628, Aug. 1998.

[26] F. J. Harris, "On the use of windows for harmonic analysis with the discrete fourier transform," *Proc. IEEE*, vol. 66, no. 1, pp. 51–83, Jan. 1978.

[27] R. B. Marks, "A multiline method of network analyzer calibration," *IEEE Trans. Microw. Theory Techn.*, vol. 39, no. 7, pp. 1205–1215, Jul. 1991.

[28] I. Vakili, L. Ohlsson, M. Gustafsson, and L.-E. Wernersson, "Time domain material characterizations using leaky lens antennas," in *31st URSI Symp. General Assembly and Scientific (URSI GASS 2014)*, Aug. 16-23, 2014, pp. 1–2.

[29] I. Vakili, L. Ohlsson, L.-E. Wernersson, and M. Gustafsson, "Complex permittivity extraction using a leaky-lens antenna system," in *2014 Symp. Progress in Electromagnetics Research (PIERS)*, Aug. 25-28, 2014, p. 1271.

[30] C. Park and T. S. Rappaport, "Short-range wireless communications for next-generation networks: UWB, 60 GHz millimeter-wave WPAN, and ZigBee," *IEEE Wireless Commun.*, vol. 14, no. 4, pp. 70–78, Aug. 2007.

[31] T. Baykas, C.-S. Sum, Z. Lan, J. Wang, M. A. Rahman, H. Harada, and S. Kato, "IEEE 802.15.3c: the first IEEE wireless standard for data rates over 1 Gb/s," *IEEE Commun. Mag.*, vol. 49, no. 7, pp. 114–121, Jul. 2011.

[32] H.-J. Song and T. Nagatsuma, "Present and future of terahertz communications," *IEEE Trans. THz Sci. Technol.*, vol. 1, no. 1, pp. 256–263, Sep. 2011.

[33] F. Rusek, D. Persson, B. K. Lau, E. G. Larsson, T. L. Marzetta, O. Edfors, and F. Tufvesson, "Scaling up MIMO: Opportunities and challenges with very large arrays," *IEEE Signal Process. Mag.*, vol. 30, no. 1, pp. 40–60, Jan. 2013.

[34] H. Bissessur, G. Charlet, W. Idler, C. Simonneau, S. Borne, L. Pierre, R. Dischler, C. de Barros, and P. Tran, "3.2 Tbit/s (80 × 40 Gbit/s) phase-shaped binary transmission over 3 × 100 km with 0.8 bit/s/Hz efficiency," *IET Electron. Lett.*, vol. 38, no. 8, pp. 377–379, Apr. 2002.

[35] I. Sarkas, S. T. Nicolson, A. Tomkins, E. Laskin, P. Chevalier, B. Sautreuil, and S. P. Voinigescu, "An 18-Gb/s, direct QPSK modulation SiGe BiCMOS transceiver for last mile links in the 70-80 GHz band," *IEEE J. Solid-State Circuits*, vol. 45, no. 10, pp. 1968–1980, Oct. 2010.

[36] A. Tomkins, R. A. Aroca, T. Yamamoto, S. T. Nicolson, Y. Doi, and S. P. Voinigescu, "A zero-IF 60 GHz 65 nm CMOS transceiver with direct BPSK modulation demonstrating up to 6 Gb/s data rates over a 2 m wireless link," *IEEE J. Solid-State Circuits*, vol. 44, no. 8, pp. 2085–2099, Aug. 2009.

[37] C. Marcu, D. Chowdhury, C. Thakkar, J.-D. Park, L.-K. Kong, M. Tabesh, Y. Wang, B. Afshar, A. Gupta, A. Arbabian, S. Gambini, R. Zamani, E. Alon, and A. M. Niknejad, "A 90 nm CMOS low-power 60 GHz transceiver with integrated baseband circuitry," *IEEE J. Solid-State Circuits*, vol. 44, no. 12, pp. 3434–3447, Dec. 2009.

[38] S. K. Reynolds, B. A. Floyd, U. R. Pfeiffer, T. Beukema, J. Grzyb, C. Haymes, B. Gaucher, and M. Soyuer, "A silicon 60-GHz receiver and transmitter chipset for broadband communications," *IEEE J. Solid-State Circuits*, vol. 41, no. 12, pp. 2820–2831, Dec. 2006.

[39] A. Siligaris, O. Richard, B. Martineau, C. Mounet, F. Chaix, R. Ferragut, C. Dehos, J. Lanteri, L. Dussopt, S. D. Yamamoto, R. Pilard, P. Busson, A. Cathelin, D. Belot, and P. Vincent, "A 65 nm CMOS fully integrated transceiver module for 60 GHz wireless HD applications," in *2011 IEEE Int. Conf. Solid-State Circuits (ISSCC) Tech. Dig.*, Feb.20-24, 2011, pp. 162–164.

[40] N. Su, R. Rajavel, P. Deelman, J. N. Schulman, and P. Fay, "Sb-heterostructure millimeter-wave detectors with reduced capacitance and noise equivalent power," *IEEE Electron Device Lett.*, vol. 29, no. 6, pp. 536–539, Jun. 2008.

[41] H.-J. Song, J.-Y. Kim, K. Ajito, M. Yaita, and N. Kukutsu, "Fully integrated ASK receiver MMIC for terahertz communications at 300 GHz," *IEEE Trans. THz Sci. Technol.*, vol. 3, no. 4, pp. 445–452, Jul. 2013.

[42] C. W. Byeon, C. H. Yoon, and C. S. Park, "A 67-mW 10.7-Gb/s 60-GHz OOK CMOS transceiver for short-range wireless communications," *IEEE Trans. Microw. Theory Techn.*, vol. 61, no. 9, pp. 3391–3401, Sep. 2013.

[43] F. Zhu, W. Hong, W.-F. Liang, J.-X. Chen, X. Jiang, P.-P. Yan, and K. Wu, "A low-power low-cost 45-GHz OOK transceiver system in 90-nm CMOS for multi-Gb/s transmission," *IEEE Trans. Microw. Theory Techn.*, vol. 62, no. 9, pp. 2105–2117, Sep. 2014.

[44] E. Juntunen, M. C.-H. Leung, F. Barale, A. Rachamadugu, D. A. Yeh, B. G. Perumana, P. Sen, D. Dawn, S. Sarkar, S. Pinel, and J. Laskar, "A 60-GHz 38-pJ/bit 3.5-Gb/s 90-nm CMOS OOK digital radio," *IEEE Trans. Microw. Theory Techn.*, vol. 58, no. 2, pp. 348–355, Feb. 2010.

[45] J. Lee, Y. Chen, and Y. Huang, "A low-power low-cost fully-integrated 60-GHz transceiver system with OOK modulation and on-board antenna assembly," *IEEE J. Solid-State Circuits*, vol. 45, no. 2, pp. 264–275, Feb. 2010.

[46] A. Siligaris, F. Chaix, M. Pelissier, V. Puyal, J. Zevallos, L. Dussopt, and P. Vincent, "A low power 60-GHz 2.2-Gbps UWB transceiver with integrated antennas for short range communications," in *2013 IEEE Int. Symp. Radio Frequency Integrated Circuits (RFIC)*, Jun.2-4, 2013, pp. 297–300.

[47] K. Kawasaki, Y. Akiyama, K. Komori, M. Uno, H. Takeuchi, T. Itagaki, Y. Hino, Y. Kawasaki, K. Ito, and A. Hajimiri, "A millimeter-wave intra-connect solution," *IEEE J. Solid-State Circuits*, vol. 45, no. 12, pp. 2655–2666, Dec. 2010.

[48] Y. Tanaka, Y. Hino, Y. Okada, T. Takeda, S. Ohashi, H. Yamagishi, K. Kawasaki, and A. Hajimiri, "A versatile multi-modality serial link," in *2012 IEEE Int. Conf. Solid-State Circuits (ISSCC) Tech. Dig.*, Feb. 19-23, 2012, pp. 332–334.

[49] K. Katayama, M. Motoyoshi, K. Takano, L. C. Y., and M. Fujishima, "209 mW 11 Gbps 130 GHz CMOS transceiver for indoor wireless communication," in *2013 IEEE Asian Conf. Solid State Circuits (A-SSCC)*, Nov. 11-13, 2013, pp. 409–412.

[50] M. Fujishima, M. Motoyoshi, K. Katayama, K. Takano, N. Ono, and R. Fujimoto, "98 mW 10 Gbps wireless transceiver chipset with D-band CMOS circuits," *IEEE J. Solid-State Circuits*, vol. 48, no. 10, pp. 2273–2284, Oct. 2013.

[51] K. Okada, N. Li, K. Matsushita, K. Bunsen, R. Murakami, A. Musa, T. Sato, H. Asada, N. Takayama, S. Ito, W. Chaivipas, R. Minami, T. Yamaguchi, Y. Takeuchi, H. Yamagishi, M. Noda, and A. Matsuzawa, "A 60-GHz 16QAM/8PSK/QPSK/BPSK direct-conversion transceiver for IEEE802.15.3c," *IEEE J. Solid-State Circuits*, vol. 46, no. 12, pp. 2988–3004, Dec. 2011.

[52] H. Asada, K. Bunsen, K. Matsushita, R. Murakami, Q. Bu, A. Musa, T. Sato, T. Yamaguchi, R. Minami, T. Ito, K. Okada, and A. Matsuzawa, "A 60 GHz 16 Gb/s 16QAM low-power direct-conversion transceiver using capacitive cross-coupling neutralization in 65 nm CMOS," in *2011 IEEE Asian Conf. Solid State Circuits (A-SSCC)*, Nov. 14-16, 2011, pp. 373–376.

[53] T. S. Rappaport, J. N. Murdock, and F. Gutierrez, "State of the art in 60-GHz integrated circuits and systems for wireless communications," *Proc. IEEE*, vol. 99, no. 8, pp. 1390–1436, Aug. 2011.

[54] L. Esaki, "New phenomenon in narrow germanium p-n junctions," *APS Phys. Rev.*, vol. 109, no. 2, pp. 603–604, Jan. 1958.

[55] J. B. Gunn, "Microwave oscillations of current in III-V semiconductors," *Elsevier Solid State Commun.*, vol. 1, no. 4, pp. 88–91, Sep. 1963.

[56] L. L. Chang, L. Esaki, and R. Tsu, "Resonant tunneling in semiconductor double barriers," *AIP Appl. Phys. Lett.*, vol. 24, no. 12, pp. 593–595, Jun. 1974.

[57] E. R. Brown, W. D. Goodhue, and T. C. L. G. Sollner, "Fundamental oscillations up to 200 GHz in resonant tunneling diodes and new estimates of their maximum oscillation frequency from stationary-state tunneling theory," *AIP J. Appl. Phys.*, vol. 64, no. 3, pp. 1519–1529, Aug. 1988.

[58] J. H. Smet, T. P. E. Broekaert, and C. G. Fonstad, "Peak-to-valley current ratios as high as 50:1 at room temperature in pseudomorphic $In_{0.53}Ga_{0.47}As/AlAs/InAs$ resonant tunneling diodes," *AIP J. Appl. Phys.*, vol. 71, no. 5, pp. 2475–2477, Mar. 1992.

[59] H. Kanaya, H. Shibayama, S. Suzuki, and M. Asada, "Fundamental oscillation up to 1.31 THz in thin-well resonant tunneling diodes," in *24th IEEE Int. Conf. Indium Phosphide and Related Materials (IPRM 2012)*, Aug. 27-30, 2012, pp. 106–109.

[60] T. P. E. Broekaert, B. Brar, J. P. A. van der Wagt, A. C. Seabaugh, F. J. Morris, T. S. Moise, E. A. Beam, and G. A. Frazier, "A monolithic 4-bit 2-Gsps resonant tunneling analog-to-digital converter," *IEEE J. Solid-State Circuits*, vol. 33, no. 9, pp. 1342–1349, Sep. 1998.

[61] Q. Liu, A. Seabaugh, P. Chahal, and F. J. Morris, "Unified AC model for the resonant tunneling diode," *IEEE Trans. Electron Devices*, vol. 51, no. 5, pp. 653–657, May 2004.

[62] W. F. Chow, *Principles of Tunnel Diode Circuits*, 1st ed. Wiley, 1964.

[63] Y. Nakasha, Y. Kawano, T. Suzuki, T. Ohki, T. Takahashi, K. Makiyama, T. Hirose, and N. Hara, "A W-band wavelet generator using 0.13-μm InP HEMTs for multi-gigabit communications based on ultra-wideband impulse radio," in *2008 IEEE MTT-S Int. Symp. Microwave Dig.*, Jun. 15-20, 2008, pp. 109–112.

[64] N. Deparis, A. Siligaris, P. Vincent, and N. Rolland, "A 2 pJ/bit pulsed ILO UWB transmitter at 60 GHz in 65-nm CMOS-SOI," in *2009 IEEE Int. Conf. Ultra-Wideband (ICUWB)*, Sep. 9-11, 2009, pp. 113–117.

[65] A. Siligaris, N. Deparis, R. Pilard, D. Gloria, C. Loyez, N. Rolland, L. Dussopt, J. Lanteri, R. Beck, and P. Vincent, "A 60 ghz UWB impulse radio transmitter with integrated antenna in CMOS65nm SOI technology," in *11th IEEE Topical Meeting Silicon Monolithic Integrated Circuits in RF Systems (SiRF 2011)*, Jan. 17-19, 2011, pp. 153–156.

[66] A. Arbabian, S. Callender, S. Kang, B. Afshar, J.-C. Chien, and A. M. Niknejad, "A 90 GHz hybrid switching pulsed-transmitter for medical imaging," *IEEE J. Solid-State Circuits*, vol. 45, no. 12, pp. 2667–2681, Dec. 2010.

[67] D. H. Chow, M. Hafizi, W. E. Stanchina, J. A. Roth, J. J. Zinck, J. J. Dubray, and H. L. Dunlap, "Monolithic integration of resonant tunneling diodes and heterojunction bipolar transistors on patterned InâŮŃ substrates," *AVS J. Vac. Sci. Technol. B*, vol. 16, no. 3, pp. 1413–1416, May 1998.

[68] H. J. de los Santos, K. K. Chui, D. H. Chow, and H. L. Dunlap, "An efficient HBT/RTD oscillator for wireless applications," *IEEE Microw. Wireless Compon. Lett.*, vol. 11, no. 5, pp. 193–195, May 2001.

[69] L.-E. Wernersson, K. Georgsson, A. Litwin, L. Samuelson, and W. Seifert, "Planarization of epitaxial GaAs overgrowth over tungsten wires," *AIP J. Appl. Phys.*, vol. 79, no. 1, pp. 500–503, Jan. 1996.

[70] E. Lind, P. Lindstrom, and L.-E. Wernersson, "Resonant tunneling permeable base transistors with high transconductance," *IEEE Electron Device Lett.*, vol. 25, no. 10, pp. 678–680, Oct. 2004.

[71] M. Ärlelid, M. Egard, E. Lind, and L.-E. Wernersson, "Coherent V-band pulse generator for impulse radio BPSK," *IEEE Microw. Wireless Compon. Lett.*, vol. 20, no. 7, pp. 414–416, Jul. 2010.

[72] H. Riel, L.-E. Wernersson, M. Hong, and J. A. del Alamo, "III-V compound semiconductor transistors - from planar to nanowire," *MRS Bull.*, vol. 39, no. 8, pp. 668–677, Aug. 2014.

[73] M. Egard, M. Ärlelid, E. Lind, and L.-E. Wernersson, "Bias stabilization of negative differential conductance oscillators operated in pulsed mode," *IEEE Trans. Microw. Theory Techn.*, vol. 59, no. 3, pp. 672–677, Mar. 2011.

[74] W. Heinrich, "Quasi-TEM description of MMIC coplanar lines including conductor-loss effects," *IEEE Trans. Microw. Theory Techn*, vol. 41, no. 1, pp. 45–52, Jan. 1993.

[75] B. van der Pol, "The nonlinear theory of electric oscillations," *Proc. IRE*, vol. 22, no. 9, pp. 1051–1086, Sep. 1934.

[76] M. Egard, M. Ärlelid, E. Lind, G. Astromskas, and L.-E. Wernersson, "20 GHz wavelet generator using a gated tunnel diode," *IEEE Microw. Wireless Compon. Lett.*, vol. 19, no. 6, pp. 386–388, Jun. 2009.

[77] C. Gustafson and F. Tufvesson, "Characterization of 60 GHz shadowing by human bodies and simple phantoms," in *6th European Conf. Antennas and Propagation (EuCAP 2012)*, Mar. 26-30, 2012, pp. 473–477.

[78] R. A. Alhalabi and G. M. Rebeiz, "Design of high-efficiency millimeter-wave microstrip antennas for silicon RFIC applications," in *2011 IEEE Int. Symp. Antennas and Propagation (APS URSI)*, Jul. 3-8, 2011, pp. 2055–2058.

[79] A. Babakhani, X. Guan, A. Komijani, A. Natarajan, and A. Hajimiri, "A 77-GHz phased-array transceiver with on-chip antennas in silicon: Receiver and antennas," *IEEE J. Solid-State Circuits*, vol. 41, no. 12, pp. 2795–2806, Dec. 2006.

[80] J. P. Guzman, C. Calvez, R. Pilard, F. Gianesello, M. Ney, D. Gloria, and C. Person, "Silicon integrated dielectric resonator antenna solution for 60 GHz front-end modules," in *12th IEEE Topical Meeting Silicon Monolithic Integrated Circuits in RF Systems (SiRF 2012)*, Jan. 16-18, 2012, pp. 53–56.

[81] T. Zwick, D. Liu, and B. P. Gaucher, "Broadband planar superstrate antenna for integrated millimeterwave transceivers," *IEEE Trans. Antennas Propag.*, vol. 54, no. 10, pp. 2790–2796, Oct. 2006.

[82] J. Krupka, J. G. Hartnett, and M. Piersa, "Permittivity and microwave absorption of semi-insulating InP at microwave frequencies," *AIP Appl. Phys. Lett.*, vol. 98, no. 11, pp. 112 112–112 112–3, Mar. 2011.

[83] R. D. Richtmyer, "Dielectric resonators," *AIP J. Appl. Phys.*, vol. 10, no. 6, pp. 391–398, Jun. 1939.

[84] D. M. Pozar, "Considerations for millimeter wave printed antennas," *IEEE Trans. Antennas Propag.*, vol. 31, no. 5, pp. 740–747, Sep. 1983.

[85] G. M. Rebeiz, "Millimeter-wave and terahertz integrated circuit antennas," *Proc. IEEE*, vol. 80, no. 11, pp. 1748–1770, Nov. 1992.

[86] O. Sager and F. Tisi, "On eigenmodes and forced resonance-modes of dielectric spheres," *Proc. IEEE*, vol. 56, no. 9, pp. 1593–1594, Sep. 1968.

[87] J. van Bladel, "On the resonances of a dielectric resonator of very high permittivity," *IEEE Trans. Microw Theory Techn.*, vol. 23, no. 2, pp. 199–208, Feb. 1975.

[88] R. K. Mongia and A. Ittipiboon, "Theoretical and experimental investigations on rectangular dielectric resonator antennas," *IEEE Trans. Antennas Propag.*, vol. 45, no. 9, pp. 1348–1356, Sep. 1997.

[89] E. A. J. Marcatili, "Dielectric rectangular waveguide and directional coupler for integrated optics," *Bell System Techn. J.*, vol. 48, no. 7, pp. 2071–2102, Sep. 1969.

[90] R. K. Mongia, "Theoretical and experimental resonant frequencies of rectangular dielectric resonators," *IEE Proc. H Microwaves, Antennas and Propagation*, vol. 139, no. 1, pp. 98–104, Feb. 1992.

[91] J. T. H. St. Martin, Y. M. M. Antar, A. A. Kishk, A. Ittipiboon, and M. Cuhaci, "Dielectric resonator antenna using aperture coupling," *IET Electron. Lett.*, vol. 26, no. 24, pp. 2015–2016, Nov. 1990.

[92] M. W. McAllister, S. A. Long, and G. L. Conway, "Rectangular dielectric resonator antenna," *IET Electron. Lett.*, vol. 19, no. 6, pp. 218–219, Mar. 1983.

[93] R. A. Kranenburg and S. A. Long, "Microstrip transmission line excitation of dielectric resonator antennas," *IET Electron. Lett.*, vol. 24, no. 18, pp. 1156–1157, Sep. 1988.

[94] R. A. Kranenburg, S. A. Long, and J. T. Williams, "Coplanar waveguide excitation of dielectric resonator antennas," *IEEE Trans. Antennas Propag.*, vol. 39, no. 1, pp. 119–122, Jan. 1991.

[95] M. S. Al Salameh, Y. M. M. Antar, and G. Seguin, "Coplanar-waveguide-fed slot-coupled rectangular dielectric resonator antenna," *IEEE Trans. Antennas Propag.*, vol. 50, no. 10, pp. 1415–1419, Oct. 2002.

[96] Y. Ge, K. P. Esselle, and T. S. Bird, "Compact dielectric resonator antennas with ultrawide 60%–100% bandwidth," *IEEE Trans. Antennas Propag.*, vol. 59, no. 9, pp. 3445–3448, Sep. 2011.

[97] K. S. Ryu and A. A. Kishk, "Ultrawideband dielectric resonator antenna with broadside patterns mounted on a vertical ground plane edge," *IEEE Trans. Antennas Propag.*, vol. 58, no. 4, pp. 1047–1053, Apr. 2010.

[98] M. Himdi and J. P. Daniel, "Analysis of printed linear slot antenna using lossy transmission line model," *IET Electron. Lett.*, vol. 28, no. 6, pp. 598–601, Mar. 1992.

[99] J. E. Ruyle and J. T. Bernhard, "A wideband transmission line model for a slot antenna," *IEEE Trans. Antennas Propag.*, vol. 61, no. 3, pp. 1407–1410, Mar. 2013.

[100] A. V. Räisänen, J. Ala-Laurinaho, D. Chicherin, Z. Du, A. Generalov, A. Karttunen, D. Lioubtchenko, J. Mallat, A. Tamminen, and T. Zvolensky, "Antennas for electronic beam steering and focusing at millimeter wavelengths," in *2012 IEEE Int. Conf. Electromagnetics in Advanced Applications (ICEAA)*, Sep. 2012, pp. 1235–1237.

[101] R. Tsu and L. Esaki, "Tunneling in a finite superlattice," *AIP Appl. Phys. Lett.*, vol. 22, no. 11, pp. 562–564, Jun. 1973.

[102] J. N. Schulman, H. J. De Los Santos, and D. H. Chow, "Physics-based RTD current-voltage equation," *IEEE Electron Device Lett.*, vol. 17, no. 5, pp. 220–222, May 1996.

[103] E. B. Rosa, "The self and mutual inductances of linear conductors," *NBS Bull.*, vol. 4, no. 2, pp. 301–344, Jan. 1908.

[104] W. Heinrich, "The slot line in uniplanar MMIC's: propagation charac-
teristics and loss analysis," in *1990 IEEE MTT-S Int. Symp. Microwave
Dig.*, vol. 1, May 8-10, 1990, pp. 167–170.

APPENDICES

"It is nice to know that the computer understands the problem. But I would like to understand it too."

—Eugene Wigner

A

Device Fabrication

*N*ano-scale fabrication techniques are required to realise compound semi-conductor (III–V) devices for implementation in the millimetre-wave (mmW) spectrum. Below, a brief description of thin-film material growth and processing technology is provided; a standard batch recipe is then disclosed.

A.1 THIN-FILM TECHNOLOGY

Semiconductors used in device technologies are preferably mono-crystals with no or controlled impurities. First, a Czochralski process is typically used to draw a solidified ingot from a melt of the desired semiconductor compounds, which can then be sliced into wafers. If a nano-scale heterostructure of various III–V materials is desired on the surface of the wafer, this can be produced by molecular beam epitaxy (MBE). This process is performed in a vacuum chamber, in principle spraying the desired atoms onto the wafer, enabling atomic mono-layer control. Another option for layer growth is metal-organic vapour-phase epitaxy (MOVPE), where metal-organic and hydride precursors are flowed over the sample at an elevated temperature. These may decompose and the group III and V atoms can adhere to the sample at atomic layer steps on the surface to achieve step-flow crystal growth.

Having obtained a piece of a high-quality semiconductor wafer as a starting material, i.e. a chip, the envisioned device design must be realised. In a sequence of processing steps, lithographic techniques in combination with selective deposition or removal of material are used to define the device geometries. First, a resist is typically spun, and solidified into a thin film on the surface of the chip by baking. Parts of this resist layer can then be

exposed in ultra-violet (UV) light or electron beam lithography (EBL), and removed locally through immersion in a developer liquid.

A number of options are now available for local manipulation of the sample through the openings in the resist layer. For example, metal can be deposited in a blanket on the chip surface by evaporation. By dissolving the resist layer, lift-off of the material which landed on it can be achieved, leaving patterned structures on the sample surface. Another example is removal of semiconductor material where the openings in the resist will allow an acid or alkaline solution to etch the chip locally. Once again the process is finalised by dissolving the resist, leaving the chip in an altered state. These or other steps can then be repeated with different lithographic resist masks, stepwise building the devices and circuits.

A.2 WAVELET GENERATOR RECIPE

The designed wavelet generator circuit required a resonant-tunnelling diode (RTD) to be integrated monolithically with a metal-oxide-semiconductor field-effect transistor (MOSFET), and resonance circuits or antennas. A novel processing scheme was invented for this purpose, its early version is described in Paper VI and an updated description is given here.

The starting material in the fabrication process is an, externally produced, semi-insulating (SI) indium phosphide (InP) wafer grown with custom MBE layers designed according to Table A.1. This can support lattice-matched compositions of indium–aluminium–arsenide (In–Al–As) and indium–gallium–arsenide (In–Ga–As). The wafer features a pseudomorphic $In_{0.53}Ga_{0.47}As$/aluminium arsenide (AlAs)/indium arsenide (InAs) RTD on the top. Below, an $In_{0.53}Ga_{0.47}As$ MOSFET channel resides on a back-barrier of $In_{0.52}Al_{0.48}As$, which is delta-doped and provides a growth buffer to the substrate wafer. To provide etch control, stop layers of InP separate various sections of the III–V heterostructure.

The following recipe represents a standard process for the fabrication of a chip with RTDs, MOSFETs, wavelet generators, wavelet transmitters (WTxs), and various reference structures. Minor tweaking of the process parameters is always required as machine setting can drift and the chemicals may age between batches. The exact procedures and tool settings correspond to such applicable for equipment in Lund Nano Lab at the time of invention.

PREPARATION

The externally produced wafer is not processed in full, but cut into pieces.

Step 0: Cut Sample

- Cut a 8×10-mm^2 chip from the MBE wafer.

MESA ETCH

The RTD heterostructure resides on top of the MOSFET channel layer and must thereby be etched over most of the sample to allow parallel processing. By use of a mixture of phosphoric acid (H$_3$PO$_4$), hydrogen peroxide (H$_2$O$_2$), and de-ionised water (DIW), the In–Ga–As and In–Al–As layers can be removed selectively to the InP etch stop layers. To etch the InP, a mixture of hydrochloric acid (HCl) and H$_3$PO$_4$ can be utilised.

Step 1: Organic Clean

- 3 min in acetone, on 75°C hotplate
- 1 min beaker in ultra-sonic bath, setting 5
- 3 min in acetone, on 75°C hotplate
- 1 min in iso-propyl alcohol (IPA), on 75°C hotplate

Step 2: Dehydrate Sample

- 15 min on 200°C hotplate

Step 3: Apply ma-N 2403

- 45-s spin at 4500 rpm (1500 rpm/s)
- 2 min on 100°C hotplate

Step 4: Deep UV Lithography (240-nm line at 8.6 mW/cm^2)

- 10-s exposure

Step 5: Development

- 4 min in MF319
- 1 min in MF319, stir
- 1 min in DIW

Step 6: Plasma Ashing

- 60 s at 5-mbar oxygen (O)$_2$-pressure

Step 7: Temper Resist Mask

- 10 min on 140°C hotplate

Step 8: Wet Etching (layers 20→6)

- 150 s in H_3PO_4–H_2O_2–DIW (4:4:100), stir
- 30 s in DIW, stir
- 15 s in HCl–H_3PO_4 (2:8), stir
- 60 s in DIW, stir
- 50 s in H_3PO_4–H_2O_2–DIW (4:4:100), stir
- 60 s in DIW, stir

Step 9: Strip Resist

- 2 min in acetone, beaker in ultra-sonic bath, setting 4
- 1 min in IPA

DUMMY GATE

A short hydrogen silsesquioxane (HSQ) dummy gate will then be defined on the MOSFET channel layer.

Step 10: Ozone Cleaning

- 10 min at 500-sccm O_2-flow

Step 11: Wet Etching (layer 5 and oxide)

- 10 s in ammonium hydroxide (NH_4OH), stir
- 30 s in DIW, stir
- 10 s in HCl–H_3PO_4 (2:8), stir
- 60 s in DIW, stir
- 30 s in NH_4OH, stir
- 60 s in DIW, stir

Step 12: Dehydrate Sample

- 15 min on 200°C hotplate

Step 13: Apply HSQ XR-1541-006

- 45-s spin at 4500 rpm (1500 rpm/s)
- 2-min bake on 200°C hotplate

Step 14: Electron Beam Lithography (30 kV)

- 700-μC/cm^2 base dose, 2-nm raster

Step 15: Development

- 1 min in tetra-methyl ammonium hydroxide (TMAH)

- 1 min in TMAH, gently stir

- 1 min in DIW, gently stir

- 1 min in DIW, gently stir

CONTACT REGROWTH

A highly doped In–Ga–As contact layer is then grown about the dummy gate, and on top of the previously defines RTD mesa. The contact layer is further capped with an InP support layer.

Step 16: Ozone Cleaning

- 10 min at 500-sccm O_2-flow

Step 17: Wet Etching (pre-treatment)

- 30 s in NH_4OH

- 60 s in DIW

Step 18: MOVPE Regrowth

- 30 nm highly doped In–Ga–As contact layer

- 100 nm InP support layer

GATE FORMATION

The dummy gate is removed and, by means of atomic layer deposition (ALD), a aluminium (Al)- and hafnium (Hf)-based high-permittivity gate dielectric is deposited. This is followed by a deposition of a T-gate that attains its shape from the support layer. The excess dielectric material and the support layer are then removed.

Step 19: Organic Cleaning

- 3 min in acetone, on 75°C hotplate

- 1 min beaker in ultra-sonic bath, setting 4

- 1 min in IPA, on 75°C hotplate

Step 20: Wet Etching (dummy gate)

- 3 min in buffered oxide etch (BOE) (10:1)

- 60 s in DIW

Step 21: Ozone Cleaning

- 10 min at 500-sccm O_2-flow

Step 22: Passivation

- 20 min in 25% ammonium sulphide $((NH_4)_2S)$–DIW (1:2)
- 15 s in DIW

Step 23: ALD

- 20-sccm nitrogen $(N)_2$-flow
- 300°C
- 5× {0.015-s TMAl, pump 4 s}
- 5× {0.015-s TMAl, pump 4 s, 0.015-s water (H_2O) , pump 4 s}
- 100°C
- 50× {0.15-s TDMAHf, pump 60 s, 0.015-s H_2O, pump 60 s}

Step 24: Apply poly methyl-methacrylate (PMMA) 950 A6

- Two layers
- 45-s spin at 4500 rpm (1500 rpm/s)
- 2-bake on 180°C hotplate

Step 25: EBL Exposure (20 kV)

- 250-μC/cm^2 base dose, 6-nm raster

Step 26: Development

- 90 s in methyl iso-butyl ketone (MIBK)–IPA (1:3)
- 30 s in IPA

Step 27: Plasma Ashing

- 20 s at 5-mbar O_2-pressure

Step 28: Metallisation

- 6 Å titanium (Ti) (0.5 Å/s), rotation
- 100 Å palladium (Pd) (1 Å/s), rotation
- 2900 Å gold (Au) (2-5 Å/s), rotation

Step 29: Lift-off

- 2 h in acetone

- 60 s in IPA

Step 30: Ozone Cleaning

- 10 min at 500-sccm O_2-flow

Step 31: Wet Etching (gate dielectric)

- 7 min in BOE (10:1)
- 1 min in DIW

Step 32: Wet Etching (support layer)

- 10 s in NH_4OH
- 30 s in DIW
- 10 min in HCl–DIW (1:1) (stirrer setting 1.5 or 500 rpm)
- 60 s in DIW
- 30 s in NH_4OH, new beaker
- 60 s in DIW

TOP CONTACT

The top contact of the RTD is deposited on the dedicated mesa, and the ends of the MOSFET gate are anchored.

Step 33: Apply PMMA 950 A6

- Two layers
- 45-s spin at 4500 rpm (1500 rpm/s)
- 2 min on 180°C hotplate

Step 34: EBL (20 kV)

- 250-μC/cm^2 base dose, 6-nm raster

Step 35: Development

- 90 s in MIBK–IPA (1:3)
- 30 s in IPA

Step 36: Plasma Ashing

- 20 s at 5-mbar O_2-pressure

Step 37: Wet Etching (contact)

- 60 s in HCl–DIW (1:1)
- 30 s in DIW

Step 38: Metallisation

- 200 Å Ti (1–2 Å/s), rotation
- 400 Å Pd (1–3Å/s), rotation
- 3400 Å Au (5–10 Å/s), rotation

Step 39: Lift-Off

- 2 h in acetone
- 60 s in IPA

DIODE AND ISOLATION

The outline of the RTD top contact is used to define the final device in a wet etch. In parallel, the MOSFET is masked and isolated .

Step 40: Apply S1813

- 45-s spin at 6000 rpm (1500 rpm/s)
- 90 s on 115°C hotplate

Step 41: Soft UV Lithography Exposure (365-nm line at 20 mW/cm^2)

- 7-s edge bead removal
- 5-s exposure

Step 42: Development

- 1 min in MF319, stir
- 30 s in MF319, stir
- 30 s in MF319, stir
- 30 s in DIW, stir

Step 43: Plasma Ashing

- 60 s at 5-mbar O_2-pressure

Step 44: Hard Bake

- 15 min on 125°C hotplate

Step 45: Wet Etching (layers 20→8/ 4→1, and 7)

- 180 s in H_3PO_4–H_2O_2–DIW (4:4:100)
- 30 s in DIW
- 10 s in HCl–H_3PO_4–DIW (1:4:5), stir
- 60 s in DIW
- 30 s in NH_4OH
- 60 s in DIW

Step 46: Strip Resist

- 2 min in acetone, on 75°C hotplate
- 1 min in IPA

Step 47: Ozone Cleaning

- 10 min at 500-sccm O_2-flow

DEVICE CONTACTS

A tilted evaporation is used to deposit a self-aligned emitter contact for the RTD, as well as self-alignes source and drain contacts for the MOSFET.

Step 48: Apply LOR 10B

- 45-s spin at 3500 rpm (1500 rpm/s)
- 5 min on 190°C hotplate

Step 49: Apply S1805

- 45-s spin at 6000 rpm (1500 rpm/s)
- 90 s on 115°C hotplate

Step 50: Deep UV Lithography Exposure (365-nm line at 0.85 mW/cm^2)

- 18-s exposure

Step 51: Development

- 27 s in MF319, stir
- 30 s in DIW, stir

Step 52: Ozone Cleaning

- 10 min at 500-sccm O_2-flow

Step 53: Oxide etch

- 60 s in HCl–DIW (1:9)
- 30 s in DIW

Step 54: Metallisation

- 150 Å Ti at 20 degree tilt, rotation
- 250 Å Pd at 20 degree tilt, rotation
- 400 Å Au at 20 degree tilt, rotation

Step 55: Lift-Off

- 2 hour in acetone
- 60 s in IPA
- 5 min in Remover 1165, on 75°C hotplate
- 60 s in DIW, stir

INTERLAYER DIELECTRIC

An interlayer dielectric is deposited to planarise the sample, and a sulphur hexafluoride (SF_6)–O_2 dry-etch is subsequently used to access the device contacts.

Step 56: Ozone Cleaning

- 10 min at 500-sccm O_2-flow

Step 57: Dehydrate Sample

- 15 min on 200°C hotplate

Step 58: Apply Cyclotene 3022-46

- 45-s spin at 6000 rpm (1500 rpm/s)
- 60 s on 120°C hotplate

Step 59: Temper Interlayer Dielectric

- 150-l/h N_2-flow
- 10-min ramp from 20 through 150°C
- 20-min ramp from 150 through 250°C
- 50-min hold at 250°C

Step 60: Apply UV26 2.0

- 45-s spin at 4500 rpm (1500 rpm/s)

- 2 min on 130°C hotplate

Step 61: Deep UV Lithography Exposure (240-nm line at 7.5 mW/cm^2)

- 5-s edge bead removal
- 3-s exposure

Step 62: Post Exposure Resist Bake

- 2 min on 110°C hotplate

Step 63: Development

- 45 s in MF26A, stir
- 30 s in DIW, stir

Step 64: Dry Etching (interlayer dielectric)

- (5:50)-sccm SF$_6$–O$_2$-flow, 200 mTorr, 150 W
- 5 min chamber pre-conditioning
- 85-s patterning etch
- 15-sccm O$_2$-flow, 300 mTorr, 75 W
- 35-s mask removal
- (3:25)-sccm SF$_6$–O$_2$-flow, 100 mTorr, 30 W
- 720-s thin-down etch

Step 65: Bake Spacer Dielectric

- 15 min on 200°C hotplate

LOWER METAL

The first circuit metal layer is deposited, forming interconnections and passive circuits.

Step 66: Apply LOR 10B

- 45-s spin at 3500 rpm (500 rpm/s)
- 5 min on 190°C hotplate

Step 67: Apply S1805

- 45-s spin at 6000 rpm (1500 rpm/s)
- 90 s on 115°C hotplate

Step 68: Deep UV Lithography Exposure

- 18-s exposure (365-nm line at 0.85 mW/cm^2)

Step 69: Develop Lift-Off Mask

- 25 s in MF319, stir
- 30 s in DIW, stir

Step 70: Plasma Ashing

- 30 s at 5-mbar O_2-pressure

Step 71: Metallisation

- 50 Å Ti, rotation
- 5000 Å Au, rotation

Step 72: Lift-Off

- 2 hour in acetone
- 2 min in ultra-sonic bath, setting 2
- 60 s in IPA
- 5 min in Remover 1165, on 75°C hotplate
- 60 s in DIW, stir

CAPACITOR DIELECTRIC

A high-permittivity Hf-based dielectric is deposited to allow formation of a capacitor, and via holes are then etched to allow access to the lower metal layer.

Step 73: Ozone Cleaning

- 10 min at 500-sccm O_2-flow

Step 74: ALD

- 20-sccm N_2-flow
- 150°C
- 90× {0.15-s TDMAHf, pump 20 s, 0.015-s H_2O, pump 20 s}

Step 75: Apply S1813

- 45-s spin at 6000 rpm (1500 rpm/s)
- 90 s on 115°C hotplate

Step 76: Soft UV Lithography Exposure (365-nm line at 20 mW/cm^2)

- 5-s exposure

Step 77: Development

- 60 s in MF319, stir
- 30 s in DIW, stir

Step 78: Plasma Ashing

- 60 s at 5-mbar O$_2$-pressure

Step 79: Temper Resist Mask

- 15 min on 125°C hotplate

Step 80: Wet Etching (capacitor dielectric)

- 12 min in BOE (10:1)
- 1 min in DIW

Step 81: Strip Resist

- 2 min in acetone, beaker on 75°C hotplate
- 1 min in IPA

UPPER METAL

The upper and final circuit metal layer is deposited, completing the capacitor, pads, and passive circuits.

Step 82: Apply LOR 10B

- 45-s spin at 3500 rpm (500 rpm/s)
- 5 min on 190°C hotplate

Step 83: Apply S1805

- 45-s spin at 6000 rpm (1500 rpm/s)
- 90 s on 115°C hotplate

Step 84: Deep UV Lithography Exposure (365-nm line at 0.85 mW/cm^2)

- 17-s exposure

Step 85: Develop Lift-Off Mask

- 25 s in MF319, stir

- 30 s in DIW, stir

Step 86: Plasma Ashing

- 30 s at 5-mbar O_2-pressure

Step 87: Metallisation

- 50 Å Ti, rotation
- 5000 Å Au, rotation

Step 88: Lift-Off

- 2 hour in acetone
- 2 min in ultra-sonic bath, setting 2
- 60 s in IPA
- 5 min in Remover 1165, on 75°C hotplate
- 60 s in DIW, stir

PACKAGING

All devices, except for the WTxs, are finalised at this stage. They must further be diced from the bulk of the chip and assembled on a carrier, e.g. as described in Paper X and Chapter 4.

Table A.1: Layer specification for the semiconductor heterostructure on the wafer used in the fabrication of the circuits.

#	Function	Material	Doping	Type
20	Collector	300 Å $In_{0.70}Ga_{0.30}As$	Si: $4.0 \cdot 10^{19}$ /cm^3	n++
19	Collector	300 Å In–Ga–As	Si: $4.0 \cdot 10^{19}$ /cm^3	n++
18	Collector	500 Å $In_{0.53}Ga_{0.47}As$	Si: $3.0 \cdot 10^{19}$ /cm^3	n++
17	Spacer	1000 Å $In_{0.53}Ga_{0.47}As$	Si: $2.0 \cdot 10^{17}$ /cm^3	n
16	Separator	30 Å $In_{0.53}Ga_{0.47}As$	NID	–
15	Barrier	14 Å AlAs	NID	–
14	Well	9 Å $In_{0.53}Ga_{0.47}As$	NID	–
13	Notch	20 Å InAs	NID	–
12	Well	9 Å $In_{0.53}Ga_{0.47}As$	NID	–
11	Barrier	14 Å AlAs	NID	–
10	Separator	30 Å $In_{0.53}Ga_{0.47}As$	NID	–
9	Emitter	200 Å $In_{0.53}Ga_{0.47}As$	Si: $4.0 \cdot 10^{18}$ /cm^3	n
8	Emitter	500 Å $In_{0.53}Ga_{0.47}As$	Si: $1.5 \cdot 10^{19}$ /cm^3	n+
7	Etch Stop	50 Å InP	Si: $1.5 \cdot 10^{19}$ /cm^3	n+
6	Intermediate	1000 Å $In_{0.53}Ga_{0.47}As$	Si: $1.5 \cdot 10^{19}$ /cm^3	n+
5	Etch Stop	50 Å InP	Si: $1.5 \cdot 10^{19}$ /cm^3	n+
4	Channel	100 Å $In_{0.53}Ga_{0.47}As$	NID	–
3	Barrier	10 Å $In_{0.52}Al_{0.48}As$	NID	–
2	Delta Doping	50 Å $In_{0.52}Al_{0.48}As$	Si: $8.0 \cdot 10^{18}$ /cm^3	n++
1	Buffer	1900 Å $In_{0.52}Al_{0.48}As$	Be: $5.0 \cdot 10^{16}$ /cm^3	p
0	Substrate	0.65 mm InP	Fe	SI

B

Electrical Models

*M*ODELLING of millimetre-wave (mmW) devices require equivalent electrical circuits to be identified, and methods to quantify the constituting elements. The following procedures have been used in this thesis.

B.1 RESONANT-TUNNELLING DIODE

An analytic modelling approach was developed to simulate the characteristics of the resonant-tunnelling diode (RTD) used in the circuits presented in this thesis. The current-voltage description is taken from a model developed elsewhere [60], while the charge-voltage behaviour is calculated from the geometry and material parameters designed; a specification of the device layers can be found in Table A.1. In the description below, the intrinsic heterostructure layers refers to layers 10 through 16 and have a $t_{\mathrm{rtd}} = 12.6$-nm total thickness, while their effective permittivity $\varepsilon_{\mathrm{r,eff}} = 14.1$ was used unless otherwise stated. The model was fitted simultaneously to the characteristics of diodes in an $A_{\mathrm{eff}} = 14.9$–41.3-$\mu\mathrm{m}^2$ active area range.

Generally, in one direction, the current through an RTD can be calculated by integrating the product of available carriers on the emitter side and their transmission probability through the multi-barrier structure to the collector [101]. Unfortunately, this is typically not an analytic expression for the resonant-tunnelling current density, J_{res}, at finite temperatures. An approximative approach can be utilised where a narrow Lorentzian transmission probability is assumed to act as a weighted delta-function [102], thereby avoiding non-analytic polylogarithm expressions. Thermionic emission over the multi-barrier heterostructure also contributes to a leakage current den-

sity, J_{lkg}, which dominates at high bias. The total current current density, $J_C = J_{res} + J_{lkg}$, that is fitted to the RTD characteristics in this thesis has been proposed in a similar model [60]. The resonant-tunnelling current density, J_{res}, is accordingly found as

$$J_{res} = J_P \frac{\eta_{res} V_{th}}{V_N - V_T} \bigg/ \left(2 - \sqrt{\frac{8\Gamma_{eff}}{\pi (V_N - V_T)}} \right)$$
$$\times \left\{ \left[1 + \frac{2}{\pi} \arctan \left(\frac{(V_N - V_{CE})}{\Gamma_{eff}} \right) \right] \ln \left(1 + \exp \left(\frac{V_{CE} - V_T}{\eta_{res} V_{th}} \right) \right) \right.$$
$$\left. - \left[1 + \frac{2}{\pi} \arctan \left(\frac{(V_N + V_{CE})}{\Gamma_{eff}} \right) \right] \ln \left(1 + \exp \left(\frac{-V_{CE} - V_T}{\eta_{res} V_{th}} \right) \right) \right\}, \quad \text{(B.1)}$$

where the fitted $J_P = 140$ kA/cm^2 is the approximate peak current density, $V_N = 0.699$ V denotes the negative conductance voltage, $V_T = 0.0533$ V denotes the resonant-tunnelling threshold, $\Gamma_{eff} = 3.38 V_{th}$ is the effective resonance voltage-width, and $\eta_{res} = 1.20$ is the resonance ideality; the thermal voltage, $V_{th} = k_B T_{amb}/q_e$, is found from Boltzmann's constant, k_B, the elemetary charge, q_e, and the ambient temperature, $T_{amb} = 300$ K, assumed. This is accompanied by a leakage current density, J_{lkg}, specified by the model [60], as

$$J_{lkg} = J_V \sinh \left(\frac{V_{CE}}{\eta_{lkg} V_{th}} \right) \bigg/ \sinh \left(\frac{V_V}{\eta_{lkg} V_{th}} \right), \quad \text{(B.2)}$$

where $\eta_{lkg} = 13.4$ is a leakage ideality factor, $V_V = 4.40$ V denotes the voltage threshold for the thermionic emission, and $J_V = m_e^* T_{amb}^2 A_0$ denotes the leakage current at V_V. This thermionic current scales by Richardson's constant, $A_0 = 4\pi m_0 k_B^2 q_e / h_P^3$ where h_P is Planck's constant, m_0 is the free electron mass, and $m_e^* = 0.041$ denotes the relative effective electron mass in the emitter.

The total charge per unit area, $q_{CE} = q_{dep} + q_{trc}$, modelled for the RTD in this thesis has depletion and transit-charge contributions, q_{dep} and q_{trc}, respectively. The intrinsic capacitance, C_0, of the RTD heterostructure can be solved by series connection of the capacitances related to the intrinsic heterostructure layers [61]. Under applied bias, however, band-bending about the RTD will occur due to charging of the emitter and collector. By assuming a thin accumulation layer of carriers at the emitter and a depleted space-charge region on the collector side, the depletion charge can be solved using Poisson's equation, as

$$q_{dep} = 2\kappa_{dep} \sqrt{V_{CE}} - \frac{2\kappa_{dep}^2}{C_0} \left[\ln \left(\kappa_{dep} + C_0 \sqrt{V_{CE}} \right) - \ln \left(\kappa_{dep} \right) \right], \quad \text{(B.3)}$$

where

$$\kappa_{dep} = \varepsilon_0 \varepsilon_{r,eff} \Big/ \sqrt{\frac{2\varepsilon_0 \varepsilon_{r,eff}}{q_e N_{dep}} \left(\frac{\eta_{res} - 1}{\eta_{res}} \right)} \tag{B.4}$$

denotes a depletion constant and $N_{dep} = 2 \cdot 10^{17}$ /cm^3 is the doping density in the depleted spacer layer.

Charges in transit from the emitter to the collector also contribute to a capacitive effect. In this thesis, the transit-charge per unit area, $q_{trc} = -\tau_{trc} J_{res}$, of the RTD is approximated by the resonant-tunnelling current density, J_{res}, and the transit time, τ_{trc}, evaluated as a constant at the negative conductance voltage, $V_{CE} = V_N$, as follows. The assumption that electrons are injected with the average thermal velocity, $v_{th} = \sqrt{2k_B T_{amb}/(\pi m_0 m_e^*)}$, accelerated by a linear field equal to that in the intrinsic heterostructure, traverse the remainder of the depletion layer with a constant velocity, and scatter upon exit, approximates the transit time, as

$$\tau_{trc} = 2\eta_{res} t_{rtd} \left\{ \frac{1}{v_{lin}} - \frac{v_{th}}{v_{lin}^2} \left[\ln(v_{th} + v_{lin}) - \ln(v_{th}) \right] \right\}$$
$$+ \left(\sqrt{\frac{2\varepsilon_0 \varepsilon_{r,eff}}{q_e N_{dep}} \left(\frac{\eta_{res} - 1}{\eta_{res}} \right)} V_{CE} - t_{rtd} \frac{\eta_{res} - 1}{\eta_{res}} \right) \Big/ (v_{th} + v_{lin}) , \quad \text{(B.5)}$$

where $v_{lin} = \sqrt{2q_e V_{CE}/(m_0 m_e^*)}$ is the velocity attained for linear acceleration by the applied bias under the effective-mass approximation.

Fitting of the above model is greatly alleviated under knowledge of the series resistance, R_{ce}, of the RTD. Here, the $\rho_{c,e} = 150$-Ω–μm^2 and $\rho_{c,c} = 25$-Ω–μm^2 specific contact resistivities of emitter and collector, respectively, were estimated and their respective resistances were further accompanied by mesa resistances. Utilisation of both bias polarities required continuity in conductance and charge. By physically transforming the resonance widths in forward and reverse bias by the ideality factors, the model could be fitted more efficiently. An access inductance can also be added by use of standard theory [103], but is negligible for the diode geometries used.

B.2 SLOT-COUPLED DIELECTRIC RESONATOR ANTENNA

As for monolithic slot antennas [98, 99], a transmission line model can be used to describe the input characteristics of the slot-coupled dielectric resonator antenna (DRA), cf. Figure 4.5; this could further be exploited to also study the radiation characteristics. In the case of a uniform transverse electromagnetic (TEM) coupling-slot located on the centre of the ground-plane face of the DRA, the modelling is straightforward. The loaded coupling-slot of length

l_s is approximated as a quasi-TEM transmission line, with characteristic impedance, $Z_{0,c}$, and propagation constant, γ_c. The antenna admittance, Y_A, can thereby be found by use of (1.11), in the centre-fed case as

$$Y_A = \frac{2}{Z_{0,c}} \frac{j\omega C_{tc} Z_{0,c} + \tanh\left(\gamma_c \frac{l_s}{2}\right)}{1 + j\omega C_{tc} Z_{0,c} \tanh\left(\gamma_c \frac{l_s}{2}\right)}, \tag{B.6}$$

where C_{tc} is the terminating capacitance at each end of the coupling-slot. This expression can easily be modified to describe offset-fed coupling-slots, but such a design would have a negative impact on the radiation efficiency.

It is clear that the coupling-slot transmission line parameters must be found to be used in (B.6). For this purpose, the slot line is assumed to have a characteristic impedance, $Z_{0,s}$, in the lossless and unloaded limit case. The quasi-TEM effective permittivity $\varepsilon_{r,s} = (\varepsilon_{r,\text{InP}} + 1)/2$ can be used if the slot line is narrow [104]; a narrow slot width further ensures that any influence from the carrier is small due to the flip-chip stand-off and carrier metallisation void under the DRA. The corresponding capacitance and inductance per unit length of the slot are thereby found, as

$$C'_s = \frac{\sqrt{\varepsilon_{r,s}}}{Z_{0,s} c_0} \tag{B.7}$$

and

$$L'_s = \frac{Z_{0,s} \sqrt{\varepsilon_{r,s}}}{c_0}, \tag{B.8}$$

respectively. The un-loaded and lossless characteristic impedance, $Z_{0,s} = 121\ \Omega$, as well as resistive loss in the slot metallisation and conductive loss in the dielectric body were approximated by numerical fitting to simulated results of the DRA with $l_s = 300\text{-}\mu\text{m-long}$ and $v_s = 20\text{-}\mu\text{m-wide}$ slot. The resistance per unit length was allowed to scale with the skin depth, as

$$R'_s = 15.0 \cdot 10^{-3} \frac{2\rho_m}{\delta_s t_m}, \tag{B.9}$$

while the losses in the dielectric were assumed approximately constant, $G'_s = 1.64\ \text{S/m}$.

Loading of the coupling-slot, induced by the dielectric body of the DRA, can now be added in terms of a radiation conductance per unit length, $G'_r = 16.8\ \text{S/m}$, embedded in a series resonance. This conductance, as well as the resonance frequency and quality-factor of the loaded DRA, $f_r = 61.1\ \text{GHz}$ and $Q_r = 10.0$, respectively, were also be found by numerical fitting. This

corresponds to a capacitance and inductance per unit length, C_r' and L_r', respectively, as

$$C_r' = \frac{G_r'}{\omega_r Q_r}, \tag{B.10}$$

and,

$$L_r' = \frac{Q_r}{\omega_r G_r'}, \tag{B.11}$$

where $\omega_r = 2\pi f_r$ denotes the series resonance angular frequency.

Finally, the impedance and admittance per unit length are thereby

$$Z_c' = R_s' + j\omega L_s', \tag{B.12}$$

and

$$Y_c' = G_s' + j\omega C_r' + 1/\left(j\omega L_r' + \frac{1}{G_r'} + \frac{1}{j\omega C_r'}\right). \tag{B.13}$$

The characteristic impedance and propagation constant of the loaded coupling-slot can be calculated using (1.8) and (1.9), respectively. This model provides a fair accuracy in terms of input characteristics, but simplistic approximations were used here to identify the line parameters and can be improved on many aspects. The general modelling approach, however, should be valid for DRAs similar to those described in this thesis.

C

Numerical Methods

*E*LECTROMAGNETIC method-of-moments solvers, as well as time-domain circuit simulations, have been utilised to design and study the devices and circuits presented in this thesis.

C.1 ELECTROMAGNETIC CALCULATIONS

A dielectric body on a ground-plane can be studied in *COMSOL Multiphysics* using the *electromagetic waves* model. The resonator used for antennas in this thesis provided a full-wave *eigenfrequency* at $61.2 + j2.92$ GHz, instead of 60.4 GHz from the dielectric waveguide model. Similar agreement was found for resonators of limited aspect ratios.

Antenna simulations were performed in *CST Microwave Studio*, typically using the *time-domain solver* with an energy convergence set to -40 dB for iterations utilising *energy-based adaptive meshing*. Analysing very reactive components, standard convergence criteria on reflection coefficient magnitude are not effective. Instead, the susceptance was tracked for the inductive antennas.

C.2 CIRCUIT ANALYSIS

Wavelet generator simulations require time-domain (TD) circuit analysis. Further, support for user defined models is required and one generic alternative is *Qucs* (`http://qucs.sourceforge.net/`). The device models presented in this thesis were implemented using *equation defined devices* and the circuit was solved in a *transient simulation*.

PAPERS

"In physical science a first essential step in the direction of learning any subject is to find principles of numerical reckoning and practicable methods for measuring some quality connected with it. I often say that when you can measure what you are speaking about and express it in numbers you know something about it; but when you cannot measure it, when you cannot express it in numbers, your knowledge is of a meagre and unsatisfactory kind: it may be the beginning of knowledge, but you have scarcely, in your thoughts, advanced to the stage of science, whatever the matter may be."

—Lord Kelvin

Paper I

Paper I

Reproduced, with permission, from:

I. Vakili, L. Ohlsson, M. Gustafsson, and L.-E. Wernersson, "Wideband and Non-Dispersive Wavelet Transmission Using Leaky Lens Antenna," *IET Electron. Lett.*, vol. 49, no. 5, pp. 321–322, Feb. 2013.

Wideband and non-dispersive wavelet transmission using leaky lens antenna

I. Vakili, L. Ohlsson, M. Gustafsson and L.-E. Wernersson

An ultra-wideband, non-dispersive leaky lens antenna system for impulse applications has been designed, fabricated and characterised. An in-house wavelet generator is connected to the antenna to transmit 100 ps-long square pulses with centre frequencies at 45, 60 and 75 GHz. It is shown that the leaky lens antenna has negligible distortion and preserves the pulse shape generated by the millimetre-wave pulse generator.

Introduction: Short pulse radiation is a growing demand in many applications such as imaging, radars, and high data rate wireless communications. These applications require antenna phase linearity over a wide bandwidth of operation. TEM horn [1], Vivaldi, and spiral [2] antennas are examples that show relatively low-dispersive radiation over a wide bandwidth. However, in TEM horn antennas the phase centre moves along the longitudinal axis and in spirals, nonlinear phase variations give pulse distortion and degrade the performance. A combination of leaky wave radiation and a dielectric lens has been proposed for very low-dispersive radiation over a wide bandwidth [3]. An octave bandwidth with excellent pulse preservation is demonstrated in [4, 5]. This is done using a planar-fed leaky lens antenna that has been characterised using a frequency domain system.

In this reported work, the leaky lens antenna has been modified and tested by both frequency-domain and time-domain systems. Its reflection coefficient was characterised by a network analyser, while its transient characteristics were investigated through transmission of 100 ps-long pulses realised by a wavelet generator [6]. Wavelet generators are used in short-range ultra-wideband applications, such as radars and high data rate communications [7, 8]. The wavelet generator presented here consists of a fast switching metal-oxide-semiconductor field-effect-transistor (MOSFET) in series with a resonant tunnelling diode (RTD) which generates short high-frequency pulses. The wavelet generator delivers pulses to one transmitting leaky lens antenna and another is used as a receiver. It is demonstrated that the antenna preserves the pulse shape, i.e. the pulse distortion is negligible.
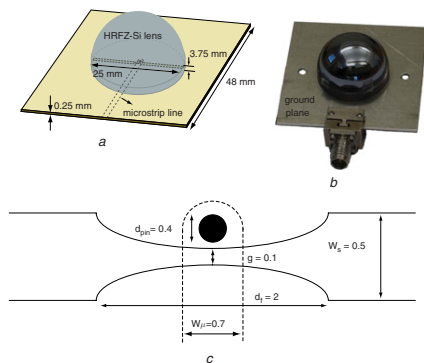

Fig. 1 *Geometry of leaky wave lens antenna (all dimensions in millimetres)*
a 3D view of lens antenna
b Leaky lens antenna prototype
c Microstrip to slot transition details

Antenna design: The antenna consists of a synthesised hemisphere high resistivity float zone-silicon (HRFZ-Si) lens with relative permittivity $\varepsilon_r = 11.67$ integrated to a planar feeding structure. To achieve a fixed phase centre, the shape of the lens has to be elliptical, but fabricating an elliptical lens has difficulties. Instead, a synthesised hemispherical silicon lens with a cylindrical extension at its fictitious focal point may be used as a good approximation of an ellipsoid [9]. In Fig. 1*a*, the lens together with the slot feeding structure is depicted and Fig. 1*b* shows the manufactured lens antenna. The feed is placed at the focal point of the lens. The radius of the lens is $a = 12.5$ mm and the eccentricity is $e = 1/\sqrt{\varepsilon_r}$ [10], which gives the height of the extension, $h = 3.75$ mm. An air gap of 0.25 mm is introduced between the antenna and the planar structure to reduce the sidelobes. This air gap gives an upper bound to the leaky wave propagation direction and is equal to the critical angle of the dielectric ($\theta_c \simeq 73°$) [11]. The resulting radiation is directive and frequency independent [4, 5].

To match the antenna to 50Ω, the microstrip width $W_\mu = 0.7$ mm has been chosen. This microstrip line feeds the slot through a metallic via etched in a 250 µm substrate of Arlon Diclad 880 with permittivity $\varepsilon_r = 2.2$. Fig. 1*c* shows the microstrip to slot connection, which has been optimised to achieve a very low reflection over the frequency range [15, 65] GHz. CST Microwave Studio has been used to design and simulate the antenna.

Frequency-domain measurements: The frequency domain performance of the antenna has been verified by an Agilent E8361A PNA from 15 to 67 GHz. A SouthWest Microwave 2.40 mm end launch connector has been used to connect the manufactured antenna to a 1.85 mm MegaPhase cable. Two antenna prototypes have been manufactured and their reflection coefficients are shown in Fig. 2. It is obvious that the antenna is well matched over the targeted frequency band. This is achieved without use of any matching layers, which are difficult to fabricate at higher frequencies. The main reflection is from the lens–air interface and can be reduced using matching layers [5].
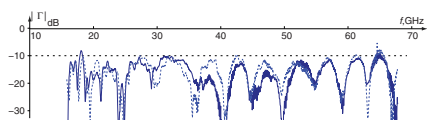

Fig. 2 *Reflection coefficients of two leaky lens antenna prototypes with same dimensions*

Time-domain measurements: To verify the non-distorting pulsed operation of the lens antenna, it was tested together with an in-house fabricated RTD-MOSFET wavelet generator [6]. The wavelet generator is implemented fully on-chip and it consists of an InGaAs RTD, i.e. a negative differential conductance device, connected in series with a $In_{0.53}Ga_{0.47}As$ MOSFET operated as a switch. When switching the generator input gate to a high state, the total conductance in the circuit becomes negative and an oscillation builds up. In this state, as the MOSFET channel is open, the drive voltage falls primarily over the RTD. The frequency of oscillation is controlled by an on-chip resonance circuit and the RTD capacitance, which is dependent on the drive voltage. When the voltage on the gate is returned to a low state, charge transport through the MOSFET is impeded. This turns the total conductance in the circuit positive and the oscillation is quenched; see [6] for details.

During the measurements, a probe station with 100 µm pitch GSG Cascade Infinity Probes was used to access both the MOSFET gate input and the output taken over the on-chip resonance circuit. An Agilent N4906B Serial BERT was used to generate 100ps-long baseband pulses, with a periodic repetition every 10 ns. These pulses were transferred to the input of the RTD-based wavelet generator, switching the output between oscillating and non-oscillating states. The transmitting (Tx) antenna was connected to the isolated port of a bias-T. The receiving (Rx) antenna was connected to the sampling head of a LeCroy WaveExpert 100H sampling oscilloscope with a 30-inch MegaPhase cable with 1.85 mm interfaces. The Tx and Rx antennas depicted in Fig. 3 are separated by 30 cm, measured between the ground planes. Reference measurements were also made using the cable to connect the bias-T and sampling head directly. Three wavelet generators with centre frequencies, $f_c = 45$, 60 and 75 GHz, were used. In Fig. 4*a*, the 100 ps-long reference pulse with $f_c = 60$ GHz is shown. The amplitude of the pulse is normalised to its maximum value, $V_0 = 165$ mV. Figs 4*b* and *c* show the lens to lens transmission and the horn to horn transmission, respectively. It is seen that the pulse width in the leaky lens case remains almost the same as the reference pulse, and the rectangular pulse shape is preserved. The maximum value of the received pulse in the lens to lens configuration is $V_0 = 8.3$ mV and considering the path loss at 60 GHz, the gain of the antenna is found

to be 15.3 dB. In horn to horn configuration the amplitude of the received signal is $V_0 = 15.5$ mV, which corresponds to 19.1 dB gain, in agreement with 19.48 dBi in the manufacturer's specification.
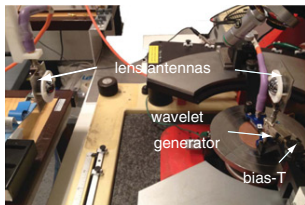
Fig. 3 *Time domain measurement setup using in-house fabricated wavelet generator*
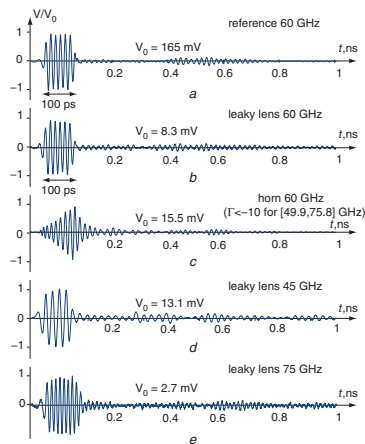
Fig. 4 *Received voltage normalised by maximum received pulse amplitude, V_0. Transmitted pulse is 100 ps long*

a Reference pulse ($f_c = 60$ GHz)
b Lens antenna ($f_c = 60$ GHz)
c Horn antenna ($f_c = 60$ GHz) which is well matched over frequency range [45,75.8] GHz
d Lens antenna ($f_c = 45$ GHz)
e Lens antenna ($f_c = 75$ GHz)

To verify the UWB performance of the antenna system, two additional wavelet generators with 100 ps-long pulses at $f_c = 45$ GHz and 75 GHz were used. The measured lens to lens transmission voltages with 100 ps-long pulses at $f_c = 45$ GHz and $f_c = 75$ GHz are depicted in Fig. 4*d* and *e*, respectively. Considering the path loss and the reference

voltages $V_0 = 186$ mV at $f_c = 45$ GHz and $V_0 = 76.4$ mV at $f_c = 75$ GHz, the corresponding approximate gains are 15.5 dB and 14.8 dB, respectively. These Figures further verify the ultra-wideband gain property and non-dispersiveness of the leaky lens antenna.

Conclusions: A leaky lens antenna has been designed and fabricated. The antenna has been verified by frequency- and time-domain measurements. The frequency-domain results show that the antenna is well matched over the frequency band [15,67] GHz, which is an advantage in adaptive systems. The antenna has been tested using in-house wavelet generators at different frequencies. The results demonstrate pulse radiation through a millimetre-wave radio channel with negligible pulse distortion.

I. Vakili, L. Ohlsson, M. Gustafsson and L.-E. Wernersson (*Department of Electrical and Information Technology, Lund University, Lund 221 00, Sweden*)

E-mail: Iman.Vakili@eit.lth.se

References

1 Shlager, K.L., Smith, G.S., and Maloney, J.G.: 'Accurate analysis of TEM horn antennas for pulse radiation', *IEEE Trans. Electromagn. Compat.*, 1996, **38**, pp. 414–423
2 Elmansouri, M.A., and Filipovic, D.S.: 'Low-dispersion spiral antennas'. *IEEE Trans. Antennas Propag.*, 2012, **60**, pp. 5522–5530
3 Neto, A., Bruni, S., Gerini, G., and Sabbadini, M.: 'The leaky lens: a broad-band fixed-beam leaky-wave antenna', *IEEE Trans. Antennas Propag.*, 2005, **53**, pp. 3240–3246
4 Neto, A., Monni, S., and Nennie, F.: 'UWB, non dispersive radiation from the planarly fed leaky lens antenna Part II: Demonstrators and measurements', *IEEE Trans. Antennas Propag.*, 2010, **58**, pp. 2248–2258
5 Neto, A.: 'UWB, non dispersive radiation from the planarly fed leaky lens antenna Part I: Theory and design', *IEEE Trans. Antennas Propag.*, 2010, **58**, pp. 2238–2247
6 Egard, M., Ärlelid, M., Ohlsson, L., Borg, B.M., Lind, E., and Wernersson, L.-E.: 'In$_{0.53}$Ga$_{0.47}$As RTD-MOSFET millimetre-wave wavelet generator', *IEEE Electron Device Lett.*, 2012, **33**, pp. 970–972
7 Gresham, I. *et al*: 'Ultra-wideband radar sensors for short-range vehicular applications', *IEEE Trans. Microw. Theory Tech.*, 2004, **52**, pp. 2105–2122
8 Ärlelid, M., Egard, M., Ohlsson, L., Lind, E., and Wernersson, L.-E.: 'Impulsed-based 4 Gbit/s radio link at 60 GHz'. *Electron. Lett.*, 2011, **47**, 467–468
9 Filipovic, D.F., Gearhart, S.S., and Rebeiz, G.M.: 'Double-slot antennas on extended hemispherical and elliptical silicon dielectric lenses', *IEEE Trans. Antennas Propag.*, 1993, **41**, 1738–1749
10 Hecht, E.: 'Optics' (Addison-Wesley, 1987 2nd edn)
11 Born, M., and Wolf, E.: Principles of optics (Cambridge University Press, 1999 7th edn)

Paper II

Paper II

Reproduced, in printed version only, from:

L. Ohlsson, I. Vakili, D. Sjöberg, and L.-E. Wernersson, "Time-Domain Wavelet Characterisation With Gating Techniques Applied to Millimetre-Wave Antennas," *IEEE Trans. Antennas Propag.*, Mar. 2015, submitted.

Paper III

Paper III

Reproduced, with permission, from:

M. Ärlelid, M. Egard, L. Ohlsson, E. Lind, and L.-E. Wernersson, "Impulse-Based 4 Gbit/s Radio Link at 60 GHz," *IET Electron. Lett.*, vol. 47, no. 7, pp. 467–468, Mar. 2011.

Impulse-based 4 Gbit/s radio link at 60 GHz

M. Ärlelid, M. Egard, L. Ohlsson, E. Lind and
L.-E. Wernersson

A 4 Gbit/s radio link using impulse-based on-off keying at 60 GHz is demonstrated. The input baseband signals are transferred to radio frequency wavelets through direct conversion, by switching a GaAs gated tunnel diode oscillator on and off. The wavelet generator drives an antenna directly without any buffer or power amplifier. The peak output power is −11 dBm at a power consumption of 30 mW. The signals are detected with an energy detector and the link has a bit error rate $< 10^{-12}$ for distances shorter than 35 cm.

Introduction: The worldwide unlicensed band around 60 GHz may provide bit rates of several Gbit/s, where the large available bandwidth makes it possible to use robust impulse radio with low-level modulation and high throughput [1]. However, further research related to the hardware for the millimetre (mm)-wave front-end is required, addressing speed, power, and efficiency in order to fully exploit the potential. We report on a short-range, high-speed transmitter operating at 60 GHz which for the first time demonstrates its function in an impulse-based radio link. The transmitter is based on direct conversion of baseband signals to radio frequency (RF) wavelets by switching a resonant tunnelling diode (RTD) LC-tank oscillator on and off. The input baseband signal for the oscillator may be used to control the position, length, amplitude, frequency, and phase of the generated wavelet. In this Letter, the first results on bit error rate tests of the wavelet generator are presented and the transmitter is used to demonstrate transmission at a bit rate of 4 Gbit/s using impulse radio on-off keying (IR-OOK) over an wireless error-free data link at a distance of 35 cm. The transmitter is designed without any power amplifier or buffer and drives a 50 Ω horn antenna load directly, which is an advantage of the low-complexity technology. The technique is inherently scalable and the carrier frequency is extendable to a few hundred gigahertz.

System description and wavelet generator performance: The schematic diagram in Fig. 1a shows the implementation developed using only one active device with direct conversion from baseband to RF. The transmitter circuit is an LC-tank oscillator, in which the tank consists of a coplanar waveguide stub acting as an inductance coupled with the output capacitance of a gated tunnel diode (GTD). The GTD consists of an RTD integrated adjacent to a permeable gate, which enables control of the output conductance of the GTD by changing the potential on the input terminal [2]. The active device area of the GTD is $2 \times 18 \ \mu m^2$, and a chip photo of the transmitter circuit is shown in Fig. 1b, the total chip size is $270 \times 200 \ \mu m^2$. The function of the circuit has been described for an implementation with a centre frequency of 20 GHz in [3]. The 60 GHz transmitter presented here has a peak output power of −11 dBm, a phase noise of –111 dBc/Hz at 1 MHz offset, and consumes 30 mW, in continuous-mode operation. The general operation in pulsed-mode is straightforward; when the control signal at the baseband input is high, the GTD is biased in a region with positive differential conductance, and the oscillator is in its off-state. When the control signal is decreased, the GTD is switched to a region with negative differential conductance and an oscillation will build up. The oscillation is rapidly quenched when the control signal returns to the off-state, as shown for the 56.4 ps short wavelet in Fig. 2. The peak-to-peak voltage of the oscillator is 177 mV, with loss de-embedded. Wavelets down to 30 ps have been realised corresponding to a −10 dB bandwidth of 20 GHz [4]. The signal generated by the oscillator is coherent and stable; measurements show that the conversion from baseband pulse to RF wavelet is completed without any additional jitter or errors. To characterise the wavelet generator itself, the pulse-error rate of the wavelet generators has been characterised and values below 10^{-12} over a V_c bias range of 50 mV at 2.5 Gpulses/s operation has been measured. The voltage range is determined by the negative differential conductance in the GTD and the value of the capacitance, C_S, used in the circuit design [5]. Circuits including an additional $400 \ \mu m^2$ Schottky diode, as shown in Fig. 1b, have been studied to achieve amplitude shift keying (ASK) modulation. Although the diode increases the power consumption by a factor of 2, it helps to stabilise the bias network. The energy consumption for the transmitter is 7.5 pJ/bit for 4 Gbit/s, while it is 5.2 pJ/bit for 12.5 Gbit/s.
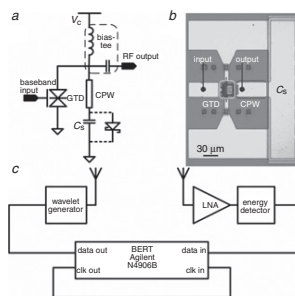

Fig. 1 *Transmitter circuit schematics of wavelet generator, chip photo, and system description*

a Transmitter circuit schematics
b Chip photo
c System description
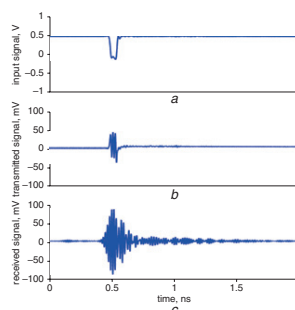
Fig. 2 *Input signal of wavelet generator (Fig. 2a); on-chip measurement of generated signal (Fig. 2b) (centre frequency of wavelet is 59 GHz, de-embedded voltage swing is 177 mV_pp; pulse length of baseband signal is 53.9 ps, wavelet is 56.4 ps); received wavelet after transmission (Fig. 1c)*
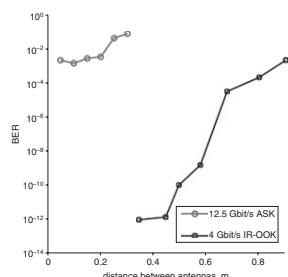
Fig. 3 *BER for 4 Gbit/s using impulse radio OOK and 12.5 Gbit/s using binary ASK for different distances between Tx and Rx antennas*

Data pattern of 2^{21} PRBS used in both cases. For IR-OOK, BER is below 10^{-12} for distances shorter than 35 cm

Transmission tests: The entire system is evaluated when measuring the bit error rate; Fig. 1c describes the test bed for the wireless measurements. The wavelet generator is connected directly to the antenna without any buffer or power amplifier at the transmitter. Both transmit and receive antennas are horn apertures from the Flann microwave, which have a gain of 20 dBi, from 50 to 75 GHz. The LNA is an HLNAV-383 with 30 dB gain from 50 to 67 GHz with a P_{DC} of 1625 mW and the energy detector is an HFD15P (10 mV/mW to 50 Ω load), both from HXI. The receiver is only suitable for non-coherent amplitude modulation although the transmitter can support either binary ASK or different types of impulse-radio modulations, such as

OOK, pulse position modulation (PPM), and binary phase shift keying (BPSK). In Fig. 3, the measured bit error rates for two different modulation types, bit rates, and distances are shown, where both measurements use a pseudorandom bit sequence (PRBS) of 2^{21} bits. For the 4 Gbit/s measurement, the bit error rate (BER) is below 10^{-12} when the antenna separation is less than 35 cm. When increasing the bit rate to 12.5 Gbit/s, the measured bit error rate increases. A comparison between the transmitted wavelet and the received wavelet is shown in Fig. 2; the received signal is distorted both in shape and in length as an effect of the channel, antennas, and LNA. However, the generated signal strength is equal in the two cases after de-embedding gain and loss. The distortion reduces the distinction between the two different amplitude levels in the binary ASK modulation, although the wavelet generator itself is able to quench the signal even at 12.5 Gpulses/s as verified by the pulse-error rate tests in [4] through wired measurement.

Discussion: To compare the transmitter presented in this Letter, three different demonstrated radio links with impulse-based transmitter topologies have been selected. Lee *et al.* [1] presented a fully integrated transceiver at 60 GHz with 2.5 Gbit/s bit rate, BER $< 10^{-12}$ at 4 cm separation using OOK modulation with an RF switch; the transmitter consumes 183 mW with 7.6 dBm output power. A different approach is found in the work of Nakasha *et al.* [6], where a passband filter at 85 GHz is used to obtain wavelets from a 6.5 ps-long baseband pulse. The demonstrated bit rate is 10 Gbit/s with BER $< 10^{-12}$ at 10 cm separation and the power consumption is 790 mW and the transmitted peak power is -22 dBm, also using OOK modulation. In [7], Sasaki and Kikkawa presented a transmitter for IR-OOK at 2.4 GHz. The difference between OOK and IR-OOK is distinguished by the additional separation between symbols found in IR-OOK. The radio link demonstrates 200 Mbit/s with BER $< 6.89 \times 10^{-9}$ at 9 cm separation; the transmitter digitally generates a Gaussian pulse and consumes 30 mW with an output power of -34 dBm. Generally, our implementation either increases the bit rate by a factor of 10 or reduces the power consumption by a factor of 10 compared with the transmitters found in [1, 6, 7]. The receiver power consumption is 103, 275, and 43 mW for [1], [6], and [7], respectively. In addition, our design can handle different types of modulation schemes and the direct wavelet synthesis is an implementation with only one active device that may be realised as an add-on to an antenna. The measurements show that the generated RF signal is coherent and stable with a low BER and that transmission of the short pulses may be an effective way to characterise the radio link. The wireless transmission of 4 Gbit/s is the highest bit rate achieved using impulse radio OOK, to the authors' best knowledge.

Conclusion: A wavelet generator with pulse lengths down to 30 ps with -11 dBm peak power has been realised. The circuit has been used in a wireless demonstration of 4 Gbit/s with OOK impulse radio and 12.5 Gbit/s with binary ASK modulation. The power consumption of the transmitter ranges from 30 to 65 mW depending on the circuit implementation, which gives an energy consumption of 5.2 pJ/bit, for 12.5 Gbit/s operation.

M. Ärlelid, L. Ohlsson and L.-E. Wernersson (*Department of Electrical and Information Technology, Lund University, Lund 221 00, Sweden*)

E-mail: mats.arlelid@eit.lth.se

M. Egard and E. Lind (*Department of Solid State Physics, Lund University, Lund 221 00, Sweden*)

References

1 Lee, J., Huang, Y., Chen, Y., Lu, H., and Chang, C.: 'A low-power fully integrated 60GHz transceiver system with OOK modulation and on-board antenna assembly'. ISSCC Dig. Tech. Pprs, Grenoble, France, February 2009, pp. 316–317
2 Lind, E., Lindström, P., and Wernersson, L.-E.: 'Resonant tunneling permeable base transistors with high transconductance', *IEEE Electron Device Lett.*, 2004, **25**, (10), pp. 678–680
3 Egard, M., Ärlelid, M., Lind, E., Astromskas, G., and Wernersson, L.-E.: '20 GHz wavelet generator using a gated tunnel diode', *IEEE Microw. Wirel. Compon. Lett.*, 2009, **19**, (6), pp. 386–388
4 Ärlelid, M., Egard, M., Lind, E., and Wernersson, L.-E.: 'Coherent V-band pulse generator for impulse radio BPSK', *IEEE Microw. Wirel. Compon. Lett.*, 2010, **20**, (7), pp. 414–416
5 Egard, M., Ärlelid, M., Lind, E., and Wernersson, L.-E.: 'Bias stabilization of negative differential conductance oscillators operated in pulsed mode', *IEEE Trans. Microw. Theory*, 2011 (doi:10.1109/TMTT.2010.2103230)
6 Nakasha, Y., Sato, M., Tajima, T., Kawano, Y., Suzuki, T., Takahashi, T., Makiyama, K., Ohki, T., and Hara, N.: 'W-band transmitter and receiver for 10-Gb/s impulse radio with an optical–fiber interface', *IEEE Trans. Microw. Theory*, 2009, **57**, (12), pp. 3171–3180
7 Sasaki, N., and Kikkawa, T.: 'Bit error rate measurement of IR-UWB CMOS transmitter and receiver'. IEEE Asia-Pacific Microw. Conf., Singapore, December 2009, pp. 249–252

Paper IV

Paper IV

Reproduced, with permission, from:

A 15-Gb/s Wireless ON-OFF Keying Link

LARS OHLSSON AND LARS-ERIK WERNERSSON

Department of Electrical and Information Technology, Lund University, Lund 22100, Sweden

Corresponding author: L. Ohlsson (lars.ohlsson@eit.lth.se).

ABSTRACT Bit-error rate measurements for ON-OFF keying modulation at multigigabit per second rates over a V-band wireless link are presented. Serial data-rates from 2.5 to 20 Gb/s were studied for a 2^{31}-1 bit random sequence. Error-free data transfer over a 0.3-m link was achieved at up to 10 Gb/s. Acceptable bit-error rates, $<10^{-5}$ and 10^{-3}, were measured at up to 1.5 m for 10- and 15-Gb/s data-rate, respectively. The performance was achieved using a transmitter that consists of an integrated wavelet generator, whereas the receiver was built from off-the-shelf waveguide components. The results demonstrate that very high data-rates may be achieved using binary modulation and short symbols generated in an efficient V-band transmitter. The system is benchmarked against state-of-the-art transceiver systems with multigigabit per second data-rates.

INDEX TERMS Multi-Gb/s, on-off keying (OOK), wireless communication.

I. INTRODUCTION

Wireless communication at data-rates exceeding 100 Gb/s are required to meet future demands [1]. Long-haul fibre links already show performance in excess of this [2], and last-mile millimetre-wave links are considered for wireless back-haul between cellular access points [3]. As of today, the standards for short-range multi-Gb/s wireless access, e.g. IEEE 802.15.3c, specify operation over up to 10 m at data-rates of a few Gb/s [4]. However, there are application areas which require even higher data-rates over shorter distances. One example is the computation area, where chip-to-chip communication and intra-connects can provide reduced routing complexity [5], [6]. Another example is wireless personal area networks (WPANs), where indoors streaming of media, kiosk downloads, and rapid device synchronisation is attractive [7], [8]. To achieve the required performance in such wireless systems, the limits of data-rate, energy-efficiency, and range in Gb/s wireless links must be investigated outside the present frameworks of standardisation. Such implementations may be operated in un-licensed bands, and pave the road towards future standardisation.

Interestingly, the targeted digital modulation format affects the front-end design challenges. To illustrate this, symbol sequences of typical modulation schemes are exemplified in Fig. 1. On the one hand, binary amplitude-shift keying (2-ASK) allows each radio symbol to hold one bit of data. A high data-rate thereby implies an equally high symbol-rate. This is the case for on-off keying (OOK), as illustrated in Fig. 1(a), which is a popular full-level 2-ASK sub-format.
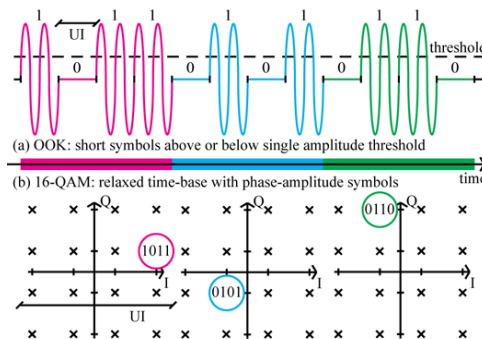
FIGURE 1. Illustration of two typical modulation schemes which can provide wireless Gb/s performance between integrated front-ends. (a) OOK is based on rapid switching about a threshold level, while (b) 16-QAM relies on accurately defined and detected phase-amplitude changes in the signal.

In OOK, the transmitter turns the carrier signal on and off and the receiver evaluates if the signal exceeds a certain threshold level. Wavelet generators and fast energy detection receivers [9], [10], may be used to push the performance in such spread-spectrum systems by increased symbol-rate. On the other hand, for high-order modulation schemes, a quantised constellation of unique phase-amplitude symbols maps the permutations of a multi-bit sequence. This is utilised, e.g. in 4-bit quadrature amplitude

modulation (16-QAM), as shown in Fig. 1(b). To achieve a certain data-rate, the QAM symbol-rate can be relaxed by a factor equal to the number of bits per symbol. The symbol unit interval (UI), as illustrated in Fig. 1, is thereby prolonged and more time may be spent on hardware processing, e.g. sampling in analogue-to-digital converters. However, signal mixing, amplification, and sampling in high-order modulation schemes results in increased power dissipation. The increase is typically a factor of 10 in the transmitter and a factor of 5 in the receiver, based on current multi-Gb/s implementations [11], [12], which may be significant in battery-powered applications. The QAM sub-format of quadrature phase-shift keying (QPSK) has the property of constant power-level in all symbols. This ideally means that the dynamic range of the receiver may be reduced. However, to combat the influences of path-loss variation in the wireless link, e.g. from changing distance and signal fading, high receiver dynamic range, e.g. via baseband limiting amplifiers [13], is beneficial for all the above modulations.

To realise better transceivers, device optimisation and circuit innovation in silicon and various III-V technologies continues to be explored extensively in the millimetre-wave spectrum, 30–300 GHz, [14]. On the one hand, implementations in silicon technology allows for digital signal processing in complementary logic at a high integration level. This alleviates the implementation of I/O buffers, high-order modulation schemes [15], and hybrid switching transmitters [16]. On the other hand, III-V technologies provide advanced devices and improved transistor performance, especially with the recent development of III-V metal-oxide-semiconductor field-effect-transistors (MOSFETs). Specifically, III-V MOSFETs currently provide high transconductance and low on-resistance, as compared to other III-V transistors [17], and can be used as rapid switches [9]. Such transistors may be exploited in high-speed short-range wireless communication where efficient and simplistic implementations need to be considered to maintain energy-efficiency. Further, resonant-tunneling diodes (RTDs) in III-V heterostructures may be used for signal generation up to the THz-spectrum [18]. Schottky diodes, or heterojunction backward diodes [19], may be used in envelope detectors, providing down-conversion of multi-Gb/s OOK signals [20]. Systems in III-V technology also have access to low-loss passives and efficient antennas on-chip based on the insulating substrate [21]. Ultimately, to access wider channel bandwidths that allow higher symbol-rates, a shift towards front-end technologies operating at higher frequencies, will be required. Also, scaling towards terahertz frequencies makes it feasible to reduce the physical size of antenna elements and arrays [22].

In this paper, we demonstrate wireless communication measurements at serial data-rates up to 20 Gb/s. A III-V wavelet generator with sub-period start-up [9] is used together with off-the-shelf V-band, 50–75 GHz, components in waveguide assemblies. We also evaluate and discuss the transmitter and receiver performance, including output

FIGURE 2. Transceiver for Gb/s on-off keying communication. (a) Schematic setup for bit-error rate measurements, and (b) photograph of transmitter.

power, sensitivity, and energy-efficiency. Also, the concept of transceiver omni-distance is defined and utilised for benchmarking.

II. MULTI-Gb/s WIRELESS TRANSCEIVERS

In recent years, the first wireless transceiver front-ends operating at data-rates approaching, or exceeding, 10 Gb/s have been demonstrated. Most of these multi-Gb/s implementations operate in the V-band. Transmitter front-ends typically achieve output power levels ranging from 0 to +10 dBm, and have been implemented for OOK [11], [13], [23]–[25], 2-ASK [5], [6], [10], [26], QPSK [15], [27]–[29], and 16-QAM [12], [15], [30], [31]. Receiver front-ends for ASK and OOK operate by energy detection to demodulate the data, with demonstrated input referred sensitivities as low as −33.7 dBm [10]. For demodulation of phase-defined symbols, e.g. 4-QPSK and 16-QAM, coherent receivers are required. QAM receiver front-ends have been shown with sensitivity levels of −54.2 dBm, but their symbol-rates are currently limited to about 4 GS/s [12]. Finally, wireless communication between multi-Gb/s transceivers has also been demonstrated. The record link distance of 3 m was achieved for 2-ASK at a bit-rate of 12 Gb/s using high-gain horn antennas [10]. By use of integrated antennas separated by a 5 mm link, a data-rate of 10 Gb/s/channel was achieved in two parallel 2-ASK streams diplexed in 57 and 80 GHz channels [6]. However, by use of integrated antennas communicating in 16-QAM over 20 cm, a data-rate of 16 Git/s has been demonstrated [12].

To allow a comparison of wireless transceivers in various implementations, a set of applicable figures-of-merit needs to be defined. The link budget in line-of-sight is set by the transmitter output power, P_{Tx}, the receiver sensitivity, S, i.e. minimum received input power, P_{Rx}, which can be detected, via Friis's transmission equation

$$P_{Rx} = P_{Tx} G_{A,Tx} \left(4\pi d f_c / c\right)^2 G_{A,Rx} / L , \qquad (1)$$

where $G_{A,Tx}$ and $G_{A,Rx}$ are the realised gains of the transmit and receive antennas, respectively, d is the link distance, f_c is the carrier frequency, L is the implementation loss, and c is the speed of light. The transmit and receive antennas are often equal, allowing a more compact notation for their gain, $G_A = G_{A,Tx} = G_{A,Rx}$. The power dissipations of the transmitter, $P_{dc,Tx}$, and receiver, $P_{dc,Rx}$, front-ends are intuitively found from the products of bias current and voltage. The total power dissipation of the transceiver, $P_{dc} = P_{dc,Tx} + P_{dc,Rx}$, when operated at a certain bit-rate, r, may be used to define the transceiver energy-efficiency, $EE = P_{dc}/r$. Further, having evaluated the link for a random symbol sequence at the limit of an acceptable bit-error probability, p_e, the normalised transceiver energy-efficiency, $NEE = P_{dc}/(rd)$, is found.

Portable wireless multi-Gb/s transceivers must be able to achieve a certain link distance by the use of integrated antennas, but front-ends are often evaluated using external antennas. To allow a comparison of transceiver front-end pairs tested under various conditions, the antenna gain and achieved link distance may be used to evaluate the equivalent omni-distance, or intrinsic front-end distance, d_i. The omni-distance is defined here as the equivalent link distance when using hypothetical omni-directional antennas with unit radiation efficiency. This is a representative figure-of-merit for comparison of the intrinsic performance of front-end transceivers, although antenna distortion is a variable of uncertainty if the antenna technologies differ significantly. A rigorous definition of the omni-distance was derived by use (1), equating the transmission loss for the implemented antenna gains and the link distance to the corresponding expression for $G_A = 0$-dBi antennas at the omni-distance. Consequently, it is found that

$$d_i = d/\sqrt{G_{A,Tx}G_{A,Rx}} \cong d/G_A, \qquad (2)$$

where the final approximation assumes equal transmit and receive antennas. Given knowledge of the transceiver omni-distance, it follows from (1) that the achievable link distance is doubled for every 6 dB of added transmission gain. Further, an omni-transceiver energy-efficiency, $NEE_i = P_{dc}/(rd_i)$, is also defined. This figure-of-merit is used to evaluate the normalised transceiver energy-efficiency without influence of the specific antenna gain in the test setup.

In chip-to-chip scenarios, typical link distances of 10 mm and compact antennas with 0 dBi gain, i.e. dipole- or patch-like directivity and a few decibels of radiation loss, can be assumed [5]. Corresponding specifications for WPAN scenarios are link distances of at least 50 mm and, as larger areas may be populated on- or off-chip, antenna gains of approximately 7 dB [11]. In both of the above cases, this results in a required omni-distance of $d_i = 10$ mm for short-range multi-Gb/s wireless transceiver front-ends.

III. OOK TRANSCEIVER SETUP
To test the limits of OOK modulation, a transceiver was implemented as illustrated in Fig. 2(a). An Anritsu MP1800A Signal Quality Analyzer, equipped with a 32-Gb/s pulse
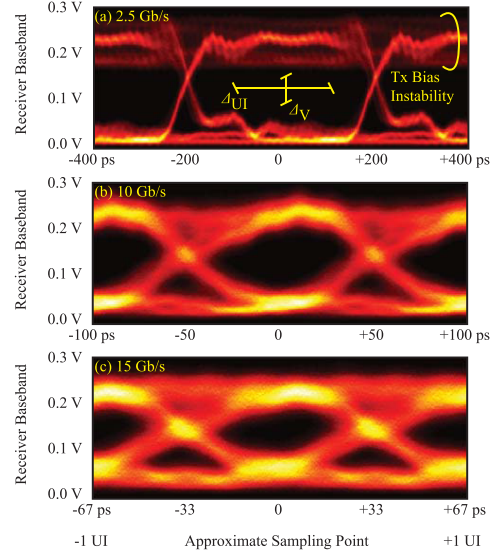
FIGURE 3. Measured symbol eye diagrams for a 15-PRBS at 0.3-m channel distance. The data-rate is (a) 2.5, (b) 10, and (c) 15 Gb/s. A schematic illustration of the eye margins is shown on the 2.5-Gb/s eye.

pattern generator (PPG) and a high-sensitivity error detector (ED), was used to generate data patterns and evaluate received errors. No clock-recovery was implemented and the clock was instead wired directly from the PPG to the ED. An $n = 2^N - 1 = 2^{31} - 1$ bit pseudo-random binary sequence (31-PRBS) of data with high and low levels of $+0.6$ and -0.6 V, respectively, was fed to the probed transmitter front-end. As applicable for OOK, the data-sequence was translated into carrier on- and off-states for high and low level, respectively.

A coherent RTD-MOSFET wavelet generator with sub-period start-up and quench was used to up-convert the input baseband data-pattern to the V-band. Using the same device design but a more streamlined processing scheme, this wavelet generator was based on a previous implementation [9]. It provided an output power level of approximately $+5$ dBm at 62.5-GHz carrier-frequency in the on-state. In the off-state, the 130-nm III-V MOSFET implemented in series with the 35-μm^2 RTD blocked the bias current and no oscillation was generated. The output of the wavelet generator was probed with an RF-probe and the signal was then fed to a 20-dBi gain V-band horn antenna via a bias-T and an adapter, as shown in Fig. 2(b). The probe, bias-T, and adapter have insertion loss specifications of 1 dB, 2 dB, and 1 dB, respectively, corresponding to implementation loss of approximately $L = 4$ dB. The signal was sent over a line-of-sight channel at link distances of $d =$
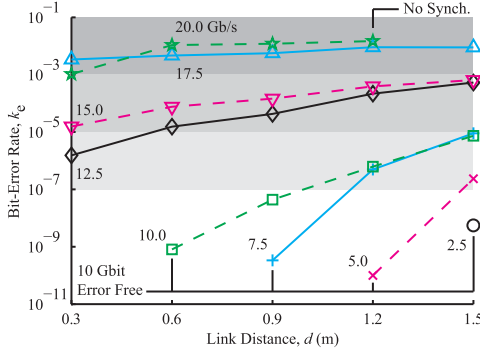
FIGURE 4. Measured wireless 2.5 to 20-Gb/s on-off keying bit-error rate in a line-of-sight scenario. The carrier-frequency was approximately 62.5 GHz.
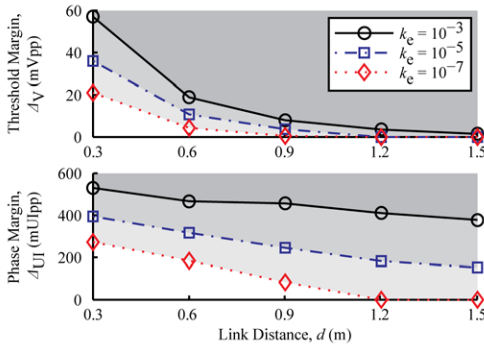
FIGURE 5. Measured eye margins for bit-error rates $k_e < 10^{-3}$, 10^{-5}, and 10^{-7} at 10 Gb/s data-rate, i.e. with a 100-ps UI. Both margins, i.e. threshold, Δ_V, and phase, Δ_{UI}, are given peak-to-peak at the sampling point.

0.3, 0.6, 0.9, 1.2 and 1.5 m. In such far-field line-of-sight, the channel pathloss, L_{FS}, may be identified from (1) as $L_{FS} = (4\pi d f_c/c)^2$. The pathloss levels at the realised link distances were thereby varied from 57.9 dB to 71.8 dB. Further, the evaluated link distances correspond to omni-distances up to 15 mm.

On the receiving side, an identical horn antenna was connected directly to the waveguide input of a V-band amplifier. This amplifier provided nominally 26 dB gain from 50 to 75 GHz, and consumed 243 mA at 12 V bias. The total receiver power dissipation was thereby 2.92 W. The amplified waveform was de-modulated using a V-band envelope detector, converting its input power to a received baseband voltage. This zero-bias detector has a mean specified continuous-wave voltage sensitivity of 2.9 V/mW at −20-dBm input level for 1-MΩ termination of the IF-output. In the setup used here, however, the non-linear detector was terminated with the

50-Ω input of the ED. This drastically lowered the detector voltage sensitivity, but also reduced its symbol transition-time, i.e. widening its IF-bandwidth for high-rate operation. The resulting input referred receiver sensitivity level is evaluated below.

In the MP1800A, the received energy detector output signal was synchronised to find the ideal sampling point within the symbol UI. A total of number of $m = 10^{10}$ bits, i.e. 10 Gbits in binary OOK, were evaluated for each measurement. The number of received faulty bits, m_e, was used to calculate the ratio of erroneous bits, $k_e = m_e/m$, commonly and ambiguously referred to as bit-error rate. This is a good estimate of the bit-error probability, $p_e \approx k_e$, if the utilised PRBS is long enough to emulate a random sequence when repeated. It has been shown for similar systems that bit-error rate results may be strongly underestimated if the utilised PRBS length is too short to provide appropriate randomness [13]. Eye diagrams were captured using a LeCroy 100H oscilloscope with a SE-100 sampling head connected to the receiver output, for a 15-PRBS of data due to post-processing memory limitations.

IV. OOK TRANSCEIVER RESULTS

The RTD-MOSFET was biased at 1.85 V and consumed up to 13.5 mA, increasing with data-rate, yielding transmitter front-end energy-efficiencies, $EE_{Tx} = P_{dc,Tx}/r$, down to 1.25 pJ/bit. Specifically, the realised transmitter front-end energy-efficiencies were $EE_{Tx} = 7.70$, 4.00, 2.79, 2.17, 1.81, 1.55, 1.36, and 1.25 pJ/bit, respectively, for the data-rates increasing in equal steps from $r = 2.5$ to 20.0 Gb/s. This compares favourably to a state-of-the-art V-band transmitter implementation in silicon technology where the transmitter achieves 2.94 pJ/bit at 10.7 Gb/s [11]. The resulting receiver power dissipation, receiver front-end energy-efficiency, $EE_{Rx} = P_{dc,Rx}/r$, and the total transceiver energy-efficiency are high, as compared to state-of-the-art. In Table I, which will be discussed below, the summarised performance of the OOK transceiver is compared to state-of-the-art implementations for wireless multi-Gb/s communication systems.

The received symbol eye diagrams at 0.3 m channel distance, captured at 2.5, 10, and 15-Gb/s data-rate are shown in Fig. 3(a-c), respectively. Increasing the data-rate, the eye has a saturated region around the sampling-point up to approximately $r = 10$-Gb/s, as seen in Fig. 3(b), where the symbol UI is $1/r = 100$ ps. At this data-rate, the symbol transition-time is of approximately the same length as the UI. The eye thereby starts to close at higher data-rates, as can be seen in Fig. 3(c). From the link budget defined by (1), i.e. $P_{Rx} = P_{Tx}G_A^2/(L_{FS}L)$, the input power level to the receiver amplifier was found to range from −16.9 to −30.9 dBm as the channel distance was increased from 0.3 to 1.5 m, respectively. After amplification and conversion to baseband, the maximum detector amplitudes were 297 mV at the shortest distance, and 54 mV at the longest link distance. The received on-level is seen, in Fig. 3(a), to be distributed peculiarly at

TABLE 1. Benchmark comparison of multi-Gb/s wireless transceivers.

Quantity	*Symbol* (Unit)	[11]	[5]	[13]	[10]	[15] [a]	[12] [a]	This Work
Author Affiliations	——	K.A.I.S.T. (Daejeon)	Sony Corp. (Tokyo)	Southeast U. (Nanjing)/ E.P. Montreal	Hiroshima U. (Higashi-Hiroshima)	Tokyo I.T./ Sony Corp. (Tokyo)	Tokyo I.T.	Lund U.
Publication Year	——	2013	2010	2014	2013	2011	2011	2014
Circuit Technology	——	90-nm CMOS	40-nm CMOS	90-nm CMOS	40-nm CMOS	65-nm CMOS	65-nm CMOS	130-nm III-V
Antenna Technology	——	On-board Yagi-Uda	On-board Bond-Wire	On-board Yagi-Uda	D-band Horn	On-board Aperture	On-board Aperture	V-band Horn
Modulation Format	——	OOK	2-ASK	OOK	2-ASK	4-QPSK/ 16-QAM	16-QAM	OOK
Centre-Frequency	f_c (GHz)	60	57	45	134	60.5	60.5	62.5
Data-Rate	r (Gb/s)	10.7	11	5	12	8/ 11	**16**	10/ 15
Limit Bit-Error Rate	k_e (m_e/m)	10^{-12}	10^{-11}	10^{-12}	10^{-5}	10^{-3} [a]	10^{-3} [a]	$10^{-5}/ 10^{-3}$
PRBS Exponent	N	7	7	7	31	—— [a]	—— [a]	31
Transmitter Power-Dissipation	$P_{dc,Tx}$ (mW)	31.5	29	61.6	77.0	252	247	**21.6/ 23.3**
Transmitter Energy-Efficiency	EE_{Tx} (pJ/bit)	2.94	2.64	12.3	6.42	31.5/ 22.9	15.4	**2.17/ 1.55**
Output-Power [b]	P_{Tx} (dBm)	+4.4	0	+7.6	+2.8	**+9.5**	+5.4	+5
Receiver Power-Dissipation	$P_{dc,Rx}$ (mW)	**36.0**	41	53.6	132	172	204	2920
Receiver Energy-Efficiency	EE_{Rx} (pJ/bit)	3.36	3.73	10.7	11.0	21.6/ 15.6	12.8	292/ 194
Sensitivity [c]	S (dBm)	−30.4	−30.5	−32.5	−33.7	−28.6/ −38.1	**−54.2**	−30.9
Transceiver Power-Dissipation	P_{dc} (mW)	**67.5**	70	115	209	424	451	2940
Transceiver Energy-Efficiency	EE (pJ/bit)	**6.31**	6.36	23.0	17.4	53.0/ 38.5	28.2	294/ 196
Antenna Gain	G_A (dBi)	6.6	0	8.7	24	2	2	20
Link Distance	d (m)	0.10	0.014	0.40	**3.00**	0.05	0.20	1.50
Omni-Distance [d]	d_i (mm)	21.9	14.0	54.0	11.9	31.5	**126**	15.0
Normalised Transceiver Energy-Efficiency	NEE (pJ/bit/m)	63.1	455	57.6	**5.81**	1060/ 771	141	196/ 131
Omni-Transceiver Energy-Efficiency [e]	NEE_i (pJ/bit/mm)	0.288	0.455	0.427	15.8	1.68/ 1.22	**0.223**	19.6/ 13.1

The transceivers are ordered with increasing power dissipation from left to right. The three best implementations are highlighted by shading for figures-of-merit (rows) where "good" or "bad" is well-defined; the best is indicated by bold font.

[a] The high-order implementations have high limit bit-error rates at unknown PRBS lengths [12] [15], challenging the validity of the comparison.

[b] Output power is the high symbol power for OOK, 2-ASK, the constant symbol power for 4-QPSK, and the maximum symbol power for 16-QAM.

[c] Sensitivity is stated as the power at the receiver antenna port which must be detected during the benchmarked communication measurements, found via (1). This is the high symbol power for OOK and 2-ASK, the constant symbol power for 4-QPSK, and the minimum symbol power for 16-QAM. Assuming an even-spaced voltage constellation with equal probability for 16-QAM, the average symbol power is −2.55 dBmax and the minimum symbol power is −9.54 dBmax.

[d] Omni-distance is the link distance normalised over the antenna gain according to (2), for front-end comparison.

[e] Omni-transceiver energy-efficiency is the transceiver energy-efficiency normalised over the omni-distance, for front-end comparison.

2.5-Gb/s, as compared to the more Gaussian distributions seen at higher data-rates. This is attributed to transmitter bias instability when the on-state is held continuously, i.e. for several repeated 2.5-Gb/s on-symbols. Also, a noticeable level of detector RF-leakage can be seen as an approximately $1/f_c = 16$-ps ripple on the eye diagram.

Bit-error rate, k_e, measurements were performed at the five channel distances and the results are shown in Fig. 4. It is seen that more errors were captured for increasing data-rate and channel distance, as expected. It is especially noted that error-free transmission of a 10 Gbit data-sequence was achieved at data-rates up to 10 Gb/s over a 0.3-m chan-nel. This corresponds to a normalised transceiver energy-efficiency of 1 nJ/bit/m. In a WPAN implementation, bit-error rates up to 10^{-5} or even 10^{-3} may be viable. This is visualised by increased levels of shading in Fig. 4 and Fig. 5. For these limit bit-error rates, data-rates up to 10 or 15-Gb/s, respectively, qualify as viable at 1.5 m link distance and the corresponding input referred sensitivity is −30.9 dBm. Interestingly, the bit-error rate results are seen to degrade significantly as the data-rate is increased from 10 to 12.5 Gb/s. We attribute this to the closing of the symbol eye, as seen in Fig. 3, where the symbol transition-time was identified to be 100-ps. Further, pattern synchronisation at 20 Gb/s was

only possible over link distances up to 1.2 m. To convey additional details of the link properties at 10-Gb/s data-rate, the measured eye margins, as indicated in Fig. 3(a), are shown in Fig. 5 for different limit values of bit-error rate. The phase margin, Δ_{UI}, has an approximately linear dependence on the channel distance, while the corresponding trend for the threshold margin, Δ_{V}, is seen to decay exponentially. This is attributed to the combination of link pathloss and detector non-linearity.

V. DISCUSSION

The III-V system presented in this paper has unique functionality, as compared to silicon implementations, what provides performance benefits. On the transmitter side, the RTD-MOSFET wavelet generator provides coherency and frequency scalability [9]. This allows for system design in the millimetre-wave spectrum, and scaling towards terahertz frequencies where spread-spectrum signals may be used in unlicensed bands [22]. On the receiving side, the zero-bias property of the detector allows for energy-efficient down-conversion. As an alternative to the utilised off-the-shelf power-hungry amplifier and bulky antennas, a more efficient and integrated amplifier and antenna implementation in III-V or silicon would improve the performance of the receiver. Receiver and antenna options can be found in the literature, as summarised below and benchmarked in Table I.

The here presented transceiver system, i.e. III-V wavelet generator, to amplifier, and zero-bias detector must be benchmarked against other implementations for short-range high-speed communication. For this purpose, state-of-the-art wireless multi-Gb/s transceivers have been summarised in Table I. The selection include all systems, to the best of our knowledge, which have demonstrated data-rates exceeding 3 Gb/s for omni-distances above 10 mm at disclosed PRBS lengths and limit bit-error rates. An exception on the disclosure of the PRBS length was made for the 4-QPSK and 16-QAM transceivers [12], [15], allowing a comparison across additional modulation formats. Certain transceiver implementations of significance did not fit within the selection criteria for this benchmark comparison. For example, transceiver chipsets implemented for 60 GHz communication within IEEE 802.11a have been shown [27], [28], [30]. Another, more recent, front-end implementation targets the IEEE 802.15.3c specification [31]. Spread-spectrum implementations such as 60-GHz OOK front-ends have also been shown [23]. Implementations with antennas in-package typically achieve data-rates of a few Gb/s [24], [25].

From Table I, it is clear that OOK and 2-ASK transceivers have lower power-dissipation than their multi-Gb/s QPSK or QAM counterparts. The most energy-efficient transceiver has achieved OOK communication at only 6.31 pJ/bit [11]. However, the RTD-MOSFET transmitter presented here has demonstrated the highest OOK data-rate and the best transmitter energy-efficiency in the comparison. The output power is competitive and the link distance is high, as compared to most other implementations. However, the link distances for

all systems in Table I are seen to scale in proportion to the gain of the utilised antennas. The best omni-distance, i.e. intrinsic front-end distance without antenna gain, is achieved by the 16-QAM system using low-gain in-package antennas [12]. The 16-QAM implementation also has the best sensitivity, and achieves the highest data-rate. A general, and intuitive, observation is that the best performance in relation to invested energy, measured as a minimum in omni-transceiver energy-efficiency, is found for combinations of low power dissipation, high output power, and low sensitivity [11]–[13].

VI. CONCLUSION

Wireless OOK communication at up to, unprecedented, 20 Gb/s serial data-rates have been demonstrated. The utilised III-V transmitter front-end has high energy-efficiency and long link distances were achieved, as compared to state-of-the-art integrated multi-Gb/s transceivers. Viable performance was measured over channel distances up to 1.5 m at data-rates of 10 and 15 Gb/s for bit-error rate $k_{\mathrm{e}} < 10^{-5}$ and 10^{-3}, respectively. The corresponding transmitter energy efficiencies are 2.17 and 1.55 pJ/bit. At 10 Gb/s data-rate, error-free transfer of 10 Gbit data in a 31-PRBS was possible over a 0.3 m link. The normalised transceiver energy-efficiency was 131 pJ/bit/m at 15 Gb/s data-rate over a 1.5 m line-of-sight channel; dominated to more than 99% by the receiver amplifier. The transceiver omni-distance was 15 mm, and the corresponding omni-transceiver energy-efficiency was hence 13.1 pJ/bit/mm. In the design of future spread-spectrum systems, III-V components allow for unique options in the transceiver architecture, regarding coherent signal generation, millimetre-wave frequency scaling, and energy-efficiency. This will improve the performance of portable, battery-powered, high-rate, and compact wireless links for short-range computation and WPAN applications.

REFERENCES

[1] P. Smulders, "The road to 100 Gb/s wireless and beyond: Basic issues and key directions," *IEEE Commun. Mag.*, vol. 51, no. 12, pp. 86–91, Dec. 2013.

[2] H. Bissessur *et al.*, "3.2 Tbit/s (80 × 40 Gbit/s) phase-shaped binary transmission over 3 × 100 km with 0.8 bit/s/Hz efficiency," *Electron. Lett.*, vol. 38, no. 8, pp. 377–379, Apr. 2002.

[3] S. Rangan, T. S. Rappaport, and E. Erkip, "Millimeter-wave cellular wireless networks: Potentials and challenges," *Proc. IEEE*, vol. 102, no. 3, pp. 366–385, Mar. 2014.

[4] T. Baykas *et al.*, "IEEE 802.15.3c: The first IEEE wireless standard for data rates over 1 Gb/s," *IEEE Commun. Mag.*, vol. 49, no. 7, pp. 114–121, Jul. 2011.

[5] K. Kawasaki *et al.*, "A millimeter-wave intra-connect solution," *IEEE J. Solid-State Circuits*, vol. 45, no. 12, pp. 2655–2666, Dec. 2010.

[6] Y. Tanaka *et al.*, "A versatile multi-modality serial link," in *IEEE Int. Conf. Solid-State Circuits Tech. Dig. Papers (ISSCC)*, Feb. 2012, pp. 332–334.

Paper IV: © 2014 IEEE

[7] R. C. Daniels, J. N. Murdock, T. S. Rappaport, and R. W. Heath, "60 GHz wireless: Up close and personal," *IEEE Microw. Mag.*, vol. 11, no. 7, pp. 44–50, Dec. 2010.

[8] C. Park and T. S. Rappaport, "Short-range wireless communications for next-generation networks: UWB, 60 GHz millimeter-wave WPAN, and ZigBee," *IEEE Trans. Wireless Commun.*, vol. 14, no. 4, pp. 70–78, Aug. 2007.

[9] M. Egard, M. Ärlelid, L. Ohlsson, B. M. Borg, E. Lind, and L.-E. Wernersson, "In$_{0.53}$Ga$_{0.47}$As RTD–MOSFET millimeter-wave wavelet generator," *IEEE Electron Device Lett.*, vol. 33, no. 7, pp. 970–972, Jul. 2012.

[10] K. Katayama, M. Motoyoshi, K. Takano, L. C. Yang, and M. Fujishima, "209 mW 11 Gbps 130 GHz CMOS transceiver for indoor wireless communication," in *Proc. IEEE Asian Solid-State Circuits Conf. (A-SSCC)*, Nov. 2013, pp. 409–412.

[11] C. W. Byeon, C. H. Yoon, and C. S. Park, "A 67-mW 10.7-Gb/s 60-GHz OOK CMOS transceiver for short-range wireless communications," *IEEE Trans. Microw. Theory Techn.*, vol. 61, no. 9, pp. 3391–3401, Sep. 2013.

[12] H. Asada *et al.*, "A 60GHz 16Gb/s 16QAM low-power direct-conversion transceiver using capacitive cross-coupling neutralization in 65 nm CMOS," in *Proc. IEEE Asian Solid State Circuits Conf. (A-SSCC)*, Nov. 2011, pp. 373–376.

[13] F. Zhu *et al.*, "A low-power low-cost 45-GHz OOK transceiver system in 90-nm CMOS for multi-Gb/s transmission," *IEEE Trans. Microw. Theory Techn.*, vol. 62, no. 9, pp. 2105–2117, Sep. 2014.

[14] T. S. Rappaport, J. N. Murdock, and F. Gutierrez, "State of the art in 60-GHz integrated circuits and systems for wireless communications," *Proc. IEEE*, vol. 99, no. 8, pp. 1390–1436, Aug. 2011.

[15] K. Okada *et al.*, "A 60-GHz 16QAM/8PSK/QPSK/BPSK direct-conversion transceiver for IEEE802.15.3c," *IEEE J. Solid-State Circuits*, vol. 46, no. 12, pp. 2988–3004, Dec. 2011.

[16] A. Arbabian, S. Callender, S. Kang, B. Afshar, J.-C. Chien, and A. M. Niknejad, "A 90 GHz hybrid switching pulsed-transmitter for medical imaging," *IEEE J. Solid-State Circuits*, vol. 45, no. 12, pp. 2667–2681, Dec. 2010.

[17] H. Riel, L.-E. Wernersson, M. Hong, and J. A. del Alamo, "III-V compound semiconductor transistors—From planar to nanowire structures," *MRS Bull.*, vol. 39, no. 8, pp. 668–677, Aug. 2014.

[18] H. Kanaya, H. Shibayama, S. Suzuki, and M. Asada, "Fundamental oscillation up to 1.31 THz in thin-well resonant tunneling diodes," in *Proc. Int. Conf. Indium Phosph. Rel. Mater. (IPRM)*, Aug. 2012, pp. 106–109.

[19] N. Su, R. Rajavel, P. Deelman, J. N. Schulman, and P. Fay, "Sb-heterostructure millimeter-wave detectors with reduced capacitance and noise equivalent power," *IEEE Electron Device Lett.*, vol. 29, no. 6, pp. 536–539, Jun. 2008.

[20] M. Egard, M. Ärlelid, L. Ohlsson, E. Lind, and L.-E. Wernersson, "Impulse-based 4 Gbit/s radio link at 60 GHz," *Electron. Lett.*, vol. 47, no. 7, pp. 467–468, Mar. 2011.

[21] L. Ohlsson, T. Bryllert, D. Sjöberg, and L.-E. Wernersson, "Monolithically-integrated millimetre-wave wavelet transmitter with on-chip antenna," *IEEE Microw. Wireless Compon. Lett.*, vol. 24, no. 9, pp. 625–627, Sep. 2014.

[22] H.-J. Song and T. Nagatsuma, "Present and future of terahertz communications," *IEEE Trans. Terahertz Sci. Technol.*, vol. 1, no. 1, pp. 256–263, Sep. 2011.

[23] E. Juntunen *et al.*, "A 60-GHz 38-pJ/bit 3.5-Gb/s 90-nm CMOS OOK digital radio," *IEEE Trans. Microw. Theory Techn.*, vol. 58, no. 2, pp. 348–355, Feb. 2010.

[24] J. Lee, Y. Chen, and Y. Huang, "A low-power low-cost fully-integrated 60-GHz transceiver system with OOK modulation and on-board antenna assembly," *IEEE J. Solid-State Circuits*, vol. 45, no. 2, pp. 264–275, Feb. 2010.

[25] A. Siligaris *et al.*, "A low power 60-GHz 2.2-Gbps UWB transceiver with integrated antennas for short range communications," in *Proc. IEEE Radio Freq. Integr. Circuits Symp. (RFIC)*, Jun. 2013, pp. 297–300.

[26] M. Fujishima, M. Motoyoshi, K. Katayama, K. Takano, N. Ono, and R. Fujimoto, "98 mW 10 Gbps wireless transceiver chipset with D-band CMOS circuits," *IEEE J. Solid-State Circuits*, vol. 48, no. 10, pp. 2273–2284, Oct. 2013.

[27] A. Tomkins, R. A. Aroca, T. Yamamoto, S. T. Nicolson, Y. Doi, and S. P. Voinigescu, "A zero-IF 60 GHz 65 nm CMOS transceiver with direct BPSK modulation demonstrating up to 6 Gb/s data rates over a 2 m wireless link," *IEEE J. Solid-State Circuits*, vol. 44, no. 8, pp. 2085–2099, Aug. 2009.

[28] C. Marcu *et al.*, "A 90 nm CMOS low-power 60 GHz transceiver with integrated baseband circuitry," *IEEE J. Solid-State Circuits*, vol. 44, no. 12, pp. 3434–3447, Dec. 2009.

[29] I. Sarkas *et al.*, "An 18-Gb/s, direct QPSK modulation SiGe BiCMOS transceiver for last mile links in the 70–80 GHz band," *IEEE J. Solid-State Circuits*, vol. 45, no. 10, pp. 1968–1980, Oct. 2010.

[30] S. K. Reynolds *et al.*, "A silicon 60-GHz receiver and transmitter chipset for broadband communications," *IEEE J. Solid-State Circuits*, vol. 41, no. 12, pp. 2820–2831, Dec. 2006.

[31] A. Siligaris *et al.*, "A 65 nm CMOS fully integrated transceiver module for 60 GHz wireless HD applications," in *Proc. IEEE Int. Conf. Solid-State Circuits Tech. Dig. Papers (ISSCC)*, Feb. 2011, pp. 162–163.

LARS OHLSSON received the M.Sc. degree in engineering nanoscience from Lund University, Lund, Sweden, in 2010, where he is currently pursuing Ph.D. degree with the Department of Electrical and Information Technology.

He performs circuit design and develops technology for integrated antennas and millimeter-wave pulse generators. He further explores pulse-based communication and time-domain characterization. His research interests include integrated antennas, pulse generator circuits, device characterization, antenna codesign, and millimeter-wave pulse-based systems.

LARS-ERIK WERNERSSON received the M.Sc. degree in engineering physics and the Ph.D. degree in solid-state physics from Lund University, Lund, Sweden, in 1993 and 1998, respectively.

He has been a Professor of Nanoelectronics with Lund University since 2005, and was a Visiting Associate Professor with the University of Notre Dame, Notre Dame, IN, USA, in 2002 and 2003. His main research interests include design and fabrication of nanowire- and tunneling-based nanoelectronic devices and circuits with applications in low-power electronics and wireless communication. He has authored or co-authored over 120 scientific papers in this area.

Dr. Wernersson has been awarded two individual career grants from the Swedish Foundation for Strategic Research.

• • •

Paper V

Paper V

Reproduced, with permission, from:

M. Egard, L. Ohlsson, M. Ärlelid, K.-M. Persson, B. M. Borg, F. Lenrick, R. Wallenberg, E. Lind, and L.-E. Wernersson, "High-Frequency Performance of Self-Aligned Gate-Last Surface Channel In$_{0.53}$Ga$_{0.47}$As MOSFET," *IEEE Electron Device Lett.*, vol. 33, no. 3, pp. 369–371, Mar. 2012.

High-Frequency Performance of Self-Aligned Gate-Last Surface Channel In$_{0.53}$Ga$_{0.47}$As MOSFET

Mikael Egard, Lars Ohlsson, Mats Ärlelid, Karl-Magnus Persson, B. Mattias Borg, Filip Lenrick, Reine Wallenberg, Erik Lind, and Lars-Erik Wernersson

Abstract—We have developed a self-aligned $L_g = 55$ nm In$_{0.53}$Ga$_{0.47}$As MOSFET incorporating metal–organic chemical vapor deposition regrown n^{++} In$_{0.6}$Ga$_{0.4}$As source and drain regions, which enables a record low on-resistance of 199 $\Omega\mu$m. The regrowth process includes an InP support layer, which is later removed selectively to the n^{++} contact layer. This process forms a high-frequency compatible device using a low-complexity fabrication scheme. We report on high-frequency measurements showing $f_{\max}$ of 292 GHz and f_t of 244 GHz. These results are accompanied by modeling of the device, which accounts for the frequency response of gate oxide border traps and impact ionization phenomenon found in narrow band gap FETs. The device also shows a high drive current of 2.0 mA/μm and a high extrinsic transconductance of 1.9 mS/μm. These excellent properties are attributed to the use of a gate-last process, which does not include high temperature or dry-etch processes.

Index Terms—Gate-last, InGaAs, metal–organic chemical vapor deposition (MOCVD) regrowth, MOSFET, self-aligned, surface channel.

I. INTRODUCTION

FIELD-EFFECT transistors utilizing the high mobility and high source injection velocities of In$_{1-x}$Ga$_x$As channel material are investigated and developed for both very large scale integration and RF applications. State-of-the-art HEMT [1] and buried channel MOSFETs [2] have shown performance superior to surface channel devices [3], [4], which are mainly limited by the absence of a high quality In$_{1-x}$Ga$_x$As MOS interface. This paper address this challenge by investigating a gate-last surface channel process, which does not include high-temperature annealing, or dry-etch processes after the deposition of the gate dielectric. A second big challenge in the design and fabrication of In$_{1-x}$Ga$_x$As FETs is the ac-
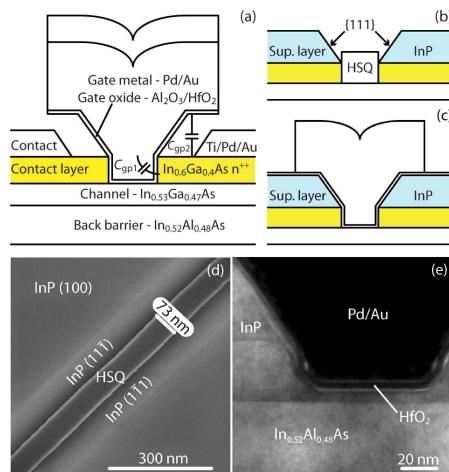
Fig. 1. Schematic cross section of (a) the completed device, (b) after MOCVD regrowth, and (c) after deposition of gate metal. (d) Shows a topview SEM image corresponding to Fig. 1(b), and (e) shows a cross-section TEM image corresponding to Fig. 1(c).

cess resistance, R_{access}. Scaling scenarios target a R_{access} of 145 $\Omega\mu$m at the 15-nm node with a contact length of 10 nm [5]. The fabrication scheme reported in this paper has been developed to address this challenge, using metal–organic chemical vapor deposition (MOCVD) to form a self-aligned device without any heterostructure barriers in the access regions, which results in low R_{access}.

The fabricated $L_g = 55$ nm devices shows excellent performance with a high extrinsic transconductance $g_{\text{m,ext.}} = 1.9$ mS/μm and a low on-resistance (R_{on}) of 199 $\Omega\mu$m. We furthermore report extrapolated $f_{\max}$ of 292 GHz and f_t of 244 GHz.

II. FABRICATION

A schematic illustration of the device is shown in Fig. 1(a). The devices are fabricated from an InP (100) substrate, on which the following structure is grown by means of molecular-beam epitaxy (MBE): a 190 nm In$_{0.52}$Al$_{0.48}$As($N_A = 5 \times 10^{16}$ cm^{-3}) buffer layer, a 5 nm In$_{0.52}$Al$_{0.48}$As($N_D = 8 \times 10^{16}$ cm^{-3}) layer, a 1 nm In$_{0.52}$Al$_{0.48}$As (N.I.D.) spacer layer, and a 10 nm In$_{0.53}$Ga$_{0.47}$As (N.I.D.) channel layer.

Hydrogen silsesquioxane (HSQ) resist is spun on the sample and baked at 80 °C for 2 min. Electron-beam exposure and development in Tetramethylammonium hydroxide (TMAH) 25% defines 130 nm high SiO_2-like dummy gates, which are used as a hard mask for selective epitaxial regrowth. The samples are treated in NH_4OH before they are loaded into a MOCVD reactor where they are annealed for 10 min at 550 °C. This is followed by the growth of 30 nm $In_{0.6}Ga_{0.4}As$ ($N_D = 6 \times 10^{19}$ cm^{-3}, Sn doped) and 90 nm of InP, as illustrated in the schematic cross section in Fig. 1(b) and in the top view SEM image in Fig. 1(d). The layers are grown at a high V/III ratio resulting in (111)B terminated slanting surfaces adjacent to the HSQ hard mask. The dummy mask is removed in a buffered oxide etch (BOE), after which the samples present trenches down to the $In_{0.53}Ga_{0.47}As$ channel. The samples are then treated in $(NH_4)_2S$ 10% for 20 min before they are loaded into an Atomic layer deposition (ALD) system. TMA and H_2O are used as precursors when depositing 0.5 nm of Al_2O_3 at 300 °C. This is followed by the deposition of 6.5 nm of HfO_2 at 100 °C using TDMAHf and H_2O as precursors. Fig. 1(c) shows a schematic cross section of the device after the gate metal, consisting of 10 nm Pd and 290 nm Au, has been deposited, and the corresponding TEM image is shown in Fig. 1(e). The gate oxide is then removed outside the gate metal in a BOE. A T-gate is formed by selectively etching the InP support layer in $HCl:H_2O$. Source and drain Ti/Pd/Au contacts are deposited in a self-aligned manner by thermal evaporation. Further details regarding the processing may be found in [6] and [7].

III. DC Results

The dc output characteristics of a $L_g = 55$ nm device are shown in Fig. 2(a). The device shows a drain current of 2.0 mA/μm and $R_{on} = 199$ $\Omega\mu$m at $V_{GS} = 1.8$ V. An extrinsic transconductance ($g_{m,ext.}$) of 1.9 mS/μm is obtained at $V_{DS} = 1$ V and $V_{GS} = 0.5$ V. The transfer characteristics of a $L_g = 140$ nm and a $L_g = 55$ nm device are shown in Fig. 2(b). The $L_g = 140$ nm device shows enhancement mode operation at $V_{DS} = 0.5$ V, with $V_T = 0.06$ V (extracted at 1 μA/μm), a subthreshold swing (SS) of 100 mV/decade, $I_{on}/I_{off} = 2.4 \cdot 10^3$ (extracted at 1/3 V_{DS} below V_T and 2/3 V_{DS} above V_T), $g_{m,ext.} = 1.05$ mS/μm, and a drain-induced barrier lowering of 110 mV/V. The SS is as low as 79 mV/decade at $V_{DS} = 0.05$ V. The good properties of the gate-last MOS interface is confirmed by CV measurements, which shows a small dispersion in accumulation of 3.7%/decade and an interface trap density (D_{it}) of 4–8 $\cdot 10^{12}$ eV^{-1}cm^{-2} in the upper part of the band gap [6]. This is similar to results from experiments on reference diodes [8], indicating that the gate-last process does not add significant D_{it} due to process induced damage. Analyzing the $L_g = 55$ nm device for $V_{DS} = 0.5$ V operation gives $g_{m,ext.} = 1.5$ mS/μm, $V_T = -0.3$ V, and $SS = 187$ mV/decade, which is limited by short channel effects and impact ionization.

From measurements of R_{on} for the $L_g = 55$ nm and $L_g = 140$ nm($R_{on} = 265$ $\Omega\mu$m) [7] device, it is possible to calculate $R_{access} = 156$ $\Omega\mu$m. The length of the source and drain contacts is longer than the transfer length.
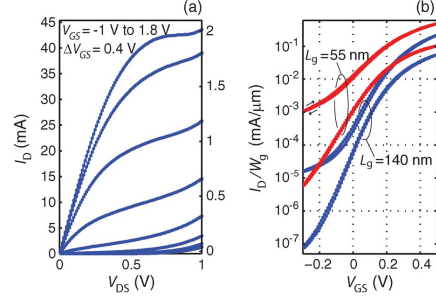
Fig. 2. (a) Output characteristics of a $L_g = 55$ nm device. (b) Transfer characteristics of a $L_g = 140$ nm and a $L_g = 55$ nm device at $V_{DS} = 0.5$ V and $V_{DS} = 0.05$ V. Both devices have a gate width (W_g) of 21.6 μm and the gate leakage current is below 10 pA/μm.
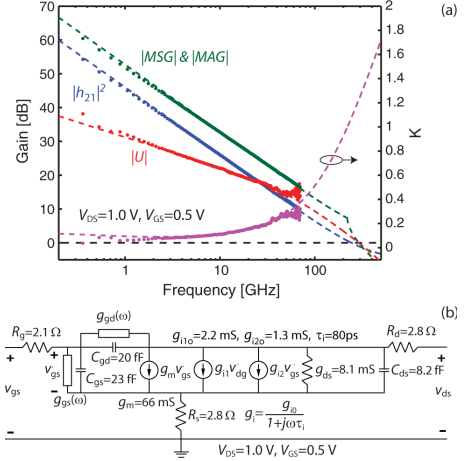
Fig. 3. (a) Measured and modeled (dashed traces) RF gain and stability factor K of a $L_g = 55$ nm, $W_g = 21.8$ μm device. (b) Small signal model corresponding to the dashed traces in (a).

IV. RF Measurements

The S-parameters of a $L_g = 55$ nm device were measured from 360 MHz to 70 GHz using on-wafer probing and a port power of −27 dBm. A two-port load-reflect-reflect-match calibration was performed using a Cascade Microtech 101–1908 impedance standard substrate. The device under test was de-embedded using on-chip open and short pad structures. The measured current gain (h_{21}), unilateral power gain (U), and maximum stable/maximum available gain (MSG/MAG) are shown in Fig. 3(a). Fig. 3(b) shows a small signal model corresponding to the dashed traces in Fig. 3(a). The small signal model was extracted using an analytical approach, where the impact ionization phenomenon seen at lower frequencies ($f < 3$ GHz) is modeled by two voltage-dependent current sources, taking into account the dependence on the gate-drain electric field and the amount of carriers [9].
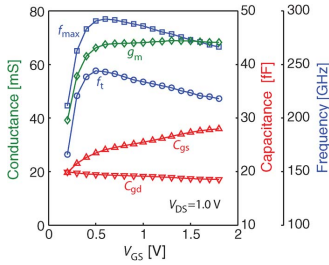
Fig. 4. $f_{\max}$, f_t, C_{gs}, C_{gd}, and g_m all extracted from RF measurements of a $L_g = 55$ nm, $W_g = 21.6$ μm device.

In Fig. 3(a), it is seen that the measured U falls off at roughly 10 dB/dec, which is less than the expected 20 dB/dec for a single pole system. This behavior is only observed for U and not MSG/MAG or h_{21}. This is explained by the fact that U heavily depends on the real part of y_{11} and y_{12}, which in a MOSFET is dominated by the conductive part of the gate oxide admittance. In order to accurately model U of a III–V MOSFET, it is necessary to take the frequency response of the oxide border traps into account. One way to do this is to use a distributed trap model, as presented in [10]. This approach is implemented in the small signal model, in Fig. 3(b), as two frequency-dependent conductances $g_{gs}(\omega)$, and $g_{gd}(\omega)$. Their values are calculated using the model in [10] with a constant border trap density of $9 \cdot 10^{19}$ cm^{-3} eV^{-1}. This may be one explanation to the roughly 10 dB/dec roll-off of U. The small variation in the gate capacitance associated with the distributed trap model is not included here. The model in Fig. 3(b) shows good agreement over the entire frequency interval. The absolute square of the relative error between the measured and extracted y-parameters is below 0.5% at all measured bias points.

Fig. 4 shows the bias dependence of parameters extracted from the S-parameter measurement. A peak $f_{\max}$ of 292 GHz, and a peak f_t of 244 GHz are obtained at $V_{DS} = 1$ V. Extrapolating with 20 dB/dec from the measured data gives $f_t = 220$ GHz. An intrinsic transconductance g_m of 3.0 mS/μm is obtained at $V_{GS} = 0.5$ V. Using the values of R_s, R_d, and g_{ds} extracted from the S-parameter measurement gives $g_{m,\text{ext.}} = 2.2$ mS/μm, and taking the effect of impact ionization at $\omega = 0$ into account gives $g_{m,\text{ext.}} = 2.1$ mS/μm, which agrees well with the value obtained from dc measurements.

The dc measurements presented in Fig. 2 show a decrease in $g_{m,\text{ext.}}$ as the gate voltage is increased beyond $V_{GS} = 0.5$ V, this is not the case for the intrinsic g_m in Fig. 4, which is extracted from RF measurements. The discrepancy may be attributed to the high density of border traps distributed throughout the oxide, which gives a very wideband frequency response as the time constant of the charge exchange between the border traps and the semiconductor depends exponentially on the distance between them [10].

The extracted gate-source C_{gs} and gate-drain C_{gd} capacitances are mainly set by parasitic coupling. The two main contributions are from the overlap between the contact layer and the gate metal C_{gp1}, and between the T-gate and the contact layer C_{gp2}, as shown in Fig. 1(a). Electrostatic capacitance modeling in the finite-element solver COMSOL gives $C_{gp1} = 17$ fF and $C_{gp2} = 7.2$ fF. These should be compared to the measured value of $C_{gd} = 19$ fF, which in the saturation regime mainly consists of the parasitic contribution.

Initial studies of the low-frequency noise give a normalized current noise spectral density, S_I/I_{DS}^2 below 10^{-8} Hz^{-1} at 10 Hz, $V_{DS} = 50$ mV, and $V_{GS} > 0.5$ V. The measurements indicate a $1/I_{DS}$ dependence, suggesting that the noise is dominated by mobility fluctuations [11].

V. CONCLUSION

We have reported on an In$_{0.53}$Ga$_{0.47}$As surface channel MOSFET which shows an extrinsic transconductance of 1.9 mS/μm, on-resistance of 199 $\Omega\mu$m, $f_{\max}$ of 292 GHz, and f_t of 244 GHz. The excellent performance is attributed to the novel MOCVD regrowth self-aligned gate-last fabrication process described in this letter.

REFERENCES

[1] T.-W. Kim, D.-H. Kim, and J. del Alamo, "60 nm self-aligned-gate InGaAs HEMTs with record high-frequency characteristics," in *Proc. IEEE IEDM*, Dec. 2010, pp. 30.7.1–30.7.4.

[2] M. Radosavljevic, B. Chu-Kung, S. Corcoran, G. Dewey, M. Hudait, J. Fastenau, J. Kavalieros, W. Liu, D. Lubyshev, M. Metz, K. Millard, N. Mukherjee, W. Rachmady, U. Shah, and R. Chau, "Advanced high-k gate dielectric for high-performance short-channel In$_{0.7}$Ga$_{0.3}$As quantum well field effect transistors on silicon substrate for low power logic applications," in *Proc. IEEE IEDM*, Dec. 2009, pp. 1–4.

[3] H. Ko, K. Takei, R. Kapadia, S. Chuang, H. Fang, P. W. Leu, K. Ganapathi, H. S. Plis, E. Kim, S.-Y. Chen, M. Madsen, A. C. Ford, Y.-L. Chueh, S. Krishna, S. Salahuddin, and A. Javey, "Ultrathin compound semiconductor on insulator layers for high-performance nanoscale transistors," *Nature*, vol. 468, no. 7321, pp. 286–289, Nov. 2010.

[4] Y. Wu, R. Wang, T. Shen, J. Gu, and P. Ye, "First experimental demonstration of 100 nm inversion-mode ingaas finfet through damage-free sidewall etching," in *Proc. IEEE IEDM*, Dec. 2009, pp. 1–4.

[5] International Technology Roadmap for Semiconductors. [Online]. Available: http://public.itrs.net

[6] M. Egard, L. Ohlsson, B. M. Borg, F. Lenrick, R. Wallenberg, L.-E. Wernersson, and E. Lind, "High transconductance self-aligned gate-last surface channel In$_{0.53}$Ga$_{0.47}$As MOSFET," in *Proc. IEEE IEDM*, Dec. 2011, pp. 13.2.1–13.2.4.

[7] M. Egard, L. Ohlsson, B. M. Borg, L.-E. Wernersson, and E. Lind, "Self-aligned gate-last surface channel In$_{0.53}$Ga$_{0.47}$As mosfet with selectively regrown source and drain contact layers," in *Proc. 69th Annu. DRC*, Jun. 2011, pp. 1–2.

[8] E. O'Connor, B. Brennan, V. Djara, K. Cherkaoui, S. Monaghan, S. B. Newcomb, R. Contreras, M. Milojevic, G. Hughes, M. E. Pemble, R. M. Wallace, and P. K. Hurley, "A systematic study of (NH4)2S passivation (22%, 10%, 5%, or 1%) on the interface properties of the Al$_2$O$_3$/In$_{0.53}$Ga$_{0.47}$As/InP system for n-type and p-type In$_{0.53}$Ga$_{0.47}$As epitaxial layers," *J. Appl. Phys.*, vol. 109, no. 2, p. 024101, 2011.

[9] S. Johansson, M. Egard, S. G. Ghalamestani, B. M. Borg, M. Berg, L.-E. Wernersson, and E. Lind, "RF characterization of vertical InAs nanowire wrap-gate transistors integrated on Si substrates," *IEEE Trans. Microw. Theory Tech.*, vol. 59, no. 10, pp. 2733–2738, Oct. 2011.

[10] Y. Yuan, L. Wang, B. Yu, B. Shin, J. Ahn, P. McIntyre, M. Rodwell, and Y. Taur, "A distributed model for border traps in MOS devices," *IEEE Electron Device Lett.*, vol. 32, no. 4, pp. 485–487, Apr. 2011.

[11] M. von Haartman and M. Östling, *Low-Frequency Noise in Advanced MOS Devices*. New York: Springer-Verlag, 2007.

Paper VI

Paper VI

Reproduced, with permission, from:

M. Egard, M. Ärlelid, L. Ohlsson, B. M. Borg, E. Lind, and L.-E. Wernersson, "In$_{0.53}$Ga$_{0.47}$As RTD-MOSFET Millimeter-Wave Wavelet Generator," *IEEE Electron Device Lett.*, vol. 33, no. 7, pp. 970–972, Jul. 2012.

In$_{0.53}$Ga$_{0.47}$As RTD–MOSFET Millimeter-Wave Wavelet Generator

Mikael Egard, Mats Ärlelid, Lars Ohlsson, B. Mattias Borg, Erik Lind, and Lars-Erik Wernersson

***Abstract*—We report on the fabrication of a self-aligned re-grown In$_{0.53}$Ga$_{0.47}$As metal–oxide–semiconductor field-effect transistor (MOSFET) and a resonant tunneling diode (RTD). The performance of these devices is demonstrated by integrating them in parallel with an inductive coplanar waveguide stub to form a highly energy-efficient 70-GHz wavelet generator. The fast switching and low on-resistance of the MOSFET make it possible to kick-start and rapidly quench this RTD-driven oscillator circuit, which produces 41-ps-short wavelets at 15 Gpulses/s, a peak output power of 7 dBm, and an energy consumption of 1.9 pJ/pulse.**

***Index Terms*—Impulse radio, InGaAs, metal–organic chemical vapor deposition regrowth, metal–oxide–semiconductor field-effect transistor (MOSFET), pulse generator, resonant tunneling diode (RTD), ultrawideband, wavelet generator.**

I. Introduction

METAL–OXIDE–semiconductor field-effect transistors (MOSFETs) based on high-mobility indium-rich compounds are considered for future high-performance circuit applications [1]. The use of III–V materials gives not only the possibility to design advanced transistors but also the opportunity to gain additional circuit functionality by incorporating heterostructure engineered devices. An example of such a heterostructure device is the resonant tunneling diode (RTD), which previously has been integrated with various transistor technologies to improve circuit performance in both digital and analog applications [2]–[5].

This letter presents the first demonstration of an In$_{0.53}$Ga$_{0.47}$As RTD–MOSFET millimeter-wave (mmW) circuit. The negative differential conductance (NDC) of the RTD is used to drive an *LC*-tank resonance circuit. The In$_{0.53}$Ga$_{0.47}$As MOSFET is integrated in series with the RTD, and by switching the MOSFET between a high and a low output state, it is possible to generate short high-frequency pulses, also known as wavelets. A key advantage of this configuration is the low on-resistance and low gate leakage current of the MOSFET, which reduces the power consumption.

Wavelet generators are considered for use in impulse-based mmW transmitters for various short-range ultrawideband applications, such as localization, radar, imaging, spectroscopy, and high-data-rate communication [6]–[8]. The RTD–MOSFET wavelet generator presented in this letter demonstrates excellent performance in terms of pulselength (t_p) and energy consumption per pulse, when compared to state-of-the-art wavelet generators [9]–[11].

II. Fabrication

The fabrication of the RTD and the MOSFET is performed in parallel. The molecular-beam-epitaxy-grown double-barrier heterostructure (DBH) features 1.4-nm-thick AlAs barriers and a 3.8-nm-thick In$_{0.53}$Ga$_{0.47}$As quantum well, including a 2.0-nm-thick InAs notch. Undoped spacers of 3 nm in thickness are present at both sides of the DBH. The doping on the emitter side is 4×10^{18} cm^{-3}, and a 100-nm $N_D = 2 \times 10^{17}$ cm^{-3} space charge region is included on the collector side. The measured peak current density is 122 kA/cm^2, and the peak-to-valley current ratio is 12. The first step is to isolate an outer RTD mesa, shown in Fig. 1(a). This is done by selective wet etching of In$_{0.53}$Ga$_{0.47}$As and the InP etch stop layers using H$_3$PO$_4$: H$_2$O$_2$ and HCl:H$_3$PO$_4$, respectively. The InP etch stop layers are included in the epitaxial design to allow for the formation of a bottom RTD contact. Hydrogen silsesquioxane (HSQ) dummy gates are formed directly on top of the channel, by electron-beam lithography. A 30-nm-thick highly Sn-doped ($N_D = 6 \times 10^{19}$ cm^{-3}) In$_{0.53}$Ga$_{0.47}$As contact layer and a 90-nm-thick InP support layer are regrown using metal–organic chemical vapor deposition at 500 °C [12]. Fig. 1(b) shows the sample after removal of the HSQ dummy gate. Pd/Au gate metal is evaporated on top of the atomic-layer-deposited Al$_2$O$_3$ (0.5 nm) and HfO$_2$ (6.5 nm) gate oxide stack. Selective wet-etch processes make it possible to form a freestanding T-gate by removing the HfO$_2$ and the InP support layer, using buffered oxide etch and HCl, respectively. Fig. 1(c) shows that the RTD collector contact is formed, by lift-off, on top of the regrown contact layer. It is then used as a mask when isolating the RTD mesa by means of wet etching. The RTD emitter contact is deposited in a self-aligned manner by tilted evaporation, at the same time as the source and drain contacts, as shown in Fig. 1(d). Measurement on reference RTDs shows that the performance of the DBH, which includes a strained InAs notch, is unaffected by the described regrowth fabrication process.

An optical image of a fabricated wavelet generator is shown in Fig. 2(a). The coplanar waveguides (CPWs) are deposited by thermal evaporation, and the 200×250 μm^2 metal–insulator–metal stabilizing capacitor (C_s) is based on an atomic-layer-deposited 15-nm-thick HfO$_2$ dielectric [13]. The
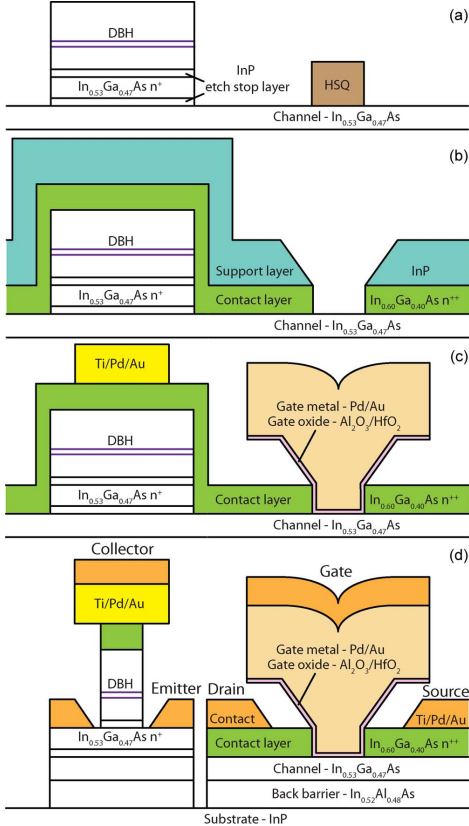
Fig. 1. Schematic cross section of the fabricated MOSFET and RTD. (a) Before regrowth, (b) after removal of the HSQ dummy gate, (c) after collector contact deposition, and (d) completed devices.
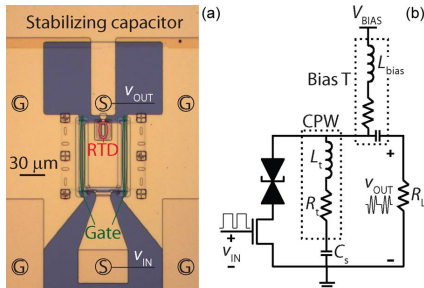

Fig. 2. (a) Optical micrograph of a fabricated wavelet generator: The input (v_{IN}) and output (v_{OUT}) are indicated by the positions of the ground–signal–ground probes. (b) Equivalent circuit of the fabricated wavelet generator. The following parameters are obtained from S-parameter characterization: $L_t = 23$ pH, $R_t = 0.2$ Ω, and $C_s = 720$ pF.
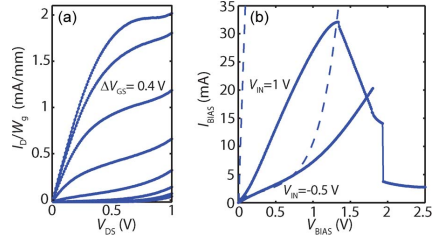
Fig. 3. (a) Output characteristics of a MOSFET with $L_g = 55$ nm and $W_g = 21.6$ μm. V_{GS} is swept from -1 to $+1.8$ V. The gate leakage current is below 10 pA/μm. (b) DC output characteristics of the wavelet generator. The dashed traces show the corresponding drain currents of the MOSFET. The dimensions of the MOSFET are $L_g = 55$ nm and $W_g = 160$ μm.

fabricated wavelet generator is represented by the equivalent circuit in Fig. 2(b). Fig. 3(a) shows the dc output characteristics of a 55-nm-gate-length (L_g) and 21.6-μm-gate-width (W_g) MOSFET. The device shows excellent performance such as high $g_{m\ ext.} = 1.9$ mS/μm at $V_{GS} = 0.5$ V and $V_{DS} = 1$ V, low $R_{on} = 199$ $\Omega \cdot \mu$m, and extrapolated f_{max} of 292 GHz and f_t of 244 GHz [12], [14].

III. WAVELET GENERATOR OPERATION

Fig. 3(b) shows the dc output characteristics of the wavelet generator; the dashed trace shows the dc output of the MOSFET. The MOSFET is operated as a variable resistor, which, at a low input voltage (V_{IN}), limits the current through the RTD and, at a high V_{IN}, acts as a short circuit. To minimize the resistive losses in the circuit, the MOSFET is implemented with $W_g = 160$ μm. This makes it possible to switch the output of the RTD–MOSFET between NDC and positive differential conductance and, hence, the output resonance circuit between an oscillating and a nonoscillating state. The center frequency of the oscillation is determined by the inductance of the CPW ($L_t = 22$ pH) and the large-signal output capacitance of the RTD, which is estimated to be 4.5 fF/μm^2. The RTD area is 2.2×12 μm^2, the series resistance of the RTD is estimated to be 4 Ω, and the minimum intrinsic RTD output conductance is -120 mS, as concluded from analytical modeling of the RTD current [2]. Fig. 4(a) and (b) shows the output signal and the input signal of the wavelet generator, respectively. The output signal is measured with an $R_L = 50$ Ω 100-GHz LeCroy coherent interleaved sampling oscilloscope, and the input signal is generated by an Agilent N4906B. The wavelet generator produces 41-ps-short wavelets with a center frequency (f_0) of 70 GHz, at a pulse-repetition frequency of 15 Gpulses/s, and a peak output power (P_{peak}) of 7 dBm. The circuit consumes 29 mW when operated at this rate, and the corresponding energy consumption per pulse (E_p) is 1.9 pJ/pulse. The length of the wavelet is evaluated at 50% of the maximum amplitude. The power consumption of the wavelet generator is limited by the OFF-state current of the MOSFET with $L_g = 55$ nm and $W_g = 160$ μm. The elevated current at high V_{DS} is attributed to impact ionization and/or band-to-band tunneling and short-channel effects [12], [14]. The focus of future work will be to further optimize the MOSFET characteristics with respect to the RTD.
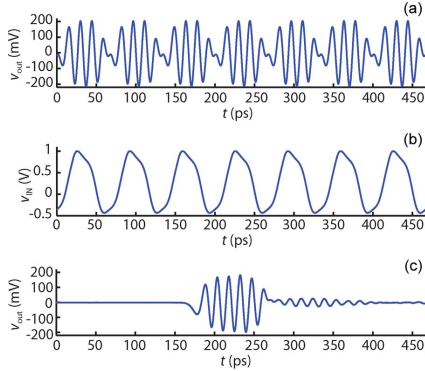
Fig. 4. (a) Measured output signal from the wavelet generator: The length of the wavelets is 41 ps, the center frequency is 70 GHz, and the peak output power is 7 dBm, which is obtained from de-embedding the measured 210-mV peak voltage amplitude by 11 dB of measurement loss. (b) Measured input signal to the wavelet generator: The pulselength is 34 ps. (c) Single wavelet: The length of the input pulse is 56 ps, and the generated wavelet is 70 ps long. The circuit is biased at 1.5 V.

TABLE I
STATE-OF-THE-ART COHERENT mmW WAVELET GENERATORS

Technology	f_0 (GHz)	t_p (ps)	P_{peak} (dBm)	E_p (pJ/pulse)	PRF (GHz)
This work	70	41	7	1.9	15
[9] GaAs GTD	60	33	-13	4.6	12.5
[10] CMOS65nm SOI	56	250	5.3	12.6	2.2
[11] CMOS65nm SOI	60	500	5	5.0	1.5

Fig. 4(c) shows a single wavelet with a 10-dBc bandwidth of 20.5 GHz. The smaller amplitude signal following the wavelet is due to reflections in the measurement setup and can be avoided by integrating the wavelet generator load on-chip. The wavelet generator is able to deliver these short bursts of mmW energy at this very high rate owing to the ultrashort start-up and decay time of the oscillator circuit [15]. The rapid start-up is controlled by the rising edge of the input signal, which switches the current through the RTD. This rapid change in current cannot be supplied by the bias inductor and is hence provided, through L_t, by C_s. This effectively determines the initial condition of the oscillation, as $v = L_t(\mathrm{d}i/\mathrm{d}t)$, and enables the generation of stable and coherent wavelets [9]. The key properties of the regrown MOSFET that enable this functionality are the fast current switching and the low on-resistance. RTDs have been previously integrated with both HFET [2], [3] and HBT [4] technologies. Considering the application presented here, HBTs are slower when switching at low output voltage, and in contrast to MOSFETs, both types of devices experience large input leakage currents when scaled for high performance. This is particularly true for HEMT devices at large gate overdrive. The regrown MOSFET also shows lower access resistance when compared to state-of-the-art HEMTs [14].

Table I presents a benchmarking of state-of-the-art coherent mmW wavelet generators reported in the literature [9]–[11]. The wavelet generator reported in this work compares favorably, particularly when a short t_p is desired, which is important

for high-data-rate signals and for high-resolution radar, imaging, and localization applications.

IV. CONCLUSION

We have demonstrated the fabrication of an $In_{0.53}Ga_{0.47}As$ RTD–MOSFET wavelet generator. The circuit operates at a rate of 15 Gpulses/s, producing 41-ps-short wavelets at an energy consumption of 1.9 pJ/pulse. The excellent performance of the wavelet generator is attributed to the low on-resistance of the self-aligned regrown MOSFET and the fact that the RTD characteristics are not deteriorated by the described fabrication process.

REFERENCES

[1] A. J. del Alamo, "Nanometre-scale electronics with III–V compound semiconductors," *Nature*, vol. 479, no. 7373, pp. 317–323, Nov. 2011.
[2] T. Broekaert, B. Brar, J. van der Wagt, A. Seabaugh, F. Morris, T. Moise, E. Beam, and G. Frazier, "A monolithic 4-bit 2-gsps resonant tunneling analog-to-digital converter," *IEEE J. Solid-State Circuits*, vol. 33, no. 9, pp. 1342–1349, Sep. 1998.
[3] K. Maezawa, H. Matsuzaki, M. Yamamoto, and T. Otsuji, "High-speed and low-power operation of a resonant tunneling logic gate mobile," *IEEE Electron Device Lett.*, vol. 19, no. 3, pp. 80–82, Mar. 1998.
[4] Y. Jeong, S. Choi, and K. Yang, "Novel antiphase-coupled RTD microwave oscillator operating at extremely low DC-power consumption," *IEEE Trans. Nanotechnol.*, vol. 9, no. 3, pp. 338–341, May 2010.
[5] A. Matiss, A. Poloczek, A. Stohr, W. Brockerhoff, W. Prost, and F.-J. Tegude, "Sub-nanosecond pulse generation using resonant tunneling diodes for impulse radio," in *Proc. IEEE ICUWB*, Sep. 2007, pp. 354–359.
[6] I. Gresham, A. Jenkins, R. Egri, C. Eswarappa, N. Kinayman, N. Jain, R. Anderson, F. Kolak, R. Wohlert, S. Bawell, J. Bennett, and J.-P. Lanteri, "Ultra-wideband radar sensors for short-range vehicular applications," *IEEE Trans. Microw. Theory Tech.*, vol. 52, no. 9, pp. 2105–2122, Sep. 2004.
[7] A. Arbabian, S. Callender, S. Kang, B. Afshar, J.-C. Chien, and A. Niknejad, "A 90 GHz hybrid switching pulsed-transmitter for medical imaging," *IEEE J. Solid-State Circuits*, vol. 45, no. 12, pp. 2667–2681, Dec. 2010.
[8] M. Ärlelid, M. Egard, L. Ohlsson, E. Lind, and L.-E. Wernersson, "Impulse-based 4 Gbit/s radio link at 60 GHz," *Electron. Lett.*, vol. 47, no. 7, pp. 467–468, Mar. 2011.
[9] M. Ärlelid, M. Egard, E. Lind, and L.-E. Wernersson, "Coherent V-band pulse generator for impulse radio BPSK," *IEEE Microw. Wireless Compon. Lett.*, vol. 20, no. 7, pp. 414–416, Jul. 2010.
[10] A. Siligaris, N. Deparis, R. Pilard, D. Gloria, C. Loyez, N. Rolland, L. Dussopt, J. Lanteri, R. Beck, and P. Vincent, "A 60 GHz UWB impulse radio transmitter with integrated antenna in CMOS 65 nm SOI technology," in *Proc. IEEE 11th Top. Meeting SiRF*, Jan. 2011, pp. 153–156.
[11] N. Deparis, A. Siligarisy, P. Vincent, and N. Rolland, "A 2 pJ/bit pulsed ILO UWB transmitter at 60 GHz in 65-nm CMOS-SOI," in *Proc. IEEE ICUWB*, Sep. 2009, pp. 113–117.
[12] M. Egard, L. Ohlsson, M. Arlelid, K.-M. Persson, B. M. Borg, F. Lenrick, R. Wallenberg, E. Lind, and L.-E. Wernersson, "High-frequency performance of self-aligned gate-last surface channel $In_{0.53}Ga_{0.47}As$ MOSFET," *IEEE Electron Device Lett.*, vol. 33, no. 3, pp. 369–371, Mar. 2012.
[13] M. Egard, M. Ärlelid, E. Lind, and L. Wernersson, "Bias stabilization of negative differential conductance oscillators operated in pulsed mode," *IEEE Trans. Microw. Theory Tech.*, vol. 59, no. 3, pp. 672–677, Mar. 2011.
[14] M. Egard, L. Ohlsson, B. M. Borg, F. Lenrick, R. Wallenberg, L.-E. Wernersson, and E. Lind, "High transconductance self-aligned gate-last surface channel $In_{0.53}Ga_{0.47}As$ MOSFET," in *Proc. IEDM*, Dec. 2011, pp. 13.2.1–13.2.4.
[15] M. Egard, M. Ärlelid, E. Lind, G. Astromskas, and L.-E. Wernersson, "20 GHz wavelet generator using a gated tunnel diode," *IEEE Microw. Wireless Compon. Lett.*, vol. 19, no. 6, pp. 386–388, Jun. 2009.

Paper VII

Paper VII

Reproduced, in printed version only, from:

L. Ohlsson, P. Fay, and L.-E. Wernersson, "Picosecond Dynamics in a Millimetre-Wave RTD-MOSFET Wavelet Generator," *IET Electron. Lett.*, Apr. 2015, submitted.

Paper VIII

Paper VIII

Reproduced, with permission, from:

L. Ohlsson, D. Sjöberg, M. Ärlelid, M. Egard, E. Lind, and L.-E. Wernersson, "Admittance Matching of 60 GHz Rectangular Dielectric Resonator Antennas for Integrated Impulse Radio," in *2010 IEEE Conf. Loughborough Antennas and Propagation (LAPC)*, pp. 253–256, Nov. 8-9, 2010.

Admittance Matching of 60 GHz Rectangular Dielectric Resonator Antennas for Integrated Impulse Radio

Lars Ohlsson[*1], Daniel Sjöberg[*], Mats Ärlelid[*], Mikael Egard[†], Erik Lind[†], Lars-Erik Wernersson[*]

[*]Department of Electrical and Information Technology, Lund University
P.O. Box 118, 221 00 Lund, Sweden
[1]lars.ohlsson@eit.lth.se

[†]Department of Physics, Solid State Physics, Lund University
P.O. Box 118, 221 00 Lund, Sweden

Abstract—**Methods to achieve admittance matching of rectangular dielectric resonator antennas intended for 60 GHz impulse radio are reported. The motivation is to find a suitable antenna that may be integrated in the V-band gated tunnel diode wavelet generator, replacing its tank circuit and forming a low complexity transmitter. Probed one- and two-port scattering parameter measurements have been performed to characterise the fabricated antennas. Changing the feed structure from a tapered dipole to an offset fed and tapered slot, a change from capacitive to inductive characteristics is observed, and the matching to the gated tunnel diode is improved. Deembedded admittance resonance frequencies of fabricated antennas were found at 53.6 and 52.2 GHz for dipole and slot fed antennas, respectively. Characterising the transmission link between dipole fed antennas, a maximum antenna gain of 10.5 dBi and a 3 dB power bandwidth of 1.5 GHz were found at 53.3 GHz.**

I. INTRODUCTION

Wireless communication at 60 GHz is attractive for operation at high bit-rates and integrated impulse-based systems offer broadband low-power consumption transmitter solutions, requiring compact and energy efficient integrated antennas. Coplanar microstrip or waveguide antennas on electrically large semiconductor substrates are not feasible for impulse operation as they disperse the transmit signal into uncontrollable high order propagating modes [1]. High, V-band, operation frequency introduce the possibility to cut a dielectric resonator antenna (DRA) from the substrate and use an electrically small probe to feed it. DRAs have been studied for their effective radiation characteristics, small size and diversity of compatible feed methods. Placed on a mirror groundplane for increased directivity and compactness, a high performance and scalable antenna may be achieved.

We are targeting a rectangular DRA for our gated tunnel diode (GTD) wavelet generator, which is fabricated on 650 μm thick semi-insulating GaAs. Successful integration with an antenna that actively tunes the GTD to resonance at 60 GHz will produce an energy efficient wavelet transmitter operable in impulse mode by e.g. pulse position, frequency or binary phase shift keying [2], [3]. Constructing a transmitter using
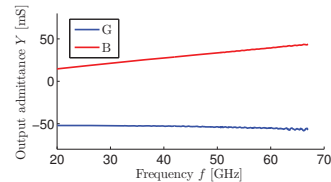

Fig. 1. Deembedded output admittance measured on a $10{\times}18$ μm^2 GTD, having an admittance $Y = -55 + 39\text{j}$ mS at 60 GHz.

a matched antenna, without any matching network or buffer, has advantages such as low power loss and minimal integration complexity.

In this work, different antenna feed structures on rectangular DRAs are fabricated and the admittance matching to the GTD evaluated. Also, transmission measurements between dipole fed DRAs demonstrate the functionality of the fabricated antennas.

II. GTD WAVELET TRANSMITTER

A resonant tunnel diode (RTD) may be utilised as the active component in an oscillator circuit since it possesses the physical property of negative differential conductance [2], [4]. The GTD is fabricated through incorporation a third terminal in the form of a permeable gate adjacent to the double barrier heterostructure of an AlGaAs/GaAs RTD. This has been made possible through the method of epitaxial GaAs overgrowth over ultra-thin tungsten wires [5]. Since the magnitude and sign of the GTD output conductance is related to the electrostatically controlled RTD area, it may be tuned using the gate bias [6]. Loading the GTD output with a tank circuit, it is possible to rapidly gate the circuit into and out of an oscillating state, producing down to 33 ps long 60 GHz wavelets directly from a baseband signal [3].

The admittance of, and hence matching of an antenna to, the GTD output is dependent on the defined active device area and
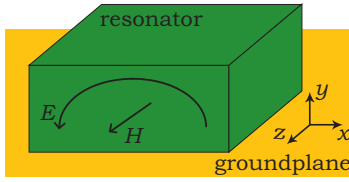
Fig. 2. Schematic of a rectangular dielectric resonator and the coordinate system used. Superimposed on the structure are electric E and magnetic H fields of the fundamental mode mirrored in a groundplane.

bias point. Deembedded output characteristics of a 10×18 μm^2 GTD measured at bias $V_{\text{CE}} = 0.94$ V and $V_{\text{GE}} = -0.50$ V is displayed in Figure 1, revealing a capacitive output admittance in the current implementation where $Y = -55 + 39\text{j}$ mS at 60 GHz. In the wavelet generator setup, the GTD is tuned to resonance by an inductive integrated coplanar short-circuit stub [2], [3]. Important in the selection of antenna is hence that it has an inductive and smooth susceptance which added to the GTD output yields a clean resonance condition at 60 GHz.

III. ANTENNA DESIGN

We treat the design of the DRAs as two separate problems. The dimensions of the resonator is assumed to be the main factor to determine the resonance frequency of the antenna, while the input admittance is tuned by the feed used to access the resonant mode, as will be discussed below.

A. Resonator

Rectangular dielectric resonators have non-confined TE-modes that efficiently radiate their energy to the surroundings. The principles of radiation from the fundamental mode in such a resonator have been reported together with design formula and experimental results [7], [8]. A schematic picture of a rectangular resonator geometry is presented in Figure 2, including a sketch of the electric and magnetic fields of the fundamental mode mirrored in the xz-groundplane.

The following design formulas of the dielectric waveguide model from [8] are used to obtain a preliminary design which is later refined using full wave simulations. In the x and y dimensions, the wavenumbers k_{x} and k_{y} of the fundamental resonant mode are simply fitted to the length l and height h of the mirrored resonator

$$k_{\text{x}} = \frac{\pi}{l} \tag{1a}$$

$$k_{\text{y}} = \frac{\pi}{2h}. \tag{1b}$$

A more intricate expression is used to relate the width w and wavenumber k_{z} of the resonator in the z direction

$$k_{\text{z}} \tan \frac{k_{\text{z}} w}{2} = \sqrt{(\epsilon_{\text{r}} - 1)k_0^2 - k_{\text{z}}^2}, \tag{2}$$

where $k_0 = 2\pi f_0/c$ is the wavenumber in free space. Applying the above expressions to the separation equation
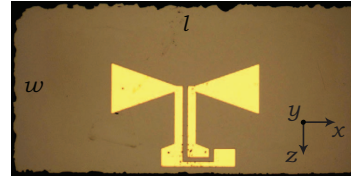

Fig. 3. Optical micrograph of a dipole feed with coplanar microstrip input on top of a 1300×650 μm^2 GaAs DRA.
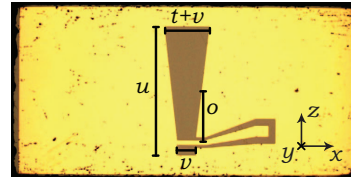

Fig. 4. Optical micrograph of a slot feed with coplanar waveguide input in a groundplane on a 1300×650 μm^2 GaAs DRA, also shown are definitions for slot dimensions.

$$k_{\text{x}}^2 + k_{\text{y}}^2 + k_{\text{z}}^2 = \epsilon_{\text{r}} k_0^2, \tag{3}$$

the width w of a resonator with known length l and electrical height $2h$ may be calculated for the desired resonance frequency f_0.

At 60 GHz, a mirrored $h = 650$ μm high and $l = 1300$ μm long GaAs resonator, $\epsilon_{\text{r}} = 12.9$, must then be $w = 450$ μm wide. Early experimental results on dipole fed DRAs indicated that a width $w = 650$ μm provides a better implementation at 60 GHz, although it according to theory would resonate at 56 GHz.

B. Feeds

Feeding of the rectangular resonator is done with an electrically small metallic structure positioned directly onto its side. Probes that mimic the fields of the targeted mode are desired in order to get a good electromagnetic coupling.

A dipole placed on top of and along the length of the resonator, to stimulate a parallel electric field, has been investigated previously through simulations [9]. This feeding solution turned out capacitive at the dielectric resonator resonance frequency as a dipole is an inherently capacitive structure below its resonance frequency. The antenna can be made inductive by shunting it with a small inductive strip, which corresponds to a simple matching network, which however will short circuit the radiation resistance. Here, we fabricated and studied dipole fed DRAs with tapered arms to increase their bandwidth, as shown on the optical micrograph in Figure 3.

A slot in an infinite groundplane is the complementary structure to a dipole, having qualitatively inverse impedances [10]. Feeding the resonator with a slot, oriented along the width of the resonator, should hence turn out as an inductive
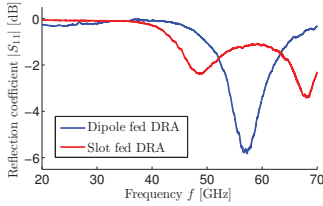
254

Paper VIII: © 2010 IEEE

Fig. 5. Deembedded reflection coefficient measurements on fabricated 1300×650 μm^2 GaAs DRAs with dipole feed and a $t = 100$ μm tapered and $\delta = 80\%$ offset fed slot.

antenna more suitable to match the capacitive GTD. This also allows for the groundplane to be deposited directly onto the resonator as a part of the feed structure, disturbing the targeted mode less than the dipole feed. Admittance modification may be performed by variation of the length u, width v and tapering t of the slot.

Feeding at an offset position in the slot has been simulated to suppress resonance undulations in the antenna susceptance [11]. In order to verify this result on slot fed DRAs, feed structures with up to $\delta = 2o/u = 90\%$ relative offsets were designed. An optical micrograph of a fabricated DRA with a $u = 500$ μm long, $v = 75$ μm wide, $t = 100$ μm tapered and $\delta = 80\%$ offset fed slot is shown in Figure 4.

IV. FABRICATION

Fabrication of the designed feed structures is performed using standard deep-UV lithography followed by thermal evaporation of metal and a lift-off process. Positive S1813 image resist on LOR 7B is used to define the antenna feed pattern consisting of a 8000 Å gold layer on an adhesion layer of 50 Å titanium [12]. This allows for the high conductivity feed to be tightly bonded to the resonator body, eliminating any parasitic effects that may be introduced from an air gap between feed and resonator [13].

Defining the rectangular GaAs resonator body from the substrate with Cl_2-based dry etching has been tested [9], but the process is challenging since it requires a very deep etching. The sample with predefined feed structures is instead sawed into 1300×650 μm^2 dies with a semiconductor saw.

V. CHARACTERISATION

Scattering parameter measurements were performed using a network analyser with calibrated 100 μm pitched GSG measurement probes. Antennas must hence be mounted on a carrier with their inputs facing up towards the alignment microscope.

Dipole fed DRAs are glued to a groundplane on a Si wafer using a cyanoacrylate-based adhesive, Loctite 420 with capillary function. Slot fed DRAs are instead glued onto a 2 mm thick PMMA plane, $\epsilon_r \approx 4$, through which they may radiate while being separated approximately 4 cm from the probe station chuck.
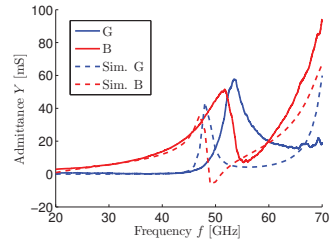

Fig. 6. Deembedded admittance measured on a dipole fed DRA, compared with an Efield simulation. Fundamental resonance is at $f_0 = 53.6$ GHz with admittance $Y(f_0) = 36.2 + 23.9j$ mS.
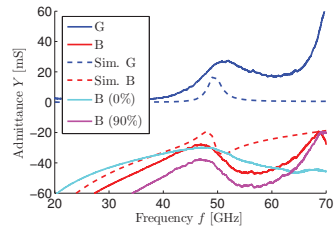

Fig. 7. Deembedded admittance measured on a slot fed DRA, compared with an Efield simulation. Fundamental resonance is at $f_0 = 52.2$ GHz with admittance $Y(f_0) = 22.1 - 43.2j$ mS. Susceptance of slot fed DRAs with the extreme point offsets, $\delta = 0$ and 90% are also shown.

Characterising the transmission between DRAs, a barrier of aluminum foil was inserted between adjacent antennas under test and a piece of Cu-plated printed circuit board was positioned above the antennas and used as a signal reflector. This setup blocks the direct path between the adjacent antennas and instead introduce a reflected link, allowing transmission measurements at broadside radiation over variable propagation distances $r = 83$ to 143 mm, corresponding to a few tens of free space wavelengths.

A. Reflection coefficient

Deembedded input reflection coefficient measurements on the dipole and slot fed DRAs in Figures 3 and 4 are presented in Figure 5, obtained with a 20 mS reference at a source power of -6 dBm. The dipole fed DRA have a relatively strong resonance peak, $|S_{11}| = -5.81$ dB at 57.3 GHz, while the slot fed DRA have two resonant peaks within the measurement interval, $|S_{11}| = -2.39$ dB at 48.6 GHz and $|S_{11}| = -3.41$ dB at 68.1 GHz, respectively.

B. Admittance

Admittance of the fabricated DRAs is extracted from the reflection coefficient measurements, showing the influence of dipole and slot feeding in Figures 6 and 7, respectively. Also shown are full wave simulation data from the method
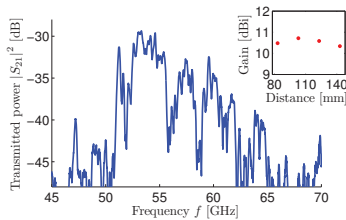
Fig. 8. Relative power level transmitted over $r = 143$ mm distance between dipole fed DRAs around the 53.3 GHz maxima. Inset show calculated maximum antenna gain, $G = 10.5$ dBi, at four equal increment distances.

of moments solver Efield (www.efieldsolutions.com), generally underestimating the bandwidth and conductance of the DRAs at resonance. The simulations predict the fundamental resonance frequency in the slot fed DRA reasonably well, while the resonance frequency in the dipole fed DRA is underestimated. The latter is likely a result of the metal connectors to the input waveguide on the fabricated dipole fed DRA, pushing the resonant mode away from the resonator top surface and reducing the electrical size of the resonator. The lower fundamental resonance frequency of the slot fed DRA may be explained by its smaller ground plane, allowing a more non-confined mode than with an infinite mirror. Measured input susceptance of antennas with both zero and maximum feed offsets are also shown in Figure 7, both undulating at their resonance frequencies.

C. Transmission

Positioning a signal reflector at different lengths from the mounted dipole fed DRAs, transfer characteristics as shown in Figure 8 were measured. The 3 dB power bandwidth of the link at 53.3 GHz is found to be 1.5 GHz, though this would be more than doubled if not for some sharp fadings. Antenna gain may now be calculated as half the difference between the theoretical free space pathloss (FSL) and the measured power maximum, which is shown on the Figure 8 inset for four equal increment distances. The shift in magnitude of link loss corresponds well to that of FSL, 45.4 to 50.1 dB at 83 to 143 mm transmit distance, and use of Friis transmission formula results in a constant maximum gain level $G = 10.5$ dBi at 53.3 GHz, confirming that the measured transfer of energy is achieved through far-field coupling between the antennas. This gain value is somewhat higher than the 5–7 dBi expected from a small dipole mirrored in a groundplane [14]. The foil barrier placed adjacent to the DRAs under test and coupling from the resonators to the probes may contribute to the increase in maximum gain.

VI. CONCLUSIONS

Dipole and slot fed rectangular DRAs have been fabricated and characterised, revealing that the two feed schemes result in qualitatively inverse input admittances. We observe susceptance resonance undulations for all fabricated slot fed

DRAs, independent on offset feeding of the electrically small feed slot. Dielectric waveguide design formulas were found to overestimate the resonance frequency of the fabricated DRAs. Inductive slot feeding of the DRA results in a resonance frequency close to simulations, while the capacitive dipole fed DRA resonate at higher frequencies, likely depending on the metal connectors to the input waveguide confining the mode further. A good susceptive match to the GTD may be performed with the tapered and offset fed slot DRA, although it need to be tuned to 60 GHz. Transmission experiments confirm the antenna functionality and show a maximum gain of 10.5 dBi for the dipole fed DRAs in the current measurement setup. Antenna gain can be further increased by combining several of the antennas considered in this paper as elements in an array antenna.

REFERENCES

[1] D. Pozar, "Considerations for millimeter wave printed antennas," *Antennas and Propagation, IEEE Transactions on*, vol. 31, no. 5, pp. 740–747, September 1983.

[2] M. Egard, M. Ärlelid, E. Lind, G. Astromskas, and L.-E. Wernersson, "20 GHz wavelet generator using a gated tunnel diode," *Microwave and Wireless Components Letters, IEEE*, vol. 19, no. 6, pp. 386–388, June 2009.

[3] M. Ärlelid, M. Egard, E. Lind, and L.-E. Wernersson, "Coherent V-band pulse generator for impulse radio BPSK," *Microwave and Wireless Components Letters, IEEE*, vol. 20, no. 7, pp. 414–416, July 2010.

[4] H. J. De Los Santos, K. K. Chui, D. H. Chow, and H. L. Dunlap, "An efficient HBT/RTD oscillator for wireless applications," *Microwave and Wireless Components Letters, IEEE*, vol. 11, no. 5, pp. 193–195, May 2001.

[5] L.-E. Wernersson, K. Georgsson, A. Litwin, L. Samuelson, and W. Seifert, "Planarization of epitaxial GaAs overgrowth over tungsten wires," *Journal of Applied Physics*, vol. 79, no. 1, pp. 500–503, January 1996.

[6] E. Lind, P. Lindstrom, and L.-E. Wernersson, "Resonant tunneling permeable base transistors with high transconductance," *Electron Device Letters, IEEE*, vol. 25, no. 10, pp. 678–680, October 2004.

[7] R. K. Mongia, "Theoretical and experimental resonant frequencies of rectangular dielectric resonators," *Microwaves, Antennas and Propagation, IEE Proceedings H*, vol. 139, no. 1, pp. 98–104, February 1992.

[8] R. K. Mongia and A. Ittipiboon, "Theoretical and experimental investigations on rectangular dielectric resonator antennas," *Antennas and Propagation, IEEE Transactions on*, vol. 45, no. 9, pp. 1348–1356, September 1997.

[9] D. Sjöberg, M. Egard, M. Ärlelid, G. P. Vescovi, and L.-E. Wernersson, "Design and manufacturing of a dielectric resonator antenna for impulse radio at 60 GHz," in *Antennas and Propagation, 2009. EuCAP 2009. 3rd European Conference on*, March 2009, pp. 3549–3553.

[10] L. V. Blake, *Antennas*, 1st ed. John Wiley & Sons, 1966.

[11] S. Suzuki, K. Hanashima, N. Kishimoto, and M. Asada, "Sub-THz resonant tunneling diode oscillators with offset-fed slot antenna," in *Indium Phosphide Related Materials, 2007. IPRM '07. IEEE 19th International Conference on*, May 2007, pp. 530–533.

[12] L. Ohlsson, "Impulse radio," Masters Thesis, Lund University, P.O. Box 118, 221 00 Lund, Sweden, March 2010.

[13] G. P. Junker, A. A. Kishk, A. W. Glisson, and D. Kajfez, "Effect of an air gap around the coaxial probe exciting a cylindrical dielectric resonator antenna," *Electronics Letters*, vol. 30, no. 3, pp. 177–178, March 1994.

[14] C. A. Balanis, *Antenna Theory: Analysis and Design*, 2nd ed. John Wiley & Sons, 1997.

Paper IX

Paper IX

Reproduced, with permission, from:

Slot-Coupled Millimeter-Wave Dielectric Resonator Antenna for High-Efficiency Monolithic Integration

Lars Ohlsson, Tomas Bryllert, Carl Gustafson, Daniel Sjöberg, Mikael Egard, Mats Ärlelid, and Lars-Erik Wernersson

Abstract—A readily mass-producible, flip-chip assembled, and slot-coupled III-V compound semiconductor dielectric resonator antenna operating in the millimeter-wave spectrum has been fabricated and characterized. The antenna has a 6.1% relative bandwidth, deduced from its 10 dB return loss over 58.8–62.5 GHz, located around the resonance at 60.5 GHz. Gating in the delay-domain alleviated the analysis of the complex response from the measured structure. The radiation efficiency is better than -0.1 dB in simulations fed from the on-chip coupling-structure, but reduced by 3.7 dB insertion loss through the measurement assembly feed. Antenna gain measurements show distortion in relation to the simulated pattern, which has a maximum gain of 6 dBi, mainly caused by interference from the electrically large connector used in the assembly. Mode degeneration in the utilized quadratic-footprint resonator was not seen to influence the performance of the antenna. The antenna is intended for on-chip integration and the fabrication technology allows scaling of the operation frequency over the complete millimeter-wave spectrum.

Index Terms—Antenna efficiency, dielectric resonator antennas (DRAs), millimeter-wave antennas, millimeter-wave communication.

I. INTRODUCTION

THERE is an increasing interest in exploring the millimeter-wave (mmW) spectrum, 30–300 GHz, for various wideband applications, including short-range radar [1] and Gbit/s wireless communication [2]. While maintaining a high efficiency in these systems, it is challenging to assemble antennas with monolithic microwave integrated circuit (MMIC) radio front-ends via wire-bonded interfaces or connectors. The solution is to flip-chip (FC) assemble a multichip module (MCM) and use on-chip integration of efficient antennas and

MMICs [3]. This results in reduced guiding and mismatch losses, but also allows high-precision fabrication techniques. Highly integrated antennas may be codesigned with active circuitry, allowing arbitrarily designed feed lines in between components, including direct integration.

Integrated mmW systems in silicon (Si) MMIC technology are attractive, due to its versatile complementary logic and low cost mass production. The resulting radiation efficiency η is however often below -10 dB because of the inherently lossy Si substrate [3]. Moreover, substrate modes affect the performance of resonant printed antennas on electrically large substrates [4]. This may result in erratic scaling behavior and additional loss. However, when such coupling is accounted for, or circumvented, the radiation efficiency in, e.g., Si-CMOS may be improved towards -2 dB [5], [6].

In a dielectric resonator antenna (DRA), coupling to the substrate modes is instead designed and their leaky radiation mechanism is exploited [7]. To transfer energy from a feed line and into a radiating resonator, e.g., a simple microstrip stub [8], coplanar waveguide (CPW) stub [9], or coaxial probe [10] in the vicinity of the dielectric body may be sufficient. For MMIC design, it is however convenient to use a more pronounced and planar coupling-structure whilst reducing the direct coupling between feed lines and resonator. The rectangular slot-coupled DRA geometry has been investigated for lower frequencies and may facilitate a CPW feed, well suited for MMIC fabrication [11]. Aperture coupling is one method often employed for mmW DRAs where the feed line and radiating resonator are separated geometrically [12], which for some applications may be convenient. It is possible to combine mmW front-ends and DRAs from different material technologies, e.g., alumina DRAs fed from FC bonded Si dies [13], but this is limited to off-antenna MMICs where inextricable feed losses are present. To approach full efficiency, III-V compound semiconductors, such as gallium arsenide (GaAs) and indium phosphide (InP), are alternative low-loss dielectrics on which MMIC front-ends may be fabricated directly integrated to mass-produced DRA coupling-structures. Active antenna elements with integrated high-speed, low-power III-V devices may, e.g., be utilized in a MCM as add-ons to Si-CMOS baseband circuitry in a wireless personal area network (WPAN) system.

Negative conductance wavelet generators, e.g., implemented utilizing resonant-tunneling diode (RTD) circuits fabricated from III-V compound semiconductor heterostructures [14], may be operated as front-ends for impulse radio communication in the 60 GHz band [15], [16]. At low-power, or high data-rate operation where efficiency and signal fidelity
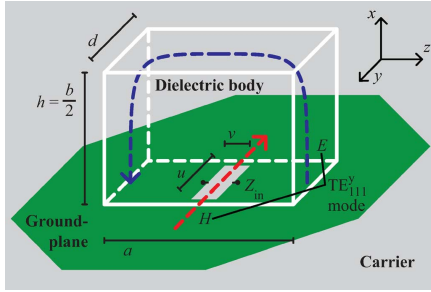
Fig. 1. Schematic geometry of a slot-coupled DRA with an octagonal ground-plane on a carrier substrate. The definitions of the dielectric body and basic coupling-slot parameters are indicated, along with an illustration of the fields of the excited fundamental TE_{111}^{y} mode.

is critical, codesign with an antenna is attractive [17]. This requires an antenna with wideband operation, well defined input characteristics, high efficiency, and readily scalable operation frequency. The possibility to fabricate such DRAs in a GaAs MMIC technology, and characterization using a probed measurement setup, was investigated previously [18], [19]. This paper addresses the design of a FC assembled 60 GHz slot-coupled DRA implemented in InP MMIC technology, and its characterization via a measurement assembly with a coaxial interface. This enables standard radiation pattern measurements, which is challenging in a probed setup.

II. ANTENNA DESIGN

The geometry of a slot-coupled rectangular DRA placed on a ground-plane reflector, and supported by a carrier substrate, is shown schematically in Fig. 1. It further includes an illustration of the dominant electric and magnetic fields, E and H, respectively, of the TE_{111}^{y} mode [20] resonating at the fundamental resonance frequency f_{r}. The electric field of this mode arcs along the longer side a of the dielectric body, while starting and ending normally oriented into the ground-plane reflector. The physical height h of the radiating resonator is electrically mirrored in the ground-plane to a virtual height $b = 2h$. The magnetic field of the TE_{111}^{y} mode is strong in the centre of the resonator and directed parallel to the shorter side d of the dielectric body. An electrically small slot in the ground-plane, oriented along the shorter radiating resonator side is used to couple energy into the DRA mode. The length u and width v of this coupling-structure, as indicated in Fig. 1, tunes the input impedance Z_{in} of the port defined over its centre. In the simulated model, the initial section of the CPW feed line, i.e., that which bridges the coupling-slot, is also regarded as part of the antenna, hence interfacing with a CPW port geometry. It is possible to recognize this port and coupling-structure as a CPW which transitions into two, oppositely directed, coplanar slot (CPS) transmission lines loaded by the radiating resonator. This allows the feed to galvanically contact the antenna, for biasing of any integrated components, in contrast to, e.g., capacitive slot-coupling from a microstrip transmission line.

A. Dielectric Body

The antennas were fabricated from a 650 μm thick semi-insulating InP substrate, which has a relative electric permittivity of $\epsilon_{\mathrm{r}} = 12.6$. This permittivity is within the typical range for III-V compound semiconductors and it limits the achievable relative bandwidth BW_{r} of the DRA, together with both the coupling-structure and any feed transitions. The bandwidth dependence on the permittivity of the dielectric body may be described via the radiation quality factor $Q_{\mathrm{rad}} \approx 1/BW_{\mathrm{r}}$, for narrow-band operation. This estimation neglects the discrepancy between their respective bandwidth definitions, i.e., from 10 dB return loss and half-power oscillation bandwidth, respectively. Regardless, a DRA radiation quality factor typically scale as $Q_{\mathrm{rad}} \propto \epsilon_{\mathrm{r}}^{\chi}$, where both the exponential factor χ and the proportionality depend on the chosen geometry of the radiating resonator [21]. Hence, even for a given dielectric body material, it is possible to increase the radiation bandwidth. Among those band-widening techniques, the most simple are to change the basic shape of the dielectric body and tune its geometrical aspect ratios. Further, several radiating resonant modes may be stacked into one single operation band, e.g., by inserting a low-permittivity inset between the radiating resonator and ground-plane [22], or by leaving the simple geometric shapes for more intricate DRA designs [23]. However, a simple geometry, such as rectangular, enables accurate scaling to small dimensions and high operation frequency f_{0}, which is an attractive property.

The scale of a rectangular DRA may in a first order approximation be estimated using a dielectric waveguide model (DWM) [20], where the radiating resonator notation for ease of interpretation is related to that of rectangular waveguides. In the DWM, the modes are assumed to be magnetically confined at the perimeter of the dielectric body. Its length a and virtual height b, corresponding to the transversal dimensions of the dielectric waveguide, hence set their corresponding mode wavenumbers. Along the width d of the dielectric body, interpreted as the dielectric waveguide extension in the propagation direction, a standing-wave assumption enforces a more complex expression which couples all radiating resonator dimensions with its permittivity [24]. The result from the DWM varies in accuracy, depending on the dielectric body aspect ratios and relative electric permittivity, but it may preferably be used to find a starting point for more thorough method-of-moments (MoM) or finite-element-method (FEM) calculations.

The basic rectangular radiating resonator geometry, without feed structure, was implemented in *COMSOL Multiphysics* and its height $h = 650$ μm was set to the InP substrate thickness. A quadratic-footprint resonator with a side length of $d = a = 1000$ μm was found to have an intrinsic fundamental resonance at $f_{\mathrm{r}} = 61.2$ GHz. This was suitable for operation at $f_{0} = 60$ GHz since the inclusion of a coupling-slot effectively will enlarge the dielectric body slightly. The quadratic-footprint resonator was chosen for two reasons. First, this geometry was found to increase the maximum radiation conductance seen from the antenna port, enabling a simple matching to a 50 $\Omega = 1/20$ mS interface. This was in relation to a more elongated design $d < a$, however, it was also found to increase the
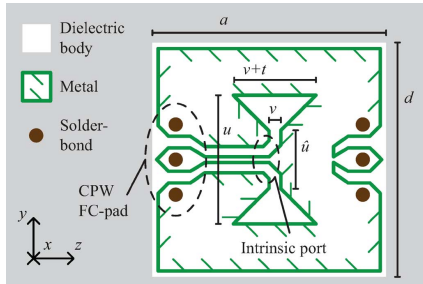
Fig. 2. Schematic layout of the metal pattern on the DRA, indicating the design parameters of the dielectric body and coupling-structure. The matched design is given by $a = d = 1000 \ \mu$m, $u = 500 \ \mu$m, $\hat{u} = 100 \ \mu$m, $t = 300 \ \mu$m, and $v = 10 \ \mu$m.

radiation quality factor Q_{rad} of the mode, which limited its intrinsic relative bandwidth to approximately 10%. Second, the quadratic-footprint geometry $d = a$ provided an interesting degeneration of the fundamental mode as an excitation in both polarizations, i.e., along either length or width, should be possible. It is feasible to investigate if this degeneration of the TE_{111}^{y} and TE_{111}^{z} modes has any impact on the antenna performance.

B. Coupling-Structure

The matching design of the coupling-slot was performed in *CST Microwave Studio*, using transient analysis and energy-based adaptive meshing for S-parameter convergence. The definitions of different DRA design parameters may be found from Fig. 2, showing a schematic drawing of the realized coupling-slot layout on the dielectric body, i.e., the bottom face of the DRA die. A 50 Ω CPW feed line, with 14 μm trace and 10 μm slots, guides the signal to the centre of the radiating resonator face, and the electrically small coupling-slot match it into the TE_{111}^{y} mode. The feed line is tapered over 100 μm from a FC-pad, with 50 μm trace and 50 μm slots, at the edge of the DRA die. A dummy FC-pad on the opposite edge provides symmetry and mechanical stability.

For a fixed resonator design, the conductance $\mathrm{Re}(1/Z_{\mathrm{in}})$ of the slot-coupled DRA port was found to be directly proportional to the slot length u. In contrast, it was found that the slot width v mainly tunes the susceptive behavior of the antenna port $\mathrm{Im}(1/Z_{\mathrm{in}})$, but also starts to load the radiating resonator heavily if it approaches a significant part of the dielectric body length a. This loading was seen as a large downward shift of the operation frequency f_0 from the intrinsic resonance frequency f_{r} of the unloaded radiating resonator. The coupling-slot width, in the centre of the DRA die face, was hence kept small to enable a virtually frequency-stable design procedure for the coupling-structure. Introduction of a slot tapering t, provided a means of shifting the input susceptance in a more controlled way than changing the full width of the slot. This layout ensured both a strong coupling to the TE_{111}^{y} mode and preserved its resonance frequency, while it allowed tuning of the susceptive behavior of the input. In order to accommodate space for

a feed, an untapered region of length $\hat{u}$ was introduced around the centered feed point.

A viable design and knowledge of its basic tuning principles were achieved at this stage. To optimize the matching, the slot length was increased until the radiation conductance exceeded 20 mS and then the ends of the slot were tapered to compensate for inductive characteristics. The coupling-slot was defined directly on the DRA substrate, instead of the carrier, which allowed an exact placement in relation to the resonator. An octagonal ground-plane extending outside the resonator, its shape chosen due to the low fields in the diagonal directions, was however provided from the carrier, 6.6 mm wide and with 2.6 mm long edges parallel to the DRA sides. An opening in the carrier metallization was left below the DRA, as it accommodates its own ground-plane. The final design on a 0.2 mm thick quartz carrier utilized a $t = 300 \ \mu$m tapered, $u = 500 \ \mu$m long and $v = 10 \ \mu$m wide coupling-slot, cf. Fig. 2. A $\hat{u} = 100 \ \mu$m long untapered region was left in the centre of the, CPS-type, coupling-slot. To smooth out the transition between the CPW feed line and the intrinsic port of the coupling-structure, cf. Fig. 2, the CPW signal trace corners were filled 11 μm while the ground edges were chamfered 5 μm. This provided improved tolerances in the fabrication process, due to reduced optical corner diffraction, as well as minor improvements in simulated performance.

In this design, it was verified by simulations that f_0 is controlled by the size of the dielectric body, and not significantly by the dimensions of the coupling-structure which sets the matching. It was not possible to split the matched input bandwidth of the quadratic-footprint DRA into two separate responses through scaling to slightly rectangular footprints. This implies that the coupling-slot only interacts with the TE_{111}^{y} mode without any parasitic effects from the TE_{111}^{z} mode, and further that aspect ratio scaling to, e.g., a wide DRA $d > a$ should be uncomplicated, despite the cross-polarized mode at lower frequencies. The resonance drift around $f_{\mathrm{r}} = 61.2$ GHz from footprint scaling with constant height, corresponding to fabrication variations, was estimated to $\Delta f_{\mathrm{r}}/\Delta a = -0.2$ GHz/5 μm, obtained from both DWM and FEM calculations when assuming $d = a$. For isotropic scaling, f_0 tunes reciprocally to the wavelength, reaching the upper edge of the mmW spectrum $f_{\mathrm{r}} = 300$ GHz for $h = 130 \ \mu$m height and a quadratic-footprint of $a = d = 200 \ \mu$m. However, the fabrication tolerances for this THz-DRA could be challenging to meet.

III. FABRICATION AND ASSEMBLY

Definition of the metal patterns, on the DRA and carrier substrates, was performed using thin-film processing technology, common in MMIC fabrication. After organic cleaning in acetone and isopropyl alcohol, the samples were coated with *MicroChem* lift-off resist and *Shipley* S1800-series image resist. This was followed by a soft-UV exposure, development of the lift-off pattern in MF319 and a rinse in deionized water. Oxygen plasma ashing removed any potential resist residues from the sample surface prior a thermally assisted evaporation deposition of 50 Å titanium (Ti), for adhesion-improvement, and then 8000 Å gold (Au) providing the main conducting layer. Lift-off performed in acetone and a rinse in isopropyl alcohol, followed
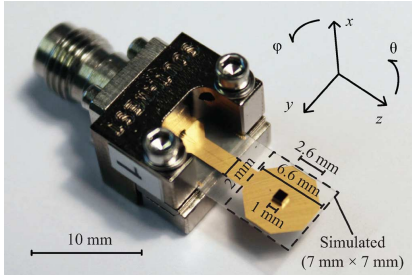
Fig. 3. Photograph of the fabricated antenna assembly, in a 2.40 mm end-launch connector. The spherical coordinate system, used for the radiation pattern representation in Fig. 9, is also illustrated.
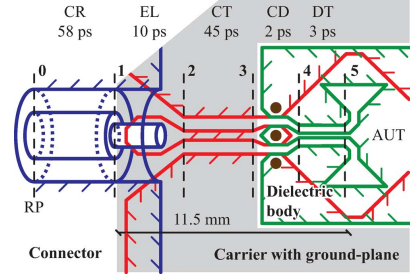

Fig. 4. Schematic outlines of the assembly feed details, connecting the coupling-slot on the DRA to the measurement reference plane. Its different transmission line segments are indicated together with their corresponding propagation delay, as estimated from material parameters. The interfaces in-between segments are numbered with bold-face numerals.

by removal of the lift-off-resist layer in MF319 and a rinse in deionized water, completed the definition of the metal patterns.

The InP substrate, metallized with coupling-structures, was diced into DRA dies and FC assembled onto 7 mm by 15 mm large quartz carrier substrates. A 3-point CPW interconnect was used for both the input and a dummy FC-pads of the DRA die and carrier. The utilized solder-bonding technique [25] produce interconnects with galvanic contact between the two chips, without thermocompression, which makes it suitable for bonding of brittle III-V compound semiconductor dies carrying active components. The assembled carrier to die stand-off gap is approximately 10 μm, and the FC interconnects are mechanically robust.

The carrier substrate utilizes a 50 Ω CPW transmission line, with 82 μm trace and 9 μm slots, which is of sufficiently small electrical dimensions to inhibit effective coupling to surface-waves [26]. This feed line connects the FC solder-bonded DRA die to an end-launch structure adopted for a *Southwest Microwave* 1492-03-A5 coaxial 2.40 mm connector. The extension of the ground-plane which harbours this feed line have a total width of 2 mm. The utilized 1492-03-A5 connector is mechanically compatible with the coaxial 1.85 mm interface and it has been engineered to function satisfactory up to 67 GHz. An assembled DRA mounted in such a connector is shown in Fig. 3, also introducing the definition of the coordinate system that is used in the presentation of the measured cuts of the radiation pattern.

IV. ANTENNA CHARACTERIZATION

The input port and pattern of the fabricated antennas were characterized using an *Agilent Technologies* E8361A vector network analyzer (VNA), identifying the voltage reflection coefficient Γ, loss L, and gain G from S-parameters. For input measurements, the reference plane (RP) was calibrated directly at the coaxial 1.85 mm port of the instrument. In order to measure cuts of the DRA assembly radiation pattern, a turntable and a linear positioner were interfaced by coaxial cables, for rotational and alignment abilities, and the calibration was in this case performed at the extended cable terminals.

The feed lines of the DRA assembly, including the connector, are too large to handle efficiently in the FEM solver. Instead,

only the 7 mm by 7 mm large part of the carrier substrate containing the reflector, cf. Fig. 3, was modelled initially. The CPW input of the DRA coupling-slot was directly open-circuit terminated and fed by a discrete port in the simulator. This is similar to the input impedance interface illustrated in Fig. 1, but applying the test signal between the CPW trace end and the ground metal edge at the termination, instead of directly over the coupling-slot. This intrinsic antenna port is where a compact MMIC preferably could be integrated on the antenna. In the case of the RTD generator discussed earlier, the coupling-slot could be modified to provide inductive port characteristics to resonate with the capacitance of the active device.

The distance to the connector body is large enough to be of minor importance for the tuning of the antenna input parameter, which has been verified through measurements. When the DRA is fed from the end of a 50 Ω transmission line, instead of the intrinsic port, the only discrepancy between measurement and simulation should ideally be the insertion loss of the feed line L_{feed}, and a phase rotation. However, the numerous cascaded transmission line sections of the assembly used for characterization do have an impact on the analysis of the measurement results. Also, even though the coupling-slot matching is not affected significantly, the radiation pattern of the realized DRA is influenced by having the bulky connector of the assembly in its vicinity.

In order to correlate the antenna measurements to the simulation, the effects of signal propagation over the feed line must be taken into account. An overview of the assembly feed, from the calibrated coaxial interface to the on-chip coupling-slot, is shown in Fig. 4, schematically indicating the different sections and their corresponding propagation delay. A signal impinging on the antenna assembly via the coaxial port will encounter; the connector transition block (CR), the end-launch (EL) from connector to carrier, the carrier transmission line (CT), the FC interconnect from carrier chip to DRA die (CD), the die transmission line (DT), and finally arrive at the antenna under test (AUT). For reference, the interfaces between the different feed line segments have been numbered, cf. Fig. 4, starting with **0** at the RP and ending with **5** at the AUT port. An index notation is used when referring to parameters of a specific interface, and
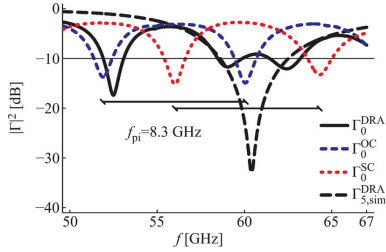
Fig. 5. Measured magnitudes of the voltage reflection coefficients, of the fabricated DRA assembly and the corresponding open- and short-circuit terminated assemblies, compared to the simulated intrinsic DRA port.

also when obtained by a specific method that is not direct measurement, e.g., $\Gamma_{5,\mathrm{sim.}}^{\mathrm{DRA}}$ is the simulated voltage reflection coefficient of the intrinsic, on-chip, port of the DRA.

A. Matching Analysis

The measured voltage reflection coefficient of the DRA assembly Γ_0^{DRA} is presented in Fig. 5, together with the simulated response of the intrinsic antenna port. The simulated antenna has a 10 dB return loss bandwidth over 58.6–62.5 GHz, limited by the coupling-structure, corresponding to a relative bandwidth of $BW_{\mathrm{r,sim.}} = 6.4\%$ around the resonance at $f_{0,\mathrm{sim.}} = 60.4$ GHz. The measured response is similar, but with two distinct differences. First, the operation bandwidth is broken by a low-level peak instead of the simulated sharp minimum and, secondly, the reflection coefficient show periodic interference instead of a simple magnitude shift due to increased insertion loss. These effects are inherent from a reflection at the EL section, as shown by the following analysis.

Two reference measurements are also shown in Fig. 5, Γ_0^{OC} and Γ_0^{SC}, for assemblies where the coupling-structure of the DRA have been exchanged with an open- and a short-circuit termination, respectively. The same periodicity of $f_{\mathrm{pi}} = 8.3$ GHz is present for both reference measurements, but shifted by about a half-period in relation to each other. This indicates that there are two strong reflections superpositioned on the feed line, with a propagation delay difference of $\tau_{\mathrm{pi}} = 1/f_{\mathrm{pi}} = 120$ ps. In relation to the various segment propagation delays on the feed, cf. Fig. 4, this may be explained by a parasitic reflection occurring at the transition from the CR to the EL, interacting with the desired signal from the AUT, interfaces **1** and **5** respectively. This parasitic reflection is likely governed by imperfect mode-matching between the cylindrical coaxial geometry and the planar CPW geometry.

By calculating the discrete inverse Fourier transformation ($\mathcal{F}^{-1}\{\cdot\}$) of the measured reflection coefficient, the corresponding delay-domain response $\gamma(\tau) = \mathcal{F}^{-1}\{\Gamma(f)\}$ is obtained. The normalized transient envelope magnitudes of the different measured assemblies are shown in Fig. 6 [27]. Expected timings of signals reflected at the different interfaces along the feed line are also indicated. The open- and short-circuit terminated assemblies show very similar magnitude transients but differ in phase. The conclusion drawn from the spectral periodicity of the reference structures are further

confirmed by the mismatch response at 102 ps, where the small timing discrepancy is a consequence of the actual placement of the RP. At the timing of interface **5**, cf. Fig. 4, both reference assemblies show strong responses, and the AUT assembly is seen slightly delayed thereafter because of its CPS extension beyond this point. The final visible mismatch response of the assemblies originate from the first high-order reflection between interfaces **5** and **1**.

In the delay-domain, it is possible to perform time-resolved filtering. This delay-domain gating procedure is sensitive to both the shape and position of the imposed window function $\Xi(\tau)$. The fed signal intensity was assumed to decay with an exponential behavior set by the radiation quality factor. Solving for the approximate time after which the reactive energy in the DRA has decayed by a factor of $\kappa = 100$ sets the gate width to $\Delta\tau_{\mathrm{g}} = \ln(\kappa)/(4\pi BW_{\mathrm{r}} f_0) = 94$ ps. Using a rectangular window function aligned to start at the timing of the peak of the targeted signal component, the transient signal corresponding to the main response from the AUT is captured. However, the measurement bandwidth, 3–67 GHz, limits the resolution of the transient signal and the gate must be widened accordingly, by $1/64$ GHz $=16$ ps, in both directions. The envelope of the window function for the DRA response is indicated by the shaded background in Fig. 6, while for the open- and short-circuited references the window function was shifted according to their corresponding peak timings. With these settings, the gate-stop conveniently coincides with the first high-order response of the implemented measurement assembly. Returning the signals to the spectral domain via discrete Fourier transformation ($\mathcal{F}\{\cdot\}$), the gated reflection coefficients $\Gamma_\Xi(f) = \mathcal{F}\{\Xi(\tau)\gamma(\tau)\}$ of the DRA and the short-circuit assemblies are shown in Fig. 7. The spectrally zero-padded, corresponding to temporal interpolation, transformations impose a truncation related bend at the edges of the measured spectrum which, however, cancels when the DRA assembly is compared to the short-circuit assembly $\Gamma_{5,\Xi/\mathrm{SC}}^{\mathrm{DRA}}$. This estimated response from the fabricated intrinsic antenna port is in close agreement to the simulation $\Gamma_{5,\mathrm{sim.}}^{\mathrm{DRA}}$, both in terms of $f_0 = 60.5$ GHz and $BW_{\mathrm{r}} = 6.1\%$ over 58.8–62.5 GHz.

Similar gated results are obtained as long as the interference from the CR-to-EL mismatch, at interface **1**, is excluded. This implies high quality for all other interfaces on the feed line. This strong similarity between gated-measured $\Gamma_{5,\Xi/\mathrm{SC}}^{\mathrm{DRA}}$ and simulated $\Gamma_{5,\mathrm{sim.}}^{\mathrm{DRA}}$ reflection coefficients further implies that undesired effects such as coupling between CPW and DRA, e.g., via excited TM surface-waves [26], is insignificant in this implementation.

B. Radiation Efficiency

The radiation efficiency of the designed DRA was evaluated through simulations, also in *CST Microwave Studio*. The efficiency results correspond to excitation of the intrinsic port at interface **5**, cf. Fig. 4, i.e., not accounting for the assembly feed line. The insertion loss of the assembly feed line was instead estimated from a phase-inverted mean between the open- and short-circuit terminated reference assemblies $L_{\mathrm{feed}} = 1/G_{\mathrm{feed}} \approx 1/|(\Gamma_0^{\mathrm{OC}} - \Gamma_0^{\mathrm{SC}})/2|$, according to transmission line theory. This estimate, shown as insertion gain G_{feed}
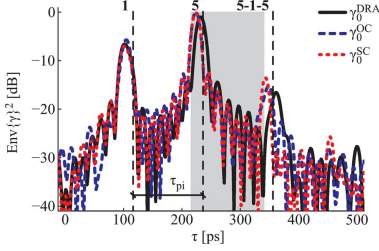
Fig. 6. Normalized magnitudes of the measured reflection coefficient delay-domain responses. The predicted positions of the reflection from different interfaces, cf. Fig. 4, are indicated. The envelope of the gating window function $\Xi(\tau)$ for the DRA assembly is indicated by the shaded background.
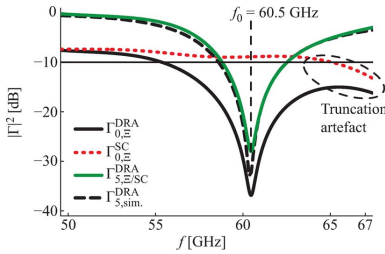

Fig. 7. Magnitudes of the spectral domain reflection coefficients resulting from the delay-domain gating procedure. Correcting the amplitude of the DRA assembly response, with regard to the short-circuit reference structure, reveal a close agreement to the simulated, on-chip, DRA port.
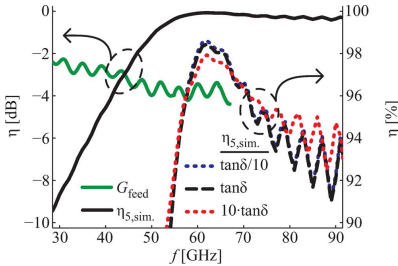

Fig. 8. Simulated radiation efficiency $\eta_{5,sim.}$ of the DRA for a $\tan \delta$ of different orders of magnitude. Notice that the simulated efficiency for the estimated value of tangential loss is plotted twice, scaled in both dB and %. Also shown is the insertion gain of the assembly feed line G_{feed}, estimated from measurements.

in Fig. 8, ideally accounts for all but higher-order reflections at the feed line termination. Its resulting spectral undulation is an artefact from such reflections. An approximate insertion loss of $L_{feed} = 3.7$ dB is deduced at $f_0 = 60.5$ GHz. Since the FC quality is high and the CR is large, this approximately corresponds to $L_{feed} = 0.33$ dB/mm over the 11.5 mm long CPW feed lines.

The radiation efficiency is limited by two loss mechanisms, metal loss and dielectric loss. The metal loss is inherent from

guiding of current along the resistive coupling-slot edges, while the dielectric loss is developed as both the fields of the excited TE_{111}^y mode and those of the coupling-slot interact with lattice dipoles and free charge carriers in the dielectric body. Any influence from the dielectric loss in the quartz carrier substrate was not seen in the simulations and is not investigated further since quartz is a high quality, i.e., low loss and homogenous, dielectric. This effect is also suppressed by the stand-off gap separating the die and its coupling-slot from the carrier.

The dielectric loss is characterized by the dielectric loss tangent $\tan \delta$ and is conventionally modelled as the sum of two main components

$$\tan \delta = \tan \delta_d + \frac{\sigma}{\omega \epsilon_0 \epsilon_r} \qquad (1)$$

where σ is the substrate conductivity, ω is the angular frequency of oscillation, and ϵ_0 is the electric permittivity of vacuum. The first term in (1), $\tan \delta_d$, is related to lattice dipole polarization in the radiating resonator material, and describes the theoretical lower bound of the loss in a dielectric. The lattice-related loss usually does not vary much for moderate changes in frequency, but may be elevated at specific points in the spectrum due to resonant responses of, e.g., material impurities. The second term in (1) describes the additional loss due to interaction with free charge carriers in the material, which decreases with increasing frequency. This indicates the importance of using an insulating DRA substrate in the fabrication process. The semi-insulating InP substrate has a high resistivity of $3 \cdot 10^7$ Ωcm, set from iron (Fe) doping. This corresponds well with the parameters of a similar substrate characterized to have a total dielectric loss tangent of $3 \cdot 10^{-4}$ at 11 GHz [28], which (1) reveals must be dominated by lattice loss. A first order conductivity model was used to extrapolate this value over the simulation bandwidth.

The simulated DRA efficiency $\eta_{5,sim.}$ is above 98%, or -0.1 dB at the operation frequency, and its spectral variation is shown in Fig. 8, scaled both in dB and % to better convey its dynamics, together with that from simulations using an order of magnitude variation of the loss. The radiation efficiency is seen to peak at approximately 62 GHz, close to the intrinsic resonance frequency of the dielectric body, and then decrease slowly with increasing frequency. Below the resonance frequency of the antenna, the radiation resistance diminish and losses increasingly dominate the accepted power. However, even at 10% below the DRA resonance frequency the radiation efficiency is more than 90%, or -0.5 dB. Simulating this trend, an order of magnitude less dielectric loss slightly improves the radiation efficiency, although marginally, coinciding with the efficiency found when only accounting for metal loss in the simulation. The corresponding increase of the dielectric loss reduces the peak radiation efficiency by half a percent. The metal loss must hence be between one and two orders of magnitude higher than the effect from the modelled dielectric loss tangent.

Regarding the metal loss, it is possible to show the reduced guiding attenuation for both increased metallization thickness and increased overall dimensions of the CPW geometry [29]. However, as both the CPW and CPS on the DRA must be of limited dimensions not to disturb the mode, the margins for reduced metal losses are limited. Scaling the operation frequency, skin
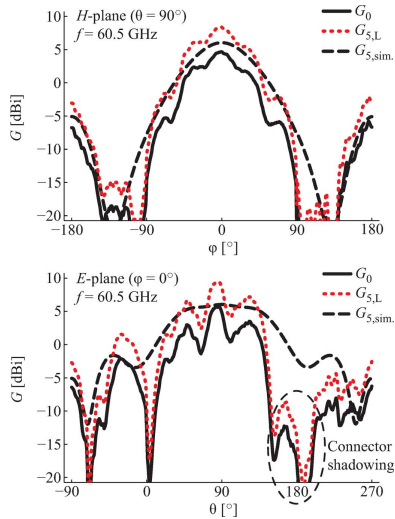
Fig. 9. Measured copolarized gain pattern cuts of the DRA assembly G_0, in the H- and E-planes, top and bottom, respectively. Also shown is the estimated intrinsic gain $G_{5,L}$, where the assembly insertion loss has been compensated, for comparison to the simulated intrinsic gain $G_{5,\text{sim.}}$. The spherical coordinate system is defined in Fig. 3.

effect confinement will increase the metal loss, while the dielectric loss according to most models is further reduced. Metal loss is hence the intrinsic limiting factor of the radiation efficiency in this antenna technology. It is however the feed line insertion loss that dominates in the fabricated design, due to metal loss. Hence, to maximize the efficiency in the integrated mmW system, the signal must be generated directly at the intrinsic antenna port. This justifies the use of InP DRAs with on-die MMICs for high performance applications.

C. Radiation Pattern

Radiation pattern measurements were performed with the VNA, transmitting from the DRA assembly and receiving using a *Flann Microwave* V-band horn antenna with a nominal gain value of 20 dBi. On the transmitting side, the AUT was attached to a turntable. By mounting the AUT in its two perpendicular orientations, both E- and H-plane patterns were recorded. The receiving horn was separated from the AUT by 0.895 m, limited due to cable length, and the high free-space pathloss together with the directive receiving antenna ensured to minimize the influence of multipath components. On the receiving side, the signal was amplified by a 50–67 GHz nominally 30 dB *HXI* low noise amplifier (LNA), and transferred from its waveguide port to the calibrated coaxial receiving port using an adapter.

The measured cuts of the DRA assembly gain pattern G_0 at $f_0 = 60.5$ GHz, shown in Fig. 9, were deduced from the measured transfer function by de-embedding the characteristics of

all the components used in the measurement setup. Specifically; the measured mismatch loss at interface **0**, the calculated theoretical free-space pathloss over the channel, the measured gain of the receiving antenna, the measured gain of the LNA, and the measured insertion loss of the WR-15 to 1.85 mm adapter. By also excluding the estimated assembly feed insertion loss, the intrinsic gain of the fabricated antenna $G_{5,L} = G_0 L_{\text{feed}}$ was estimated. This estimated intrinsic antenna gain, with respect to the on-chip intrinsic port at the coupling-slot, may be compared to the corresponding simulated intrinsic antenna gain $G_{5,\text{sim.}}$, also in Fig. 9. This gain data represents copolarized transmission and the antennas were found to be linear, as expected from [11], within the accuracy of the setup.

The maximum antenna gain, for both the measured and simulated cuts, was found close to the normal direction of the ground-plane on the DRA side of the assembly, i.e., around $\theta = 90°; \varphi = 0°$. In the simulated ideal case, where the connector and feed line are excluded, the maximum antenna gain was 6 dBi. The measured maxima in the H- and E-planes are $G_{5,L}(H; \varphi = 0°) = 8.4$ and $G_{5,L}(E; \theta = 86°) = 9.4$ dBi, respectively. This level discrepancy between the two measured radiation pattern cuts diminish in the ground-plane broadside direction as $G_{5,L}(E; \theta = 90°) = 8.6$ dBi. The sharp pattern variation makes the result susceptible to errors in absolute angular alignment, which may explain the remaining difference. However, minor sources of uncertainty are relative antenna positioning <0.1 dB, polarization alignment <0.1 dB, calibration drift due to twisting and bending of the coaxial cables, and LNA linearity.

With respect to the directivity/gain method with simulated directivity, which however has an uncertainty of approximately 20% [30], the fabricated antenna is likely very efficient in order to be able to nominally follow the simulated radiation pattern. If not, the assembly must by incidence have focused the radiated energy into the H- and E-planes. It is desirable to perform more accurate efficiency measurements, e.g., using the Wheeler method, but the machining of the required parts is challenging in the mmW spectrum. Delay-domain analysis of the radiation pattern responses reveals that there are no significant multipath propagation components. The qualitative differences between the shapes of the measured and simulated radiation pattern cuts are attributed to the presence of the assembly for the fabricated DRAs, and especially its bulky connector. However, the measurement bandwidth of 17 GHz does not provide the temporal resolution required to readily isolate the direct DRA response from either reflected or parasitic assembly responses in the delay-domain, but influences of such effects are discussed further below.

As the E-plane cuts through the connector around $\theta = 180°$ and since the simulated intrinsic DRA E-plane pattern has a relatively wide main lobe, there are many possibilities for strong interference in this plane. This would be seen as an added structure on the measured data, roughly undulating around the simulated level of the intrinsic DRA gain pattern. This is seen in the measured E-plane pattern cut where undulations vary the gain level within 6 dB in the main lobe, when normalized to the

shape of the simulated pattern. There is also a pronounced section where the connector blocks the line-of-sight radiation from the DRA, around $\theta = 180°$, indicated in Fig. 9. As expected for the more ideal fabricated H-plane, the interference with the connector gives less pronounced effects, with its typical gain level undulation reduced to about 3 dB. It was possible to reproduce the main features of the DRA assembly gain pattern in the simulation environment, with undulating interference and similar gain levels, by inclusion of a perfect electric conductor body shaped after the main features of the assembly. However, due to the significant increase in simulation time, dependence on the fine structure of the connector geometry, and the need for vast amounts of available memory for FEM simulation, an exact pattern reproduction was not pursued.

For reference, the radiation from an assembly where the coupling-slot was replaced by a short-circuit termination was also characterized. Its gain was found to be more than 10 dB below the corresponding gain of the DRA assembly in the main lobe. However, opposite the connector direction, i.e., around $\theta = 0°$ in the E-plane, the reference assembly was found to radiate with similar strength as the DRA assembly. The more pronounced overlay structure, and nominal level deviation, in this section of the measured E-plane radiation pattern, cf. Fig. 9, are likely related to this parasitic radiation phenomenon. The main source of this parasitic radiation is likely the EL, cf. Fig. 4, because of its complex geometry and electrical size. A quantitative evaluation of this measured data is however challenging, as the different terminations at interface **5** will influence the standing wave pattern on the assembly feed line, and hence the signal amplitude at any leaky position. For reference, the simulated radiation efficiency from comparable lengths of carrier CPW was found to be approximately -30 dB, which contradicts CPW radiation loss as a contributing factor to this radiation pattern artefact.

V. CONCLUSION

An efficient, slot-coupled, DRA fabricated utilizing MMIC technology and designed to allow integration with active components have been demonstrated. This antenna technology is demonstrated at 60.5 GHz with a relative bandwidth of 6.1%, but allows scaling of the operation frequency over the entire mmW spectrum. A simulated radiation efficiency of 98% is demonstrated, a value found to be intrinsically limited by metal loss. To preserve this efficiency in any system implementation, an integrated front-end on, or in close vicinity to, the DRA is required. It was also found from simulations that the coupling-slot exclusively couples to one of the two degenerated, cross-polarized, modes in a quadratic-footprint DRA. Delay-domain analysis revealed feed mismatch in the implemented coaxial/coplanar end-launch transition, and enabled response correction to identify the embedded antenna performance. A simulated radiation pattern with 6 dBi maximum antenna gain was demonstrated, while the measured pattern is similar, but affected by interference. This interference was concluded to originate both from scattering in the large connector body and parasitic radiation from its end-launch structure, which will not be parts of any actual system implementation. The combination of

rectangular DRAs with III-V semiconductor components in a compact monolithic design presents a promising high-performance platform for both integrated and active mmW on-chip antennas, or rather, chip-antennas.

REFERENCES

[1] M. Jahn, R. Feger, C. Wagner, Z. Tong, and A. Stelzer, "A four-channel 94-GHz SiGe-based digital beamforming FMCW radar," *IEEE Trans. Microw. Theory Techn.*, vol. 60, no. 3, pp. 861–869, Mar. 2012.

[2] I. Sarkas, S. T. Nicolson, A. Tomkins, E. Laskin, P. Chevalier, B. Sautreuil, and S. P. Voinigescu, "An 18-Gb/s, direct QPSK modulation SiGe BiCMOS transceiver for last mile links in the 70–80 GHz band," *IEEE J. Solid-State Circuits*, vol. 45, no. 10, pp. 1968–1980, Oct. 2010.

[3] T. S. Rappaport, J. N. Murdock, and F. Gutierrez, "State of the art in 60-GHz integrated circuits and systems for wireless communications," *Proc. IEEE*, vol. 99, no. 8, pp. 1390–1436, Aug. 2011.

[4] D. Pozar, "Considerations for millimeter wave printed antennas," *IEEE Trans. Antennas Propag.*, vol. 31, no. 5, pp. 740–747, Sep. 1983.

[5] A. Babakhani, X. Guan, A. Komijani, A. Natarajan, and A. Hajimiri, "A 77-GHz phased-array transceiver with on-chip antennas in silicon: Receiver and antennas," *IEEE J. Solid-State Circuits*, vol. 41, no. 12, pp. 2795–2806, Dec. 2006.

[6] R. A. Alhalabi and G. M. Rebeiz, "Design of high-efficiency millimeter-wave microstrip antennas for silicon RFIC applications," in *Proc. 2011 IEEE Int. Symp. Antennas Propag. (APSURSI)*, Jul. 2011, pp. 2055–2058.

[7] R. D. Richtmyer, "Dielectric resonators," *J. Appl. Phys.*, vol. 10, no. 6, pp. 391–398, Jun. 1939.

[8] R. A. Kranenburg and S. A. Long, "Microstrip transmission line excitation of dielectric resonator antennas," *Electron. Lett.*, vol. 24, no. 18, pp. 1156–1157, Sep. 1988.

[9] R. A. Kranenburg, S. A. Long, and J. T. Williams, "Coplanar waveguide excitation of dielectric resonator antennas," *IEEE Trans. Antennas Propag.*, vol. 39, no. 1, pp. 119–122, Jan. 1991.

[10] M. McAllister, S. Long, and G. Conway, "Rectangular dielectric resonator antenna," *Electron. Lett.*, vol. 19, no. 6, pp. 218–219, Mar. 1983.

[11] M. Al Salameh, Y. M. M. Antar, and G. Seguin, "Coplanar-waveguide-fed slot-coupled rectangular dielectric resonator antenna," *IEEE Trans. Antennas Propag.*, vol. 50, no. 10, pp. 1415–1419, Oct. 2002.

[12] J. T. H. St. Martin, Y. M. M. Antar, A. A. Kishk, A. Ittipiboon, and M. Cuhaci, "Dielectric resonator antenna using aperture coupling," *Electron. Lett.*, vol. 26, no. 24, pp. 2015–2016, Nov. 1990.

[13] J. Guzman, C. Calvez, R. Pilard, F. Gianesello, M. Ney, D. Gloria, and C. Person, "Silicon integrated dielectric resonator antenna solution for 60 GHz front-end modules," in *Proc. IEEE 12th Topical Meeting Silicon Monolithic Integr. Circuits RF Syst. (SiRF)*, Jan. 2012, pp. 53–56.

[14] M. Egard, M. Ärlelid, E. Lind, and L.-E. Wernersson, "Bias stabilization of negative differential conductance oscillators operated in pulsed mode," *IEEE Trans. Microw. Theory Techn.*, vol. 59, no. 3, pp. 672–677, Mar. 2011.

[15] M. Ärlelid, M. Egard, L. Ohlsson, E. Lind, and L.-E. Wernersson, "Impulse-based 4 Gbit/s radio link at 60 GHz," *Electron. Lett.*, vol. 47, no. 7, pp. 467–468, Mar. 2011.

[16] M. Egard, M. Ärlelid, L. Ohlsson, B. M. Borg, E. Lind, and L.-E. Wernersson, "In$_{0.53}$Ga$_{0.47}$As RTD-MOSFET millimeter-wave wavelet generator," *Electron Device Lett.*, vol. 33, no. 7, pp. 970–972, Jul. 2012.

[17] M. Shiraishi, H. Shibayama, K. Ishigaki, S. Suzuki, M. Asada, H. Sugiyama, and H. Yokoyama, "High output power ($\sim$400 μW) oscillators at around 550 GHz using large area RTD and optimized antenna structure," in *Proc. Compound Semiconductor Week (CSW/IPRM) 23rd Int. Conf. Indium Phosphide Related Mater.*, May 2011, pp. 1–4.

[18] D. Sjöberg, M. Egard, M. Ärlelid, G. P. Vescovi, and L.-E. Wernersson, "Design and manufacturing of a dielectric resonator antenna for impulse radio at 60 GHz," in *Proc. 3rd Eur. Conf. Antennas Propag. (EuCAP 2009)*, Mar. 2009, pp. 3549–3553.

[19] L. Ohlsson, D. Sjöberg, M. Ärlelid, M. Egard, E. Lind, and L.-E. Wernersson, "Admittance matching of 60 GHz rectangular dielectric resonator antennas for integrated impulse radio," in *Proc. Antennas Propag. Conf. (LAPC) Loughborough*, Nov. 2010, pp. 253–256.

[20] R. K. Mongia, "Theoretical and experimental resonant frequencies of rectangular dielectric resonators," in *IEE Proc. Microw., Antennas, Propag.*, Feb. 1992, vol. 139, no. 1, pp. 98–104.

[21] J. van Bladel, "On the resonances of a dielectric resonator of very high permittivity," *IEEE Trans. Microw. Theory Techn.*, vol. 23, no. 2, pp. 199–208, Feb. 1975.

[22] Y. Ge, K. P. Esselle, and T. S. Bird, "Compact dielectric resonator antennas with ultrawide 60%–100% bandwidth," *IEEE Trans. Antennas Propag.*, vol. 59, no. 9, pp. 3445–3448, Sep. 2011.

[23] K. S. Ryu and A. A. Kishk, "Ultrawideband dielectric resonator antenna with broadside patterns mounted on a vertical ground plane edge," *IEEE Trans. Antennas Propag.*, vol. 58, no. 4, pp. 1047–1053, Apr. 2010.

[24] R. K. Mongia and A. Ittipiboon, "Theoretical and experimental investigations on rectangular dielectric resonator antennas," *IEEE Trans. Antennas Propag.*, vol. 45, no. 9, pp. 1348–1356, Sep. 1997.

[25] T. Bryllert, A. Ø. Olsen, J. Vukusic, T. A. Emadi, M. Ingvarson, J. Stake, and D. Lippens, "11% efficiency 100 GHz InP-based heterostructure barrier varactor quintupler," *Electron. Lett.*, vol. 41, no. 3, pp. 131–132, Feb. 2005.

[26] M. Riaziat, R. Majidi-Ahy, and I.-J. Feng, "Propagation modes and dispersion characteristics of coplanar waveguides," *IEEE Trans. Microw. Theory Techn.*, vol. 38, no. 3, pp. 245–251, Mar. 1990.

[27] W. Wiesbeck, G. Adamiuk, and C. Sturm, "Basic properties and design principles of UWB antennas," *Proc. IEEE*, vol. 97, no. 2, pp. 372–385, Feb. 2009.

[28] J. Krupka, J. G. Hartnett, and M. Piersa, "Permittivity and microwave absorption of semi-insulating InP at microwave frequencies," *Appl. Phys. Lett.*, vol. 98, no. 11, pp. 112 112–112 112-3, Mar. 2011.

[29] G. Ghione, "A CAD-oriented analytical model for the losses of general asymmetric coplanar lines in hybrid and monolithic MICs," *IEEE Trans. Microw. Theory Techn.*, vol. 41, no. 9, pp. 1499–1510, Sep. 1993.

[30] D. M. Pozar and B. Kaufman, "Comparison of three methods for the measurement of printed antenna efficiency," *IEEE Trans. Antennas Propag.*, vol. 36, no. 1, pp. 136–139, Jan. 1988.

Lars Ohlsson received the M.Sc. degree in engineering nanoscience from Lund University, Lund, Sweden, in 2010, where he is currently performing postgraduate studies at the Department of Electrical and Information Technology.

He performs circuit design and develops technology for integrated antennas and millimeter-wave pulse generators. He further explores pulse-based communication and time-domain characterization. His research interests include integrated antennas, pulse generator circuits, device characterization, antenna codesign, and millimeter-wave pulse-based systems.

Tomas Bryllert was born in Växjö, Sweden, in 1974. He received the M.Sc. degree in physics and the Ph.D. degree in semiconductor physics from Lund University, Lund, Sweden, in 2000 and 2005, respectively.

From 1997 to 1998, he spent one year at The University of Waterloo, Waterloo, ON, Canada, as part of the Masters degree. During 2004, he worked as a Guest Researcher at the Microwave Electronics Laboratory, Chalmers, Sweden, developing frequency multipliers. Building on his research done at Lund University he developed key technology for the company Qunano AB during 2005. Starting in 2006, he joined the Physical Electronics Laboratory at Chalmers where the main research interest was device and circuit technology for THz frequency multipliers. From 2007 to 2009, he was with the Submillimeter Wave Advanced Technology (SWAT) group at California Institute of Technology/Jet Propulsion Laboratory, Pasadena, CA, USA, working on Terahertz imaging and radar systems. He is currently with the Terahertz and Millimeter Wave Laboratory at the Department of Microtechnology and Nanoscience (MC2), Chalmers, Göteborg, Sweden. He is also Cofounder and CEO of Wasa Millimeter Wave AB, which is a spin-off company from Chalmers developing and fabricating mm wave products.

Carl Gustafson received the M.Sc. degree in electrical engineering from Lund University, Lund, Sweden, where he is currently working toward the Ph.D. degree in the Department of Electrical and Information Technology.

His main research interests include channel measurements and modeling for 60 GHz wireless systems. Other research interests include antenna design, electromagnetic wave propagation, and UWB systems.

Daniel Sjöberg received the M.Sc. degree in engineering physics and the Ph.D. degree in engineering, electromagnetic theory, from Lund University, Lund, Sweden, in 1996 and 2001, respectively.

In 2001, he joined the Electromagnetic Theory Group, Department of Electrical and Information Technology, Lund University, where he was appointed Docent in electromagnetic theory in 2005, and is presently a Professor and the Director of Studies of the Department of Electrical and Information Technology. His research interests include electromagnetic properties of materials, composite materials, homogenization, periodic structures, numerical methods, radar cross section, wave propagation in complex and nonlinear media, and the inverse scattering problem.

Mikael Egard was born in Ystad, Sweden, in 1982. He received the M.Sc. degree in engineering physics, in 2007, and the Ph.D. degree in nanoelectronics, in 2012, both from Lund University, Lund, Sweden.

His current research interest includes design, fabrication, and evaluation of nanoelectronic ultrawideband impulse radio transceivers and their integration with compact antennas. Furthermore, his research activities also include fabrication, characterization, and modelling of planar and vertical field-effect transistors.

Mr. Egard received the Best Student Paper Award of the 2010 IEEE International Conference on Ultrawideband, Nanjing, China.

Mats Ärlelid received the M.Sc. degree in electrical engineering, in 2006, and the Ph.D. degree in circuit design, in 2012, both from Lund University, Lund, Sweden.

His research interest is to combine characterization and modeling of novel nanoelectronics with device and circuit simulation software for development of millimeter-wave frequency radio circuit designs. He has authored and coauthored over 20 scientific papers.

Dr. Ärlelid received the Best Student Paper Award at the 2010 IEEE International Conference on Ultrawideband.

Lars-Erik Wernersson received the M.Sc. degree in engineering physics and the Ph.D. degree in solid state physics at Lund University, Lund, Sweden, in 1993 and 1998, respectively.

Since 2005, he has been a Professor in Nanoelectronics at Lund University, following a position as Visiting Associate Professor at University of Notre Dame in 2002 and 2003. His main research interests include design and fabrication of nanowire- and tunneling-based nanoelectronic devices and circuits with applications in low-power electronics and wireless communication. He has authored/coauthored more than 120 scientific papers in this area.

Dr. Wernersson has been awarded two individual career grants from the Swedish Foundation for Strategic Research.

Paper X

Paper X

Reproduced, with permission, from:

Monolithically-Integrated Millimetre-Wave Wavelet Transmitter With On-Chip Antenna

Lars Ohlsson, Tomas Bryllert, Daniel Sjöberg, and Lars-Erik Wernersson

Abstract—An integrated millimeter-wave wavelet transmitter has been fabricated and characterized. It consists of a generator core on a co-designed compact monolithically-integrated antenna. The peak output equivalent isotropic radiated power has been measured to 11 dBm, in 80, 160, and 320 ps wavelets centred at 63.5 GHz. This corresponds to a power of 5 dBm radiated from the 6 dBi antenna. At a dc-supply of 1.45 V, the on-state power dissipation was estimated to 37 mW. The radiated wavelet-power over dc-dissipation conversion-efficiency is 9%.

Index Terms—Millimetre-wave integrated circuits, on-chip antennas, radio transmitters, wavelet generators.

I. INTRODUCTION

THE millimetre-wave (mmW) spectrum, 30–300 GHz, and in particular the V-band, 50–75 GHz, has attracted interest for various impulse-radio applications, e.g., communication [1] and radar [2]. Short-range systems for, e.g., handheld devices or data links, require compact and efficient transceiver modules. Compact transceiver modules may also be used as elements in beamforming arrays, where the scale of the elements limits the array density. Furthermore, it is important for transmitters to reach high output power to maximize signal range and channel capacity.

In this letter, we present a circuit implementation of a monolithically-integrated wavelet transmitter (WTx), based on antenna-coupled III-V semiconductor oscillators [3]. The WTx operates by direct-conversion from baseband control pulses to mmW wavelet radiation, utilising a transistor switch. We describe co-design of the active core from a previously investigated wavelet generator [4] and an inductively modified slot-coupled dielectric resonator antenna (DRA) [5], including their assembly and verification in a test module. This integrated WTx element is found advantageously compact while maintaining competitive signal-fidelity and conversion-efficiency, as compared to state-of-the-art transmitters.

II. DESIGN AND FABRICATION

An indium-gallium-arsenide (In-Ga-As) surface-channel metal-oxide-semiconductor field-effect-transistor (MOSFET)

L. Ohlsson, D. Sjöberg, and L.-E. Wernersson are with the Department of Electrical and Information Technology, Lund University, Lund, Sweden (e-mail: lars.ohlsson@eit.lth.se).

T. Bryllert is with the Department of Microtechnology and Nanoscience, Chalmers University of Technology, Göteborg, Sweden.
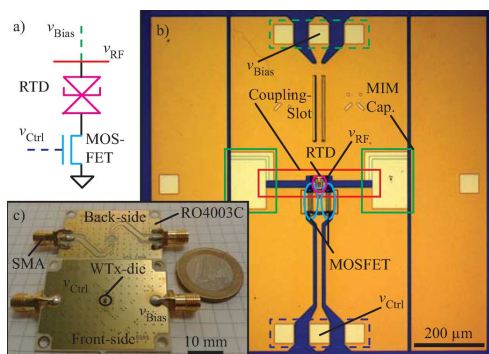
Fig. 1. WTx illustrations: (a) schematic of wavelet generator core, (b) chip-photo of die, and (c) photo of assembled module.

switch implemented in series with an aluminium arsenide (AlAs)/ In-Ga-As resonant-tunneling diode (RTD) constitutes the active core of the WTx, as illustrated in Fig. 1(a). The RTD provides negative conductance for power-generation and has a bias-dependent capacitance, approximately 4.5 fF/μm^2 [4]. This susceptance must be conjugate-matched by an inductance at the desired operation frequency. We propose that the RTD-MOSFET core should be monolithically-integrated with an inductive antenna element, forming a compact and efficient WTx. We target 62.5 GHz, i.e., the V-band centre, and utilize a slot-coupled indium phosphide (InP) DRA. This antenna technology allows fairly independent design of operation frequency and port matching [5].

A chip-photo of the fabricated monolithically-integrated WTx-die is shown in Fig. 1(b), where a 35 μm^2 RTD is centred on the 1×1 mm^2 footprint of the 0.65 mm semi-insulating InP chip. This III-V semiconductor die is utilized both as the physical platform for the RTD-MOSFET core, and as the radiating dielectric body of the DRA. An electrically-short inductive coupling slot, 300 μm long and 20 μm wide, directly matches the capacitive RTD [3]. This coupling-structure excites a mirrored TE$_{111}$ mode about the axis parallel to the slot. It provides an equivalent radiation conductance of a few mS at the antenna port [5], fed by the generated wavelet, v_{RF}. To allow the integration of the antenna with the RTD-MOSFET, a 330 pF metal-insulator-metal (MIM)-capacitor was placed at each end of the coupling-slot for ac-coupling of the dc-isolated sides of the circuit. These MIM-capacitors also serve as charge-reservoirs for bias-storage, stabilising the circuit for

pulsed operation [6]. Feeding a monolithically-integrated an-
tenna directly at its port with the RTD-MOSFET core, the need
to transfer mmW signals on dispersive and lossy transmission
lines was eliminated. This resulted in a compact and efficient
co-designed WTx-die.

The WTx-module, shown in Fig. 1(c), was finalized by flip-
chip solder-bonding a WTx-die on a 32 mil RO4003C circuit-
board carrier, using indium-based solder pellets placed with a
bonding wedge [7]. To transfer the control, v_{Ctrl}, and bias, v_{Bias},
signals to the WTx-die, SMA connectors at the edges cut by
the H-plane of the DRA, where the radiated power density is
low, were interfaced via finite-groundplane co-planar wave-
guides (CPWs). These transmission lines were fabricated mainly
on the back-side of the circuit board, as seen in Fig. 1(c), but they
were transferred through via-holes to small front-side CPWs,
which approach the WTx die in the E-plane of the DRA. This
circuit board connector layout and CPW alignment was chosen
to minimize the interference with the farfield pattern [5] and
surface-currents induced by the DRA, respectively. The design
would further allow control circuitry on the back-side and an
array of WTx-dies on the front-side.

III. MEASUREMENTS AND RESULTS

Wavelets were generated on the WTx-module, transmitted
over a 150 mm line-of-sight channel, and received using the
following setup. An Agilent N4906B serial bit error ratio tester
(BERT) was used to create a 2.8% duty-cycle baseband pattern
with an 80 ps time-base. This baseband pattern, with on- and off-
levels of $+0.5$ and -0.5 V, respectively, was fed to the control
input, v_{Ctrl}, of the WTx-module. The corresponding generated,
v_{RF}, radiated, v_{Tx}, and propagated wavelet signal was received
by a 16 dBi lens-augmented leaky-wave slot-antenna with al-
most negligible distortion [8]. Received waveforms, v_{Rx}, were
captured with an SE-100 sampling head of a LeCroy 100H os-
cilloscope. The 150 mm channel distance was chosen to ensure
good resolution on the oscilloscope. A Keithley 2602 source-
meter was used to supply a dc-bias of $v_{Bias} = 1.45$ V and
$i_{dc,2.8\%} = 5.2$ mA to the WTx-module. The pure on-state
dissipation is estimated to be $P_{dc} = v_{Bias}i_{dc,on} = 37$ mW,
where $i_{dc,on} = 25$ mA is the mean value of the RTD peak- and
valley-currents; continuous-wave measurement is not an option
due to the reactive bias-stabilization [6].

Signals received in the normal direction of the front- and
back-sides of the WTx module circuit-board, respectively, are
shown in Fig. 2, also including the front-side of a dummy
circuit-board. These coherent waveforms were captured when
80, 160, and 320 ps baseband pulses in a 20 ns period were
fed to the control input, and saved after 1001 averages. The
front-side WTx waveform shows three main wavelets, of in-
creasing lengths, shown in detail in Fig. 3 and will be discussed
below. Between the main wavelets, in Fig. 2, smaller wavelets
are clearly seen at a successive delay of 1 ns, corresponding to
antenna interference related to reflections between the antennas.
Additional minor fluctuations of the received waveform are
present, which we account to internal reflections in the lens-an-
tenna and pick-up of the control signal. Low-level emission
from the control signal connector end-launch and CPW was
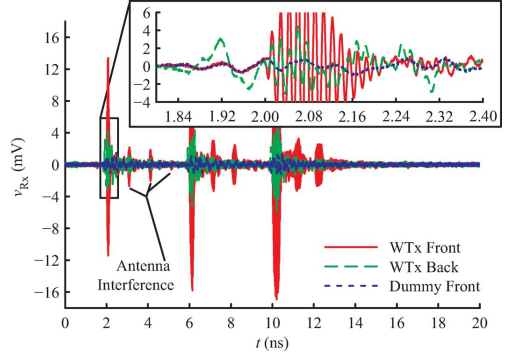verified from the measurement on the dummy circuit-board, as

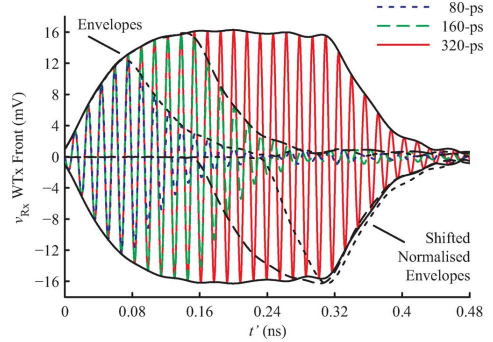Fig. 2.   Measured signals from the WTx, and a dummy circuit-board.

Fig. 3.   Filtered wavelets measured from the WTx, and their envelopes.

seen in the inset of Fig. 2. This control signal pick-up is pos-
sible due to the wide bandwidth of the Rx-antenna, but limited
within 3 mV peak-to-peak. The WTx back-side radiation, of
12 dB magnitude below the front-side level, originates from
the finite projected size of the DRA coupling-slot towards the
carrier circuit-board. If the low-frequency v_{Ctrl}-influences and
minor ringing are ignored, the back-side WTx wavelet is seen
to oscillate with an approximately rectangular envelope during
$t = 2$ to 2.08 ns. This indicates that a rectangular wavelet is
fed to the antenna, similar to that of a probed RTD-MOSFET
generator [4].

The received $f = 63.5$-GHz main wavelets are shown in
detail in Fig. 3, only including power in a 50 GHz brick-wall
bandwidth around the V-band centre to remove v_{Ctrl}-influences
and sampling noise. Also shown are their corresponding en-
velopes with positive polarity. In the negative y-axis direction,
envelopes of equalized height and shifted in time-base to coin-
cide in decay-timing are shown. The full-width half-maximum
(FWHM) lengths of the three wavelets are identified to be 94,
156, and 320 ps. A few oscillation periods are required be-
fore a steady-state amplitude is reached, due to the limited an-
tenna bandwidth, B, and the shortest wavelet does not reach

TABLE I
MMW WTx BENCHMARK COMPARISON

Reference	Technology	Oscillator Circuit	Antenna Gain and Type	Wavelet FWHM	Peak EIRP	On-State Dissipation	Footprint[a]
[9]	90-nm Si-CMOS	59.5-GHz LC-tank XC VCO	6-dBi Folded Dipole	300 ps[c]	11 dBm	183 mW at 1.2-1.5 V	10 mm²[b]
			14-dBi 4x3 Patch Array		19 dBm		130 mm²[b]
[10]	65-nm SOI CMOS	56-GHz Pulsed Colpitts ILO	-3-dBi Folded Diple	150 ps[b]	2 dBm	28 mW at 1.2 V	5 mm²[b]
This Work	AlAs/ In-Ga-As on InP	63.5-GHz RTD-MOSFET	6-dBi On-Chip DRA	156 ps	11 dBm	37 mW at 1.45 V	1 mm²

[a]Physical size of front-end and antenna. [b]Estimated from graphical data. [c]Estimated from data-rate.

steady-state at all. The maximum wavelet amplitudes are 25, 32, and 33 mV peak-to-peak, respectively, for the wavelets of increasing length. This corresponds to 8.9, 11, and 11 dBm equivalent isotropic radiated power (EIRP) from the WTx-module, found after de-embedding 52 dB free-space propagation loss, 16 dBi Rx-antenna gain, and 1 dB connector loss. The peak radiated power is hence $P_{Tx} = 5$ dBm, accounting for the 6 dBi directivity of the DRA found from simulations [5]. This translates into a radiated wavelet-power over dc-consumption conversion-efficiency of $\eta = P_{Tx}/P_{dc} = 8.9\%$.

The time-constants for start-up and decay, respectively, of the wavelet signal are found, from inspection of the envelopes in Fig. 3, to be independent of the wavelet length. In addition, by fitting of a first order response to the wavelet envelopes, the time-constants for both processes are found to be approximately $\tau = 50$ ps. As it is fed by an approximately square-envelope wavelet, this is dominated by the antenna time-constant. The equivalent bandwidth is $B = 1/(2\pi\tau) = 3.2$ GHz.

Key figures-of-merit of the WTx presented in this letter are summarized in Table I. It also reviews state-of-the-art integrated front-end solutions for mmW wavelet transmission [9], [10], along which, our implementation compares favourably. This is attributed to the use of efficient power-generation and coupling-techniques in III-V semiconductor technology instead of analog design in commercial silicon (Si)-technologies. If restricted to a sub-wavelength footprint, our WTx combines state-of-the-art wavelet length, peak EIRP, and power dissipation in an active antenna element.

IV. CONCLUSION

An 11 dBm EIRP 63.5 GHz WTx has been fabricated and characterized. It consists of an RTD-MOSFET core loaded by a co-designed inductive DRA, with a chip footprint of only 1 mm². The active core and antenna are monolithically-integrated on-chip, achieving a conversion-efficiency of 8.9%. Use of feed lines and matching networks to couple power from a generator to the radio channel is avoided. Compact systems and dense array implementations may be explored using this WTx technology in the mmW spectrum.

REFERENCES

[1] M. Ärlelid, M. Egard, L. Ohlsson, E. Lind, and L.-E. Wernersson, "Impulse-based 4 Gbit/s radio link at 60 GHz," *Electron. Lett.*, vol. 47, no. 7, pp. 467–468, Mar. 2011.
[2] M. Bocquet, N. Obeid, C. Loyez, C. Lethien, F. Boukour, N. Rolland, and M. Heddebaut, "Comparison between 60-GHz UWB frequency modulation and UWB impulse-radio location systems," in *Proc. Eur. Radar Conf. (EuRAD)*, Oct. 30–31, 2008, pp. 41–43.
[3] H. Kanaya, H. Shibayama, S. Suzuki, and M. Asada, "Fundamental oscillation up to 1.31 THz in thin-well resonant tunneling diodes," in *Proc. Int. Conf. Indium Phosphide Related Mater. (IPRM)*, Aug. 27–30, 2012, pp. 106–109.
[4] M. Egard, M. Ärlelid, L. Ohlsson, B. M. Borg, E. Lind, and L.-E. Wernersson, "In0.53Ga0.47As RTD-MOSFET millimeter-wave wavelet generator," *IEEE Electron Device Lett.*, vol. 33, no. 7, pp. 970–972, Jul. 2012.
[5] L. Ohlsson, T. Bryllert, C. Gustafson, D. Sjöberg, M. Egard, M. Ärlelid, and L.-E. Wernersson, "Slot-coupled millimeter-wave dielectric resonator antenna for high-efficiency monolithic integration," *IEEE Trans. Antennas Propag.*, vol. 61, no. 4, pp. 1599–1607, Apr. 2013.
[6] M. Egard, M. Ärlelid, E. Lind, and L.-E. Wernersson, "Bias stabilization of negative differential conductance oscillators operated in pulsed mode," *IEEE Trans. Microw. Theory Techn.*, vol. 59, no. 3, pp. 672–677, Mar. 2011.
[7] T. Bryllert, A. O. Olsen, J. Vukusic, T. A. Emadi, M. Ingvarson, J. Stake, and D. Lippens, "11% efficiency 100 GHz InP-based heterostructure barrier varactor quintupler," *Electronics Lett.*, vol. 41, no. 3, pp. 131–132, Feb. 2005.
[8] I. Vakili, L. Ohlsson, M. Gustafsson, and L.-E. Wernersson, "Wideband and non-dispersive wavelet transmission using leaky lens antenna," *Electron. Lett.*, vol. 49, no. 5, pp. 321–322, Feb. 2013.
[9] J. Lee, Y. Chen, and Y. Huang, "A low-power low-cost fully-integrated 60-GHz transceiver system with OOK modulation and on-board antenna assembly," *IEEE J. Solid-State Circuits*, vol. 45, no. 2, pp. 264–275, Feb. 2010.
[10] A. Siligaris, N. Deparis, R. Pilard, D. Gloria, C. Loyez, N. Rolland, L. Dussopt, J. Lanteri, R. Beck, and P. Vincent, "A 60 GHz UWB impulse radio transmitter with integrated antenna in CMOS65 nm SOI technology," in *Proc. IEEE 11th Topical Meeting Silicon Monolith. Integr. Circuits RF Syst. (SiRF)*, Jan. 17–19, 2011, pp. 153–156.